UNIVERSITY OF ROCHESTER
LABORATORY FOR LASER ENERGETICS

Volume 146
January–March 2016
DOE/NA/1944-1264

LLE Review

Quarterly Report

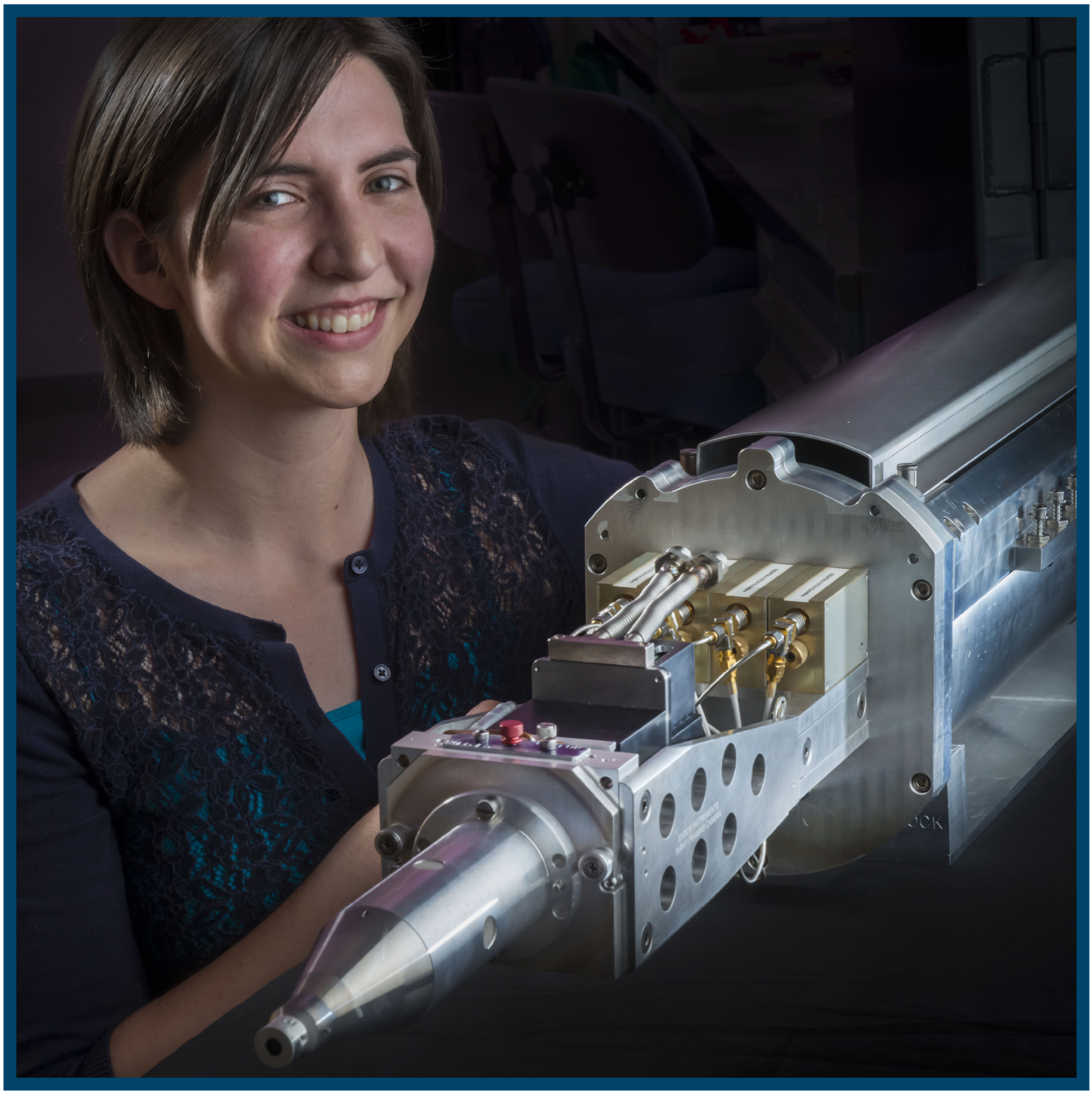

About the Cover:

The cover photo shows Physics and Astronomy graduate student Amanda Davis with an x-ray framing camera used to measure x-ray self-emission. She reports on experiments that angularly resolve the mass ablation rates and ablation-front trajectories in order to isolate and quantify cross-beam energy transfer (CBET) in direct-drive implosions on OMEGA and at the National Ignition Facility. Sixteen 2-D images of the coronal x rays were taken throughout the implosion using four-strip x-ray framing cameras as shown below.

X-ray self-emission images of Si-coated CH target implosions were used to determine the mass ablation rate of Si and the ablation-front trajectories of the target. Adding a thin layer of Si over a CH shell generates two peaks in x-ray self-emission images, indicating the position of the ablation front and the interface of the two layers in the plasma. The emergence of the second peak is used to measure the burnthrough time of the outer layer, giving the average mass ablation rate of the remaining Si layer and instantaneous mass.

This technique was adapted to measure the angular mass ablation rate in polar-drive experiments where CBET predominately affects the drive on the equator. The effects of CBET were isolated by simultaneously measuring the distances between the radii of the outer Si layer and the inner ablation front at the pole and the equator. These results are being used to validate the 2-D CBET and nonlocal thermal-transport models at direct-drive–ignition plasma conditions.

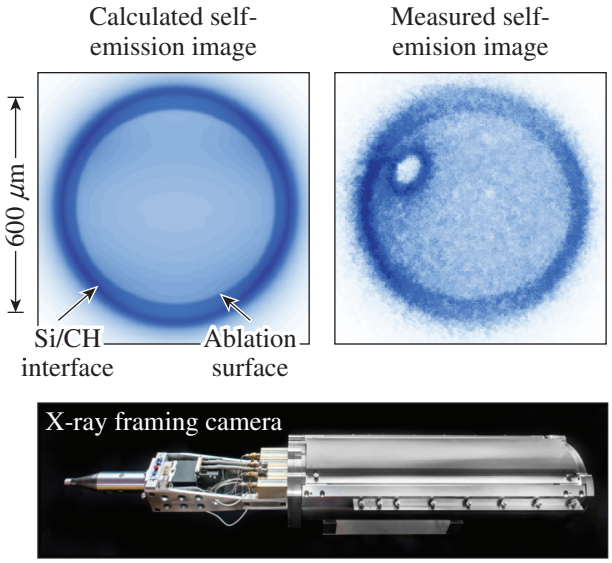

E25336JR

This report was prepared as an account of work conducted by the Laboratory for Laser Energetics and sponsored by New York State Energy Research and Development Authority, the University of Rochester, the U.S. Department of Energy, and other agencies. Neither the above-named sponsors nor any of their employees makes any warranty, expressed or implied, or assumes any legal liability or responsibility for the accuracy, completeness, or usefulness of any information, apparatus, product, or process disclosed, or represents that its use would not infringe privately owned rights. Reference herein to any specific commercial product, process, or service by trade name, mark, manufacturer, or otherwise, does not necessarily constitute or imply its endorsement, recommendation, or favoring by the United States Government or any agency thereof or any other sponsor. Results reported in the LLE Review should not be taken as necessarily final results as they represent active research. The views and opinions of authors expressed herein do not necessarily state or reflect those of any of the above sponsoring entities.

The work described in this volume includes current research at the Laboratory for Laser Energetics, which is supported by New York State Energy Research and Development Authority, the University of Rochester, the U.S. Department of Energy Office of Inertial Confinement Fusion under Cooperative Agreement No. DE-NA00001944, and other agencies.

Printed in the United States of America
Available from
National Technical Information Services
U.S. Department of Commerce
5285 Port Royal Road
Springfield, VA 22161
www.ntis.gov

For questions or comments, contact James B. Oliver, Editor, Laboratory for Laser Energetics, 250 East River Road, Rochester, NY 14623-1299, (585) 275-1194.

www.lle.rochester.edu

UNIVERSITY OF ROCHESTER
LABORATORY FOR LASER ENERGETICS

Volume 146
January–March 2016
DOE/NA/1944-1264

LLE Review

Quarterly Report

UR LLE

Contents

In Brief iii

Isolating and Quantifying Cross-Beam Energy Transfer in Direct-Drive Implosions on OMEGA and the National Ignition Facility 57

Time-Multiplexed Pulse Shaping 68

Continuous Distributed Phase-Plate Advances for High-Energy Laser Systems 74

Nanomechanics and Laser-Induced Damage in Optical Multilayer Dielectric Gratings 78

Permeation Fill-Tube Design for Inertial Confinement Fusion Target Capsules 90

Acidic Magnetorheological Finishing of Infrared Polycrystalline Materials 98

Publications and Conference Presentations

In Brief

This volume of the LLE Review, covering January–March 2016, features "Isolating and Quantifying Cross-Beam Energy Transfer in Direct-Drive Implosions on OMEGA and at the National Ignition Facility," by A. K. Davis, D. Cao, D. T. Michel, M. Hohenberger, D. H. Edgell, R. Epstein, V. N. Goncharov, S. X. Hu, I. V. Igumenshchev, J. A. Marozas, A. V. Maximov, J. F. Myatt, P. B. Radha, S. P. Regan, T. C. Sangster, and D. H. Froula. This article (p. 57) reports on the Laboratory for Laser Energetics' polar-direct-drive experiments at the National Ignition Facility to quantify cross-beam energy transfer (CBET). The polar-direct-drive laser configuration was used to limit CBET at the target poles while maintaining its influence at the equator. This combination of low- and high-CBET conditions in a single implosion made it possible to determine the effects of CBET on the ablation rate and ablation pressure. Hydrodynamic simulations performed without CBET agree with the measured ablation rate and ablation-front trajectory at the target pole, confirming that the CBET effects at the pole are small. CBET simulations incorporating a gain multiplier lead to excellent agreement with both polar and equatorial measurements.

Additional research highlights presented in this issue include:

- C. Dorrer, W. A. Bittle, R. Cuffney, M. Spilatro, E. M. Hill, T. Z. Kosc, J. H. Kelly, and J. D. Zuegel demonstrate an eight-channel, time-multiplexed pulse-shaping system that generates, demultiplexes, and retimes optical waveforms from a single pulse-shaping unit (p. 68). This system can provide pulses to multiple optical systems with low relative jitter and lower cost. Losses of less than 5 dB and extinction ratios of the order of 50 dB for an eight-channel system are measured for the system. Operating with only four channels provides a contrast of the order of 70 dB by using the final stage of the demultiplexer to enhance the contrast in the output.

- J. A. Marozas, T. J. B. Collins, J. D. Zuegel, P. W. McKenty, D. Cao, S. Fochs, and P. B. Radha describe a design approach to continuous distributed phase plates (DPP's) using the code *Zhizhoo'* (p. 74). *Zhizhoo'* produces DPP designs with exceptional control of the envelope shape, spectral and gradient control, and robustness from near-field phase aberrations. The code allows for rapid DPP design optimization, with achieved focal-spot shapes having high fidelity relative to the design objective. Using a personal computer, phase-dislocation–free DPP designs with low near-field modulation can be achieved with a <1% to 2% weighted σ_{rms} error of the far-field spot shape in a few minutes.

- K. Mehrotra, B. N. Taylor, A. A. Kozlov, S. Papernov, and J. C. Lambropoulos report on experimental efforts to correlate the mechanical properties of multilayer diffraction gratings to laser-induced–damage thresholds (LIDT's) (p. 78). Nanoindentation of holographic diffraction gratings etched into silica provides the penetration depth, brittleness, and yield strength of the structure; lower LIDT's are strongly correlated with greater measured yield stresses and lower penetration depths for the samples evaluated. This work indicates mechanical testing may provide guidance on grating cleanliness and damage thresholds for use in high-intensity laser systems.

- B. S. Rice, J. Ulreich, C. Fella, D. Turner, and M. J. Bonino (LLE); J. Crippen and P. Fitzsimmons (General Atomics); and A. Nikroo (LLNL, formerly at General Atomics) report on a unique approach for permeation filling of nonpermeable inertial confinement fusion target capsules with deuterium–tritium (DT) (p. 90). This process uses a permeable capsule coupled into the final target capsule with a tapered 0.1- or 0.08-mm-diam fill tube. Such an approach enables filling of new target materials without requiring the design and construction of a fill-tube–based DT filling station. Permeation filling of glow-discharge polymerization (GDP) targets using this method have been successfully demonstrated, as well as ice layering of the target, yielding an inner ice surface roughness of <1-μm rms (root mean square).

- S. Salzman, H. J. Romanofsky, G. West, K. L. Marshall, S. D. Jacobs, and J. C. Lambropoulos report on polishing infrared polycrystalline materials using magnetorheological finishing (p. 98). Acidic, low-viscosity magnetorheological fluids containing alumina or nanodiamond are used to polish infrared materials, including chemical-vapor–deposited (CVD) ZnS with a reduced surface structure, in an effort to improve surface microroughness. Surface roughness and power-spectral density results show that the emergence of "pebbles" on the surface of several CVD ZnS substrates finished with the acidic MR fluid containing a nanodiamond abrasive is significantly minimized, and the surface microroughness achieved was as low as ~30-nm peak-to-valley and ~6-nm rms.

James B. Oliver
Editor

Isolating and Quantifying Cross-Beam Energy Transfer in Direct-Drive Implosions on OMEGA and the National Ignition Facility

Introduction

In direct-drive inertial confinement fusion (ICF) experiments, laser beams directly illuminate a spherical capsule to drive an implosion. The capsule compression transfers the kinetic energy of the converging shell into the internal energy of the fuel, triggering fusion reactions in the hot dense core.[1] The laser energy that drives the implosion is absorbed in the plasma corona and conducted to the ablation front of the target by electron thermal transport, resulting into ablation of the shell and its corresponding acceleration caused by the rocket effect.[2]

Laser beams crossing in the coronal plasma can drive the stimulated Brillouin scattering (SBS) instability, which can redirect a significant fraction of the incident energy out of the plasma.[3] Cross-beam energy transfer (CBET) is seeded SBS facilitated by ion-acoustic waves driven by the beating of two electromagnetic waves in a plasma.[4] Depending on the amplitude of the driven ion-acoustic wave, energy is transferred from one electromagnetic (pump) wave to another (seed) wave. In direct-drive fusion experiments, outgoing rays that have refracted around the target beat with incoming rays from other beams to transfer significant energy out of the plasma before it can be absorbed. In simulations of direct-drive implosions, where individual beam intensities remain low ($I < 10^{14}$ W/cm^2), the amplitudes of the ion-acoustic waves are small. Nevertheless, significant energy transfer results from the net effect of many beam crossings throughout the coronal plasma.[5–7]

The existence of CBET was first demonstrated by experiments using planar targets.[8,9] In indirect-drive ICF experiments, this mechanism was used to transfer kilojoules of laser energy from the polar to the equatorial drive of an imploding target to improve capsule symmetry,[10–12] but uncertain plasma conditions and the large amplitude of the ion-acoustic waves driven by high single-beam intensities ($I \sim 10^{15}$ W/cm^2) have challenged the ability to obtain an accurate predictive model.[11–13] These experiments additionally identified the ability of CBET to rotate the polarization of the beams, suggesting that polarization rotation should be included when modeling systems with multiple CBET regions.[14,15] Direct-drive experiments used scattered-light spectra and shell-trajectory measurements to demonstrate the existence of CBET[5] and estimate its level.[6,16,17]

This article presents measurements of CBET's effect on coupling laser energy to the ablation front of a target by comparing its effect on the mass ablation rate and ablation-front trajectory in low- and high-CBET regions in the same implosion. A polar-direct-drive configuration[18] was used, in which a ring of beams encircling the equator was dropped and the remaining beams were repointed toward the equator, reducing detrimental CBET at the poles while enhancing it at the equator.[19,20] This combination of low- and high-CBET conditions in the same target implosion made it possible to determine the effects of CBET on hydrodynamic coupling (Fig. 146.1). The simultaneous measurements of the angularly resolved mass ablation rates and shell trajectories determine the kinetic energy of the implosion by providing the instantaneous mass of the target and the ablation-front velocity.

Two-dimensional *DRACO*[21] hydrodynamic simulations performed with an implicit Schurtz–Nicolai–Busquet (iSNB)

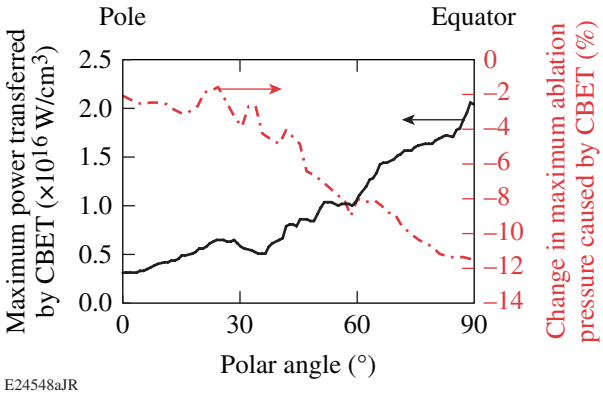

Figure 146.1
The polar-direct-drive laser configuration results in greater power transferred by cross-beam energy transfer (CBET) at the target equator compared to the pole (black curve). The consequent difference in ablation pressure (red dashed–dotted curve) was calculated from 2-D *DRACO* simulations with and without the CBET model for the highest-intensity polar-direct-drive OMEGA experiments (t = 0.8 ns).

thermal-transport model,[22] but without a CBET model, reproduced the measured trajectories at the pole of the target, verifying that the coupling physics is well modeled when CBET effects are negligible. These simulations, however, overpredicted the velocity of the shell and ablation rate at the equator. By including a 3-D ray-based CBET model adapted from 1-D plane-wave equations developed by Randall[4] in the hydrodynamic simulations, the simulated equatorial trajectories agreed better with measurements, while having a minimal impact on the polar trajectory. However, the simulations still overpredicted the drive at the equator.

The geometric ray-propagation model used in *DRACO* transports energy while neglecting diffraction effects that produce small-scale structures (temporal and spatial). The CBET model requires knowledge of the cumulative background pump intensity distributed over the propagation angle and wavelength, which is computed by accumulating the ray-energy path-length product and weighting the sum by the cell volume to capture the relevant hydrodynamic scale.[23] Diffraction may vary the energy transfer above or below the average value computed using this ray model if there is a nonlinear CBET response, but the net effect is uncertain given the small spatial and temporal interaction scales involved. *DRACO*'s ray model does not currently track polarization, but the net effect should be captured by assuming an even mixture, given the even distribution of polarization states generated by the polarization smoothing[24] processes on OMEGA.The correct formulation of the net response of polarization, which depends on the ray-interaction angles, is under investigation and may partially account for the overestimated shell kinetic energy. When a multiplier on the CBET gain was added to the model, excellent agreement between the measured and simulated mass ablation rates and shell trajectories was obtained at all angles. These measurements were performed on OMEGA[25] and at the National Ignition Facility (NIF)[26] to access a wide range of laser intensities, plasma conditions, and laser-beam geometries. The need for the CBET multiplier in all the tested configurations suggests that additional physics effects, such as diffraction, polarization effects, or shortcomings of extending the Randall model to 3-D, should be explored to explain the difference in observed and predicted drives.

Experimental Setup

1. Target and Laser Configuration

a. Isolating CBET. Experiments were performed on OMEGA[25] using forty 351-nm laser beams with equal energies, arranged in the polar-direct-drive configuration, with three rings of beams around each pole of the target chamber. The beams were repointed toward the target equator by 5° for the two inner rings of beams and 20° for the outer ring at each pole, using the angle definitions and pointing description from Ref. 27. The beam profiles were shaped with distributed phase plates[28] that provided second-order super-Gaussian laser spots on target (1/*e* radius of 183 μm). Two-dimensional smoothing by spectral dispersion (SSD)[29] and polarization smoothing[24] were used to treat the laser-intensity profiles. The laser pulses consisted of a 0.7-ns foot, ramping up to a 0.6-ns square pulse that drove the target to its final velocity (Fig. 146.2). The total energy on target was varied among 8.1±0.2 kJ ($I \approx 7 \times 10^{14}$ W/cm^2, where I is the peak overlapped intensity defined as the maximum power during the laser pulse divided by the initial surface area of the target), 11.8±0.1 kJ ($I \approx 10 \times 10^{14}$ W/cm^2), and 16.0±0.1 kJ ($I \approx 14 \times 10^{14}$ W/cm^2). The targets were 19.6±0.3-μm-thick spherical CH shells. They were coated with 2.4±0.2, 1.6±0.2, and 0.6±0.2-μm layers of Si, with outer diameters of 639 μm, known to ±1 μm with a variation between experiments of ±4 μm. The density of the Si coating was 2.1±0.2 g/cm^3 but had a significantly smaller variation (<0.2 g/cm^3) within a particular target batch. Each experimental configuration discussed here used targets from a single batch, so the density variation for a particular configuration was negligible.

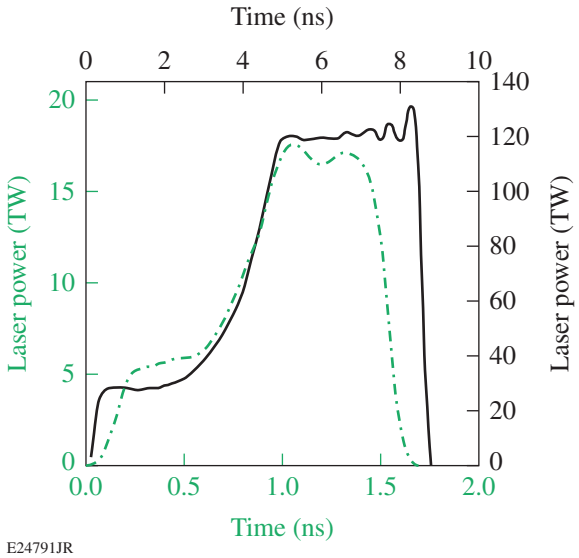

Figure 146.2
The laser pulse shapes are shown for the OMEGA (green dashed–dotted curve) and NIF (black solid curve) experiments.

b. Scaling to ignition conditions. Experiments were performed on the NIF using 192 laser beams (with one beam missing on the 2.5-μm Si experiment) in the indirect-drive configuration, with the polar-direct-drive beam-pointing design

and ring energies described in Ref. 30. This pointing design produced a round CH implosion in simulations when CBET was considered without a gain multiplier. The total laser energy was 660 kJ, giving a peak overlapped intensity on target of $\sim 8 \times 10^{14}$ W/cm^2.

The laser pulse was similar in shape to the OMEGA pulse but extended over 8 ns (Fig. 146.2). Targets were 90±2-μm-thick CH shells with Si coatings of 2.5±0.1 μm and 5±0.1 μm and outer diameters of 2314±2 μm. The density of the Si coating was reported as 2.1±0.2 g/cm^3.

c. Symmetric direct drive on OMEGA. Symmetric direct-drive experiments were performed on OMEGA using all 60 laser beams centered on the target. The same beam-smoothing methods, phase plates, pulse shape, total energies, and intensities were used as in the polar-direct-drive experiments. The targets were also similar to those used in the polar-direct-drive experiments, with 20.1±0.3-μm-thick CH shells having a variation between targets of ±0.8 μm and Si thicknesses of 2.4±0.2, 1.4±0.2, and 0.7±0.2 μm. Outer diameters had an average value of 637 μm, measured to ±2 μm, and a variation between targets of ±11 μm. The density of the Si coating was reported as 2.1±0.2 g/cm^3.

2. Self-Emission Diagnostic

a. Configuration of the x-ray framing camera. The x-ray self-emission was measured using four-strip x-ray framing cameras.[31,32] Two-dimensional images of the coronal x rays were formed using arrays of pinholes (8-μm diameter for OMEGA, 25-μm diameter for the NIF), placed to give 6× magnifications on OMEGA and 2× on the NIF. The ~50-ps time-gated images (~100 ps for the NIF) were taken throughout the implosion, with absolute timing known to ±10 ps and the interstrip timing of ~250 ps known to ±3 ps (Ref. 33). Five filters were used for the images throughout the course of the experiments: (1) 25 μm of Be, (2) 250 μm of Be, (3) 25 μm of Be with 23 μm of Saran, (4) 25 μm of Be with 50 μm of Kapton, and (5) 25 μm of Be with 75 μm of Kapton. Different filters were used to optimize imaging of the ablation front and the interface between the Si and CH in the corona. The 25-μm Be filter (blocking x rays <1 keV) was found to optimally image the CH ablation front late in time because of the lower ablation-front temperature. The 250-μm Be filter (blocking x rays <2 keV) was optimized to image the Si/CH interface as it expanded away from the ablation front because of the higher temperature in the corona. The combination of Be and Saran (blocking x rays <1.6 keV) provided a good compromise between the two. The Be and Kapton filters (blocking x rays <2 keV) were used on the NIF for the first three strips on each camera. Only 25 μm of Be was used for the last strip in each camera to measure the CH ablation-front position. Images were taken from the equator and pole for all of the polar-direct-drive experiments, so that both the variation in ablation rate and ablation-front trajectory with polar angle and the azimuthal symmetry of the implosion could be observed. Both configurations on OMEGA experiments had two equatorial cameras offset by 11° in polar angle from the equator and one camera on the pole to measure the azimuthal symmetry. The NIF experiments had one camera on the equator and one on the pole.

b. Trajectory measurements. X-ray self-emission images of Si-coated CH target implosions were used to determine the mass ablation rate of Si and the ablation-front trajectory of the target.[34,35] While the laser is on, the coronal plasma around the target is continually heated and emits soft x rays. The x-ray intensity that is line integrated through the target is imaged through a pinhole onto a time-gating diagnostic plane. Figure 146.3 shows the x-ray self-emission technique at a time shortly after the laser burned through the Si layer of the target, when the corona consists of an outer Si plasma and an inner CH plasma surrounding the unablated target.

Figure 146.3(b) shows the simulated x-ray intensity profile at the diagnostic plane when two distinct features are observed. Moving from the outside of the plasma toward the target center, an increase in x-ray intensity is observed as the line-integrated distance through the Si plasma increases. A rapid drop in intensity occurs at the interface between the Si and CH as the lower-emitting CH quickly dominates the integrated x-ray emission region (outer feature). The intensity again increases with further progress toward the center of the target until the ablation front is reached. At the ablation front, the emission quickly drops because the shell is optically thick (inner feature). These two features observed in the radial intensity at the diagnostic plane are used to track the positions of the Si/CH interface and ablation front.[35]

Figure 146.4 shows measured x-ray self-emission images and their respective intensity profiles at three different times for a symmetrically illuminated implosion. In the symmetric images, these profiles are angularly averaged around 360° of the image to obtain a measurement accurate to <1 μm for both the inner gradient (ablation-front radius) and outer peak locations (Si/CH interface position). In angularly resolved images, the profiles at the pole and equator are each averaged over 40° (20° at each pole or each side of the equator). The instrument function of the x-ray diagnostic (defined predominantly by the pinhole size)

introduced a small systematic shift (~2 μm) between the position of the inner gradient and the actual position of the ablation front.[35] This shift was determined by post-processing simulations with *Spect3D*[36] and convolving with the instrument function to calculate self-emission images. The shifts are known to ±1 μm for the ablation front and ±2 μm for the Si/CH interface.

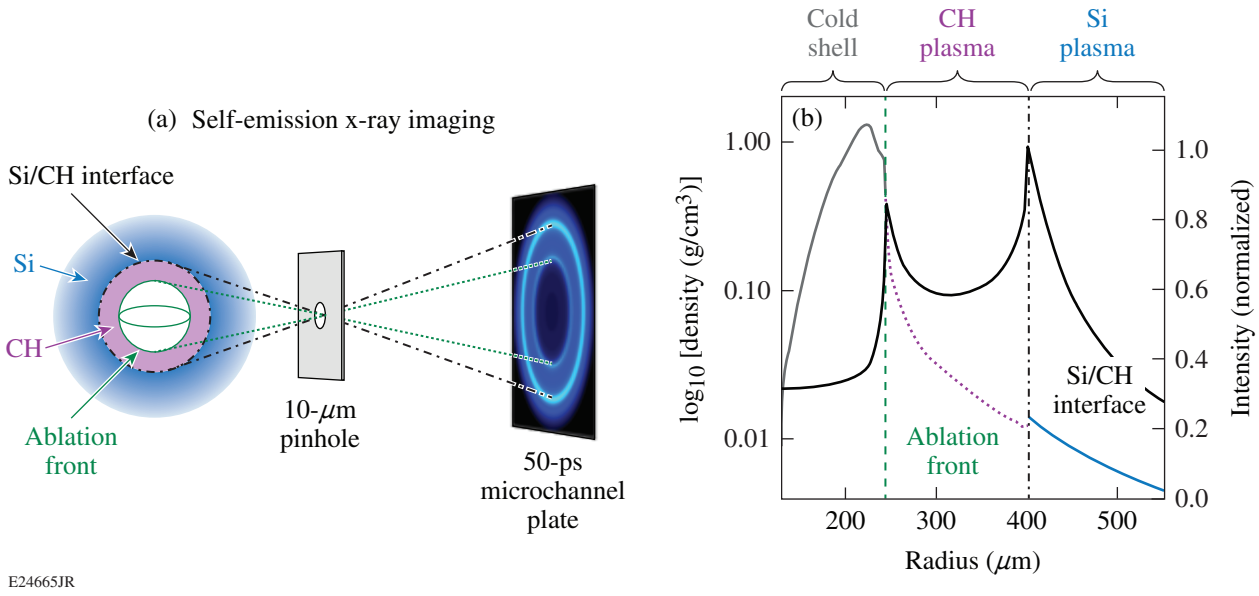

Figure 146.3

(a) Line-integrated x-ray self-emission from the target is imaged through a pinhole and filter (transmits >1 keV) onto an ~50-ps time-gated microchannel plate. (b) Comparison of the calculated radial x-ray intensity profile measured at the diagnostic plane (black solid curve) with the simulated target-density profile in the cold shell (gray solid curve), in the CH plasma (purple dotted curve), and in the Si plasma (blue solid curve). Two peaks in the emission correspond to the positions of the Si/CH interface in the coronal plasma (black dashed–dotted line) and the ablation front of the imploding shell (green dashed line). No instrument function is included in the x-ray intensity profile calculation to illustrate the steep gradients at the ablation surface and Si/CH interface.

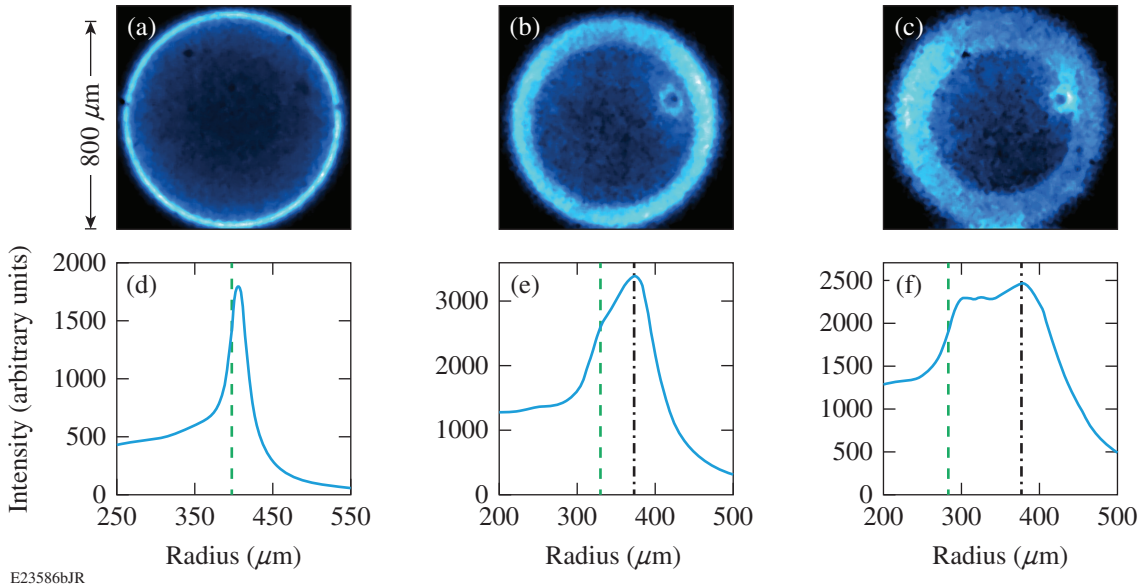

Figure 146.4

Self-emission x-ray images, taken (a) before and [(b),(c)] at two different times shortly after the laser burns through the Si layer, are shown with their corresponding averaged radial profiles. The positions of the measured ablation front (green dashed line) and the Si/CH interface (black dashed–dotted line) are included.

c. Measurements of mass ablation rate. The average mass ablation rate of the Si from the start of the laser pulse to the Si burnthrough time is determined by dividing the total ablated mass (calculated from the initial Si mass) by the time it took the laser to burn through the Si layer. The time-resolved mass ablation rate was determined by varying the thickness of the Si outer layer to determine the time-averaged mass ablation rate at different times during the implosion.

To determine the burnthrough time in each experiment, the measured Si/CH interface and ablation-front positions from the series of images taken for a particular implosion were plotted to generate the ablation-front and Si/CH interface trajectories. The burnthrough time of the Si layer corresponds to the time when the Si/CH interface trajectory separates from the ablation-front trajectory. To accurately determine the burnthrough time, a range of simulations was performed, varying the CBET multiplier. The simulation that simultaneously reproduced both measured trajectories was used to determine the Si burnthrough times around the target. The accuracy of the measurement corresponds to the variation in the burnthrough time for the simulated trajectories that are within the error bars of the experimental measurements.

The Si/CH interface trajectory is sensitive to the initial Si mass. For all experiments in a given target batch, the optimum Si density used in the simulations was determined by finding the density that minimized the differences between the simulated and measured interface trajectories at the pole. The density was varied within the measurement uncertainties (see **Isolating CBET**, below). The absolute error in the mass largely results from the uncertainty in density. This inaccuracy in the calculated mass could mask uncertainties in the equation of state, opacity, and thermal-transport models, but tests show that these effects primarily act symmetrically. Any changes in the models that affect the trajectories symmetrically must be offset by changes in another symmetric coupling model—not the CBET model—to maintain agreement with the measured polar trajectories.

Experiments

1. Isolating CBET

To measure the effects of CBET in direct-drive experiments on OMEGA, a laser configuration was used in which a ring of beams around the equator was turned off and the remaining beams were repointed toward the equator. This configuration limits the intensity of the refracted outgoing light that interacts with incoming polar beams, significantly reducing CBET at the pole. The repointing increases the flux of unabsorbed light propagating through the equatorial coronal plasma, which enhances CBET at the equator (Fig. 146.1). The implosions were designed to have nearly uniform drive around the target when CBET was not taken into consideration, so differences in measured drive between the pole and equator are attributed to CBET.

Figure 146.5 shows x-ray self-emission images taken from the equator after the laser burns through the Si layer. The intensity features visible in the images show the positions of the ablation front and Si/CH interface, which form two concentric ellipses with opposite ellipticity. The ablation-front ellipses show larger shell radii at the equator compared to the pole, demonstrating that the ablation pressure is lower at the equator compared to the pole. The smaller separations between the Si/CH interface and ablation-front ellipses at the equator,

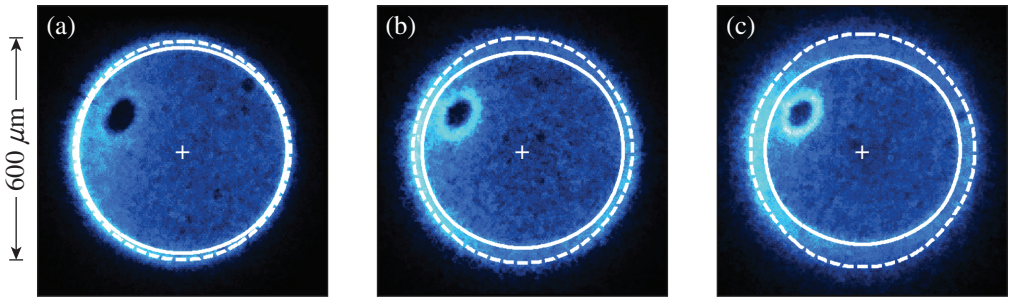

Figure 146.5
X-ray images taken after the burnthrough of a thin Si layer at (a) $t = 0.7$, (b) 0.8, and (c) 0.9 ns in an experiment having the highest intensity (14×10^{14} W/cm^2) are shown. The images indicate earlier burnthrough at the poles of the target (top and bottom of images) than at the equator. The increased separation of the Si/CH interface (dotted line) and ablation front (solid line) at the poles implies a greater time of expansion for the Si from the ablation front. This increased drive results in a smaller ablation-front radius measured at the pole than at the equator.

compared to the pole, indicate that the laser burned through the Si later at the equator. The expansion of the Si/CH interface away from the target and compression of the ablation front as a function of time can be seen through the series of images.

Figure 146.6 shows the ablation-front and interface trajectories used to determine the Si burnthrough times, i.e., the time that each trajectory pair separated with values of 0.59±0.04 ns for the equator and 0.52±0.04 ns for the pole. The later burnthrough time at the equator, compared to the pole, agrees with the lower mass ablation rate at the equator suggested by the individual images. The measured ablation-front radii of 140±2 μm for the equator and 111±2 μm for the pole at 1.49±0.01 ns indicate a lower average ablation pressure at the equator compared to the pole, which leads to a slower velocity.

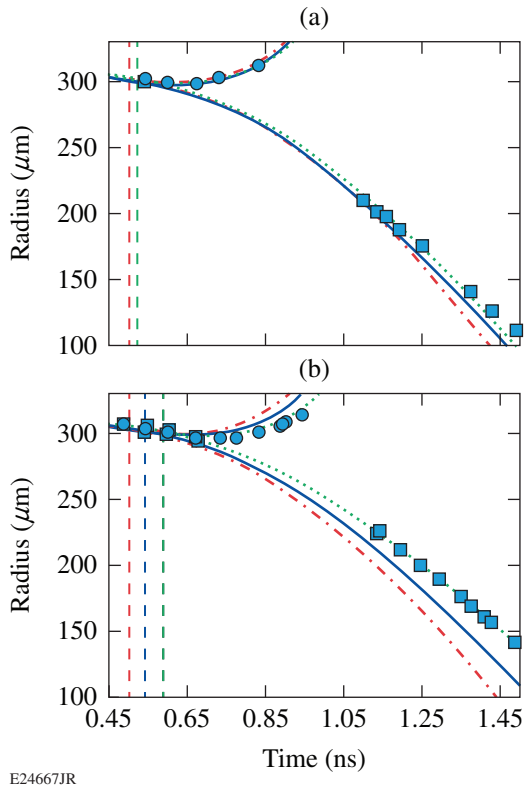

Figure 146.6
Measured Si/CH interface (blue circles) and ablation-front (blue squares) trajectories from three cameras are plotted for the (a) pole and (b) equator for the highest-intensity OMEGA polar-drive experiment with a 2.4-μm layer of Si. Error bars for the radius measurements are smaller than the data points (±2 μm for the ablation-front measurements and ±4 μm for the Si/CH interface measurements). Simulations performed with no CBET model (red dashed–dotted curve), the standard CBET model (blue solid curve), and the CBET model with the best-fitting gain multiplier (green dotted curve; $f_{\mathrm{CBET}} = 2.7$) are shown. The time that the laser burned through the Si in each simulation is marked with a dashed line of the corresponding color. Good agreement between the measurements and all models was obtained at the pole where CBET was minimal.

a. Comparison with hydrodynamic simulations. Figure 146.6 shows good agreement between the trajectory measurements at the pole and polar trajectories taken from *DRACO*[21] simulations that did not include CBET. This agreement at the pole suggests that the coupling physics is well modeled when CBET effects are small. Calculated trajectories at the equator are very similar to those calculated at the pole, which suggests that without CBET, the implosion would be symmetric. However, the measured equatorial trajectories show later burnthrough and a larger final radius than were calculated, indicating that the CBET significantly reduced the drive at this location.

A 3-D ray-based model[23] adapted from the 1-D Randall plane-wave equations[4] was implemented in *DRACO*. Figure 146.6 shows that simulations run with this model calculate a preferential decrease in drive at the equator, bringing simulations into better agreement with measurements. The addition of this CBET model results in small changes in the calculated polar trajectories at early times, verifying that CBET is negligible at the pole until the target radius is $\lesssim$250 μm (~0.9 ns). An increased effect of CBET at the pole is observed at this point because of an increase in the SBS seeds from rays that were previously shadowed by the target and an increase in the incident laser power (Fig. 146.2). Even late in time, however, the ablation-front trajectories calculated without CBET are in reasonable agreement with the measurements.

The trajectories at the equator are slowed to a greater degree than at the poles, indicating that CBET has a stronger effect at this location. The simulated Si burnthrough time is still too early and the ablation-front trajectory still too fast, however, to agree with the measurements. To estimate the CBET modification required to bring simulations into agreement with measurements, a multiplier (f_{CBET}) was incorporated into the CBET gain length:

$$L_{\mathrm{s}}^{-1} = f_{\mathrm{CBET}} \frac{k_0}{4} \frac{n_0}{\epsilon n_{\mathrm{c}}} \left(\frac{m v_q^2}{T_{\mathrm{e}}} \right) \times \left[\left(1 + \frac{3 T_{\mathrm{i}}}{Z T_{\mathrm{e}}} \right) \left(\frac{\nu_{\mathrm{i}}}{\omega_{\mathrm{s}}} \right) \right]^{-1} P(\eta), \quad (1)$$

given by Eq. (18) in Ref. 4, where all other parameters are defined within the reference.

Figure 146.6 shows that excellent agreement with the measurements was obtained when a multiplier of 2.6±0.3 was used. To determine the optimal multiplier, a χ^2 analysis was used to minimize the differences between measured and simulated trajectories (Fig. 146.7), where

$$\chi^2 = \sum_{i=1}^{N} \frac{1}{N} \frac{\left[r_i - x(t_i)\right]^2}{\sigma_{r_i}^2}, \tag{2}$$

and r_i is the measured position, $x(t_i)$ is the simulated radius, σ_{r_i} is the uncertainty in the experimental measurement (±2 μm for the ablation-front location and ±4 μm for the Si/CH interface position), and N is the total number of points measured. The error bar on the multiplier was determined from the uncertainty in absolute timing (±10 ps)—shifting the experimental image timing relative to the simulation gives an error bar on the multiplier of ±0.4 ps for high intensities to ±0.6 ps for each low-intensity experiment.

All of the simulations described here were performed using the code *DRACO* with the iSNB nonlocal thermal-transport model,[22] *SESAME* equation-of-state tables,[37] and collisional-radiative opacity tables.[38] The polar angle's dependence on the laser energy deposition, hydrodynamic efficiency, and thermal conduction is generated by the polar-direct-drive configuration, which invokes lateral thermal transport.

b. Intensity and Si-thickness scalings. Figure 146.7 shows measurements of the polar and equatorial trajectories for the 2.4-μm Si experiment at three intensities. For each intensity, simulations without CBET agreed well with experimental measurements at the pole, showing that the simulations reproduce

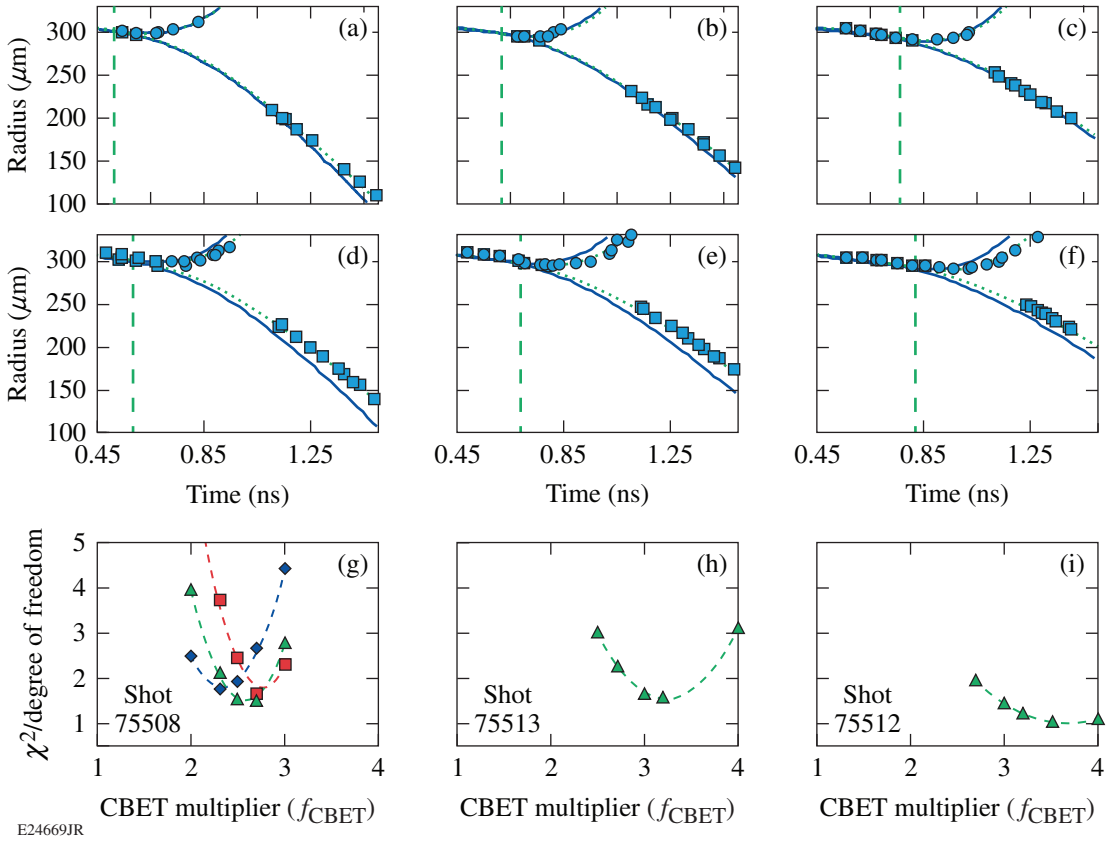

Figure 146.7
Comparison of the measured ablation front (blue squares) and Si/CH interface (blue circles) with simulated trajectories generated by *DRACO* with CBET using no multiplier (blue solid curves) and CBET with the best-fit multiplier (green dotted curves) for targets with 2.5 μm of Si. Included are trajectories for [(a)–(c)] the pole and [(d)–(f)] equator for $I = 14 \times 10^{14}$ W/cm^2 (left column), 10×10^{14} W/cm^2 (middle column), and 7×10^{14} W/cm^2 (right column). The Si burnthrough times are plotted (green dashed lines). The χ^2 minimization analyses are plotted for (g) $I = 14 \times 10^{14}$ W/cm^2, (h) 10×10^{14} W/cm^2, and (i) 7×10^{14} W/cm^2 to determine the optimal multiplier and error bars. For the highest intensity, the χ^2 values are shown for the optimal timing (green triangles), –10 ps (blue diamonds), and +10 ps (red squares). The possible error in the CBET multiplier is determined from the shift in the location of the minimum χ^2 with the uncertainty in the timing.

the hydrodynamic coupling when CBET is negligible, but the ablation rate and ablation-front velocity are overpredicted at the equator. With the introduction of the CBET model using the optimized multiplier, excellent agreement at both the pole and equator was found for each intensity. The optimized values of 2.8±0.5, 3.1±0.5, and 3.9±1.0 were determined for this configuration with overlap intensities of $I = 14 \times 10^{14}$ W/cm^2, 10×10^{14} W/cm^2, and 7×10^{14} W/cm^2, respectively. As the intensity decreases, the χ^2 curve broadens because of the smaller effect of CBET at lower intensities.

Figure 146.8 shows the mass-ablation-rate measurements at the pole and the equator for the highest laser-intensity experiments. The experiments were performed using three different thicknesses of the Si outer layer (0.6, 1.6, and 2.4 μm) to evaluate the average mass ablation rate of the Si at different times during the implosion. For three intensities, good agreement between simulated and experimental burnthrough times verifies the simulated time-resolved mass ablation rates taken when the optimal intensity multiplier was used.

2. Scaling to Ignition Conditions

Figure 146.9 shows the trajectory results from direct-drive experiments performed on the NIF to access ignition-relevant conditions (Table 146.I). The images taken during the NIF experiments were used to measure the ablation-front trajectories at the pole and the equator. Measured ablation-front trajectories agree well with simulations that used a CBET multiplier

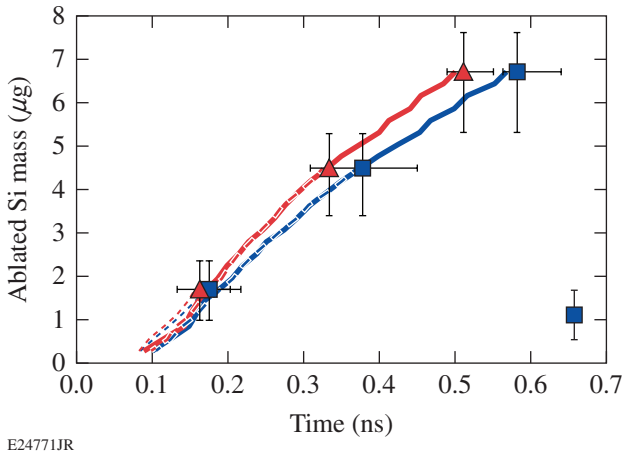

Figure 146.8
Ablated Si mass as a function of the measured burnthrough time at the pole (red triangles) and equator (blue squares) for a laser intensity of 14×10^{14} W/cm^2 is compared with simulations (dotted curve: 0.6 μm; dashed curve: 1.6 μm; and solid curve: 2.4 μm) using the optimal multipliers. The small shot-to-shot variations in the simulated ablation rate result from minor variations in the laser pulse and target size. Absolute error bars are shown for the Si mass. The relative error in mass (shown on the sample point in the lower right corner) is reduced because the density can be considered to be the same for all targets in a given batch.

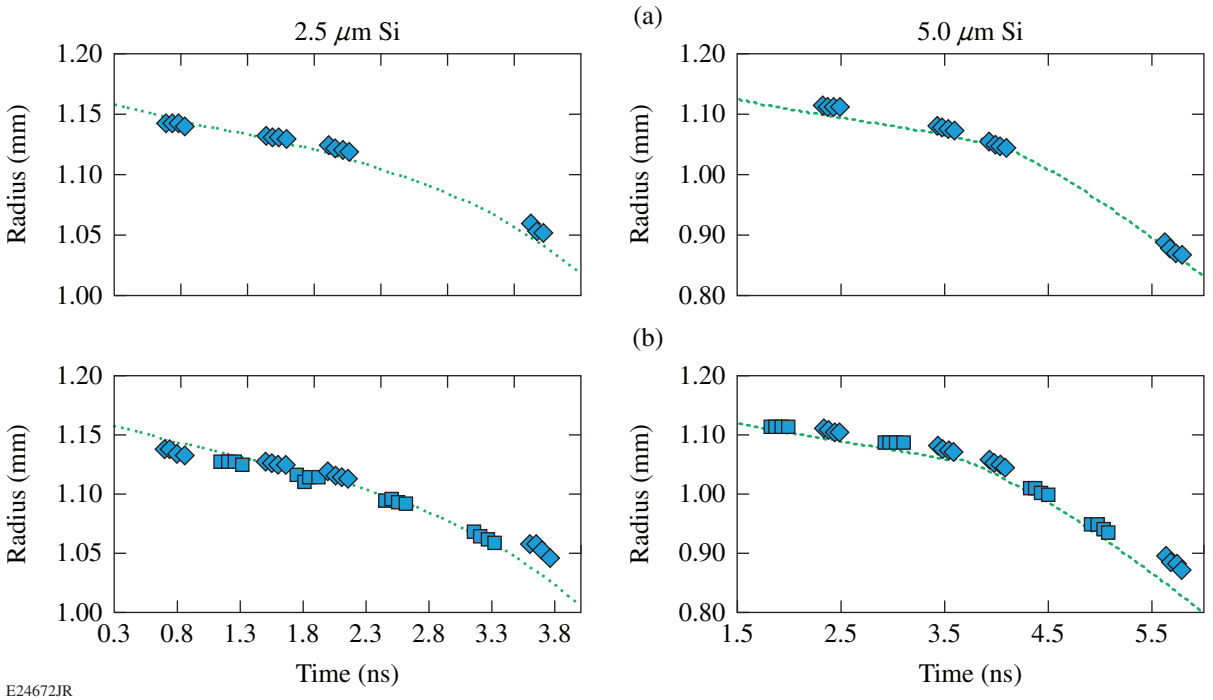

Figure 146.9
The measured ablation-front positions (blue squares) are compared with simulations (green dotted curves) for targets with [(a),(b)] 2.5 μm and [(c),(d)] 5 μm of Si at the [(a),(c)] pole and [(b),(d)] equator.

of 2, which has been shown for similar NIF experiments that used CH shells.[39] To mitigate the effects of shell decompression on the ablation-front trajectories, the experiments were limited to early times. Large perturbations at the ablation front can expand the ablation-front surface away from the shell's center of mass.[39] In the OMEGA experiments, the 2-D SSD limits the imprint, and perturbations were shown to have minimal impact on the trajectories.[35] At both facilities the radiation from the Si layer reduced the Rayleigh–Taylor (RT) growth, but on the NIF, the RT growth caused by high levels of laser imprint occurred in spite of the smoothing effects; this mixed the Si and CH at the interface, reducing the contrast of the outer interface peak in the x-ray images. As a result, the ability to measure the Si/CH interface trajectory on the NIF was limited.

Table 146.I: Comparison of the laser energy (E_L), electron temperature at the quarter-critical surface (T_e), density scale length (L_n), and overlap intensity at the quarter-critical surface (I_{qc}) near the end of the laser pulse for OMEGA and NIF polar-direct-drive experiments.

Parameter	OMEGA	NIF	Ignition
E_L	24 kJ	660 kJ	1500 kJ
T_e	2.7 keV	2.9 keV	4 keV
L_n	150 μm	350 μm	500 μm
I_{qc}	5×10^{14} W/cm^2	3×10^{14} W/cm^2	10^{15} W/cm^2

3. Symmetric Direct Drive on OMEGA

Figure 146.10 shows the trajectory results for symmetric direct-drive experiments on OMEGA. A CBET gain multiplier

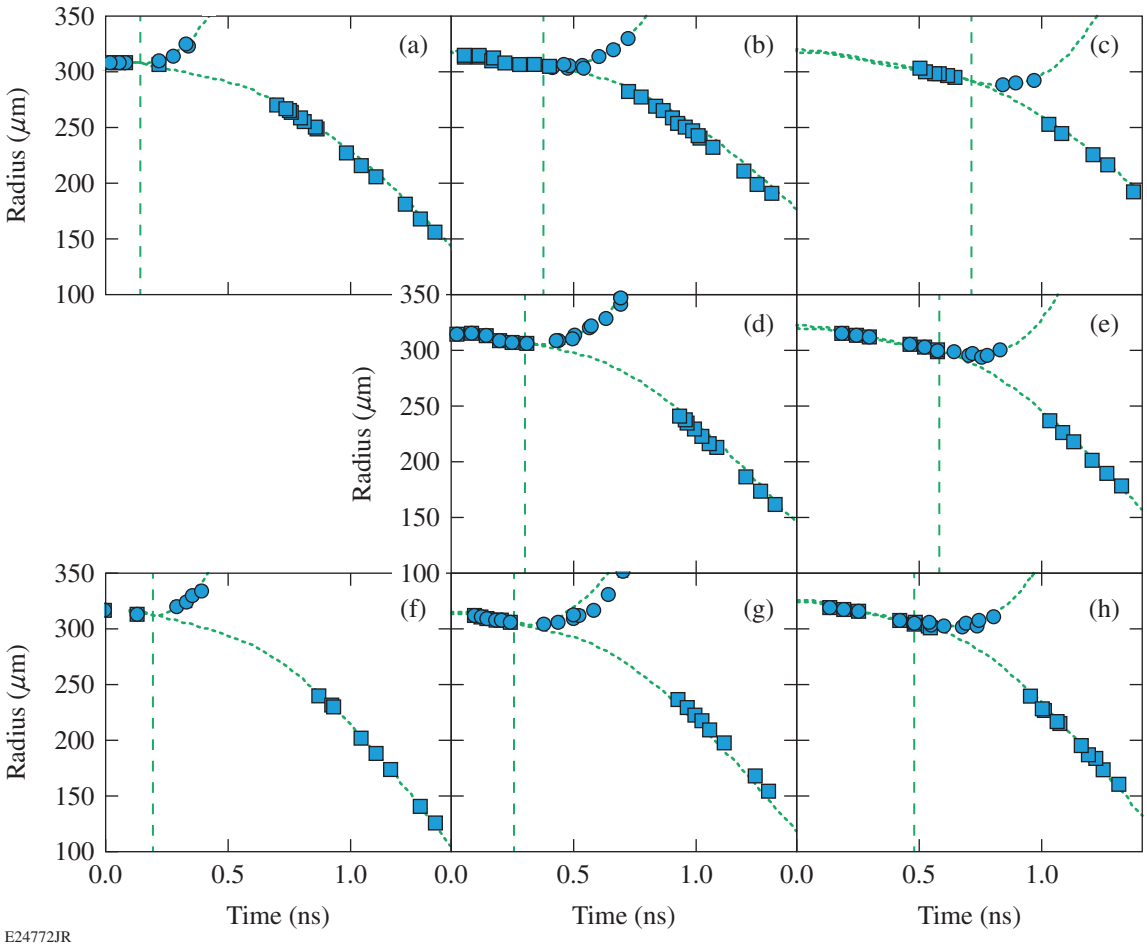

Figure 146.10
Comparison of the measured ablation-front (blue squares) and Si/CH interface (blue circles) positions with simulated trajectories (green dotted curve) for [(a)–(c)] $I = 7 \times 10^{14}$ W/cm^2; [(d),(e)] 10×10^{14} W/cm^2; and [(f)–(h)] 14×10^{14} W/cm^2 for targets with Si thicknesses of [(a),(f)] 0.7 μm; [(b),(d),(g)] 1.6 μm; and [(c),(e),(h)] 2.6 μm. The Si burnthrough times are plotted in the figure (green dashed lines).

of 2 was found to reproduce the trajectories and burnthrough times (mass ablation rates) for all combinations of laser intensity and Si thickness tested.

Conclusions

The CBET physics in direct-drive implosions was analyzed using simultaneous 2-D Si mass-ablation-rate and ablation-front-trajectory measurements. A polar-direct-drive configuration was employed, where beams were removed from the equator of a symmetrically illuminated target and the remaining beams were repointed toward the equator. This configuration suppressed CBET at the pole, while enhancing its effects at the equator. Implosion trajectories simulated without CBET were in good agreement with the measured polar trajectories for all conditions tested. This suggests that the other coupling physics is well modeled at the pole when CBET is small. The calculated mass ablation rates and ablation-front trajectories are in excellent agreement with the measurements at the pole and the equator when a 3-D ray-based CBET model is included in the simulations with a CBET gain multiplier. These measurements were performed on both OMEGA and the NIF to access a wide range of laser intensities, plasma conditions, and laser-beam geometries. The multiplier was necessary for all laser conditions, and the optimal multiplier for each configuration is shown in Fig. 146.11. The multiplier is constant for symmetric OMEGA experiments and decreases with increasing intensity in OMEGA polar-direct-drive implosions. The presence of the CBET gain multiplier required to match the data in all of the configurations tested suggests that additional physics effects should be explored, such as intensity variations caused by diffraction, polarization effects, or shortcomings of extending the 1-D Randall model to 3-D. The variation in the CBET multiplier in the polar-drive configuration, while it is constant in the symmetric configuration, suggests that additional physics may be affecting the polar-drive implosions. For example, the beams pointed toward the equator may experience increased CBET because of their increased interaction length. This increased transfer may saturate at high laser intensities, resulting in a decreasing CBET multiplier. Another candidate for further exploration is the effect of lateral thermal transport on the plasma conditions since the polar-drive configuration experiences lateral temperature gradients that do not exist in a symmetric configuration and the plasma conditions affect the level of energy transfer.

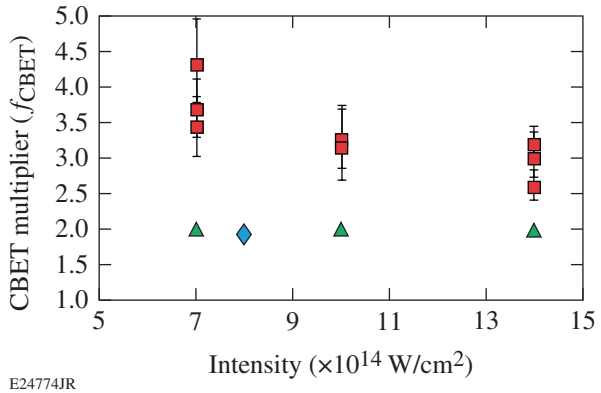

Figure 146.11
CBET multipliers that minimize the χ^2 difference between simulations and measurements are shown as a function of peak laser intensity for OMEGA symmetric direct-drive (green triangles) and polar-direct-drive (red squares) experiments and NIF experiments (blue diamond).

ACKNOWLEDGMENT

The authors thank the operations teams at both the Omega Laser Facility and the National Ignition Facility for their outstanding work. This work was supported by the U.S. Department of Energy Office of Inertial Confinement Fusion under Award Number DE-NA0001944, the University of Rochester, and the New York State Energy Research and Development Authority. The support of DOE does not constitute an endorsement by DOE of the views expressed in this article.

REFERENCES

1. J. Nuckolls *et al.*, Nature **239**, 139 (1972).
2. S. Atzeni and J. Meyer-ter-Vehn, *The Physics of Inertial Fusion: Beam Plasma Interaction, Hydrodynamics, Hot Dense Matter*, International Series of Monographs on Physics (Clarendon Press, Oxford, 2004).
3. W. L. Kruer *et al.*, Phys. Plasmas **3**, 382 (1996).
4. C. J. Randall, J. R. Albritton, and J. J. Thomson, Phys. Fluids **24**, 1474 (1981).
5. W. Seka, D. H. Edgell, J. P. Knauer, J. F. Myatt, A. V. Maximov, R. W. Short, T. C. Sangster, C. Stoeckl, R. E. Bahr, R. S. Craxton, J. A. Delettrez, V. N. Goncharov, I. V. Igumenshchev, and D. Shvarts, Phys. Plasmas **15**, 056312 (2008).
6. I. V. Igumenshchev, W. Seka, D. H. Edgell, D. T. Michel, D. H. Froula, V. N. Goncharov, R. S. Craxton, L. Divol, R. Epstein, R. Follett, J. H. Kelly, T. Z. Kosc, A. V. Maximov, R. L. McCrory, D. D. Meyerhofer, P. Michel, J. F. Myatt, T. C. Sangster, A. Shvydky, S. Skupsky, and C. Stoeckl, Phys. Plasmas **19**, 056314 (2012).
7. D. H. Froula, I. V. Igumenshchev, D. T. Michel, D. H. Edgell, R. Follett, V. Yu. Glebov, V. N. Goncharov, J. Kwiatkowski, F. J. Marshall, P. B. Radha, W. Seka, C. Sorce, S. Stagnitto, C. Stoeckl, and T. C. Sangster, Phys. Rev. Lett. **108**, 125003 (2012).
8. R. K. Kirkwood *et al.*, Phys. Rev. Lett. **76**, 2065 (1996).
9. W. Seka, H. A. Baldis, J. Fuchs, S. P. Regan, D. D. Meyerhofer, C. Stoeckl, B. Yaakobi, R. S. Craxton, and R. W. Short, Phys. Rev. Lett. **89**, 175002 (2002).
10. S. H. Glenzer *et al.*, Science **327**, 1228 (2010).

11. N. B. Meezan *et al.*, Phys. Plasmas **17**, 056304 (2010).

12. P. Michel *et al.*, Phys. Plasmas **17**, 056305 (2010).

13. P. Michel *et al.*, Phys. Plasmas **20**, 056308 (2013).

14. D. T. Michel, S. Depierreux, C. Stenz, V. Tassin, and C. Labaune, Phys. Rev. Lett. **104**, 255001 (2010).

15. D. Turnbull *et al.*, Phys. Rev. Lett. **114**, 125001 (2015).

16. I. V. Igumenshchev, D. H. Edgell, V. N. Goncharov, J. A. Delettrez, A. V. Maximov, J. F. Myatt, W. Seka, A. Shvydky, S. Skupsky, and C. Stoeckl, Phys. Plasmas **17**, 122708 (2010).

17. D. T. Michel, V. N. Goncharov, I. V. Igumenshchev, R. Epstein, and D. H. Froula, Phys. Rev. Lett. **111**, 245005 (2013).

18. S. Skupsky, J. A. Marozas, R. S. Craxton, R. Betti, T. J. B. Collins, J. A. Delettrez, V. N. Goncharov, P. W. McKenty, P. B. Radha, T. R. Boehly, J. P. Knauer, F. J. Marshall, D. R. Harding, J. D. Kilkenny, D. D. Meyerhofer, T. C. Sangster, and R. L. McCrory, Phys. Plasmas **11**, 2763 (2004).

19. D. H. Edgell, P. B. Radha, D. H. Froula, V. N. Goncharov, I. V. Igumenshchev, J. F. Myatt, and W. Seka, presented at the 42nd Annual Anomalous Conference, Key West, FL, 25–29 June 2012.

20. J. A. Marozas, T. J. B. Collins, P. W. McKenty, and J. D. Zuegel, presented at the 57th Annual Meeting of the APS Division of Plasma Physics, Savannah, GA, 16–20 November 2015.

21. P. B. Radha, T. J. B. Collins, J. A. Delettrez, Y. Elbaz, R. Epstein, V. Yu. Glebov, V. N. Goncharov, R. L. Keck, J. P. Knauer, J. A. Marozas, F. J. Marshall, R. L. McCrory, P. W. McKenty, D. D. Meyerhofer, S. P. Regan, T. C. Sangster, W. Seka, D. Shvarts, S. Skupsky, Y. Srebro, and C. Stoeckl, Phys. Plasmas **12**, 056307 (2005).

22. D. Cao, G. Moses, and J. Delettrez, Phys. Plasmas **22**, 082308 (2015).

23. J. A. Marozas, T. J. B. Collins, J. D. Zuegel, P. B. Radha, F. J. Marshall, and W. Seka, presented at the 44th Annual Anomalous Absorption Conference, Estes Park, CO, 8–13 June 2014.

24. T. R. Boehly, V. A. Smalyuk, D. D. Meyerhofer, J. P. Knauer, D. K. Bradley, R. S. Craxton, M. J. Guardalben, S. Skupsky, and T. J. Kessler, J. Appl. Phys. **85**, 3444 (1999).

25. T. R. Boehly, D. L. Brown, R. S. Craxton, R. L. Keck, J. P. Knauer, J. H. Kelly, T. J. Kessler, S. A. Kumpan, S. J. Loucks, S. A. Letzring, F. J. Marshall, R. L. McCrory, S. F. B. Morse, W. Seka, J. M. Soures, and C. P. Verdon, Opt. Commun. **133**, 495 (1997).

26. E. M. Campbell and W. J. Hogan, Plasma Phys. Control. Fusion **41**, B39 (1999).

27. P. B. Radha, J. A. Marozas, F. J. Marshall, A. Shvydky, T. J. B. Collins, V. N. Goncharov, R. L. McCrory, P. W. McKenty, D. D. Meyerhofer, T. C. Sangster, and S. Skupsky, Phys. Plasmas **19**, 082704 (2012).

28. Y. Lin, T. J. Kessler, and G. N. Lawrence, Opt. Lett. **21**, 1703 (1996).

29. S. Skupsky, R. W. Short, T. Kessler, R. S. Craxton, S. Letzring, and J. M. Soures, J. Appl. Phys. **66**, 3456 (1989).

30. M. Hohenberger, P. B. Radha, J. F. Myatt, S. LePape, J. A. Marozas, F. J. Marshall, D. T. Michel, S. P. Regan, W. Seka, A. Shvydky, T. C. Sangster, J. W. Bates, R. Betti, T. R. Boehly, M. J. Bonino, D. T. Casey, T. J. B. Collins, R. S. Craxton, J. A. Delettrez, D. H. Edgell, R. Epstein, G. Fiksel, P. Fitzsimmons, J. A. Frenje, D. H. Froula, V. N. Goncharov, D. R. Harding, D. H. Kalantar, M. Karasik, T. J. Kessler, J. D. Kilkenny, J. P. Knauer, C. Kurz, M. Lafon, K. N. LaFortune, B. J. MacGowan, A. J. Mackinnon, A. G. MacPhee, R. L. McCrory, P. W. McKenty, J. F. Meeker, D. D. Meyerhofer, S. R. Nagel, A. Nikroo, S. Obenschain, R. D. Petrasso, J. E. Ralph, H. G. Rinderknecht, M. J. Rosenberg, A. J. Schmitt, R. J. Wallace, J. Weaver, C. Widmayer, S. Skupsky, A. A. Solodov, C. Stoeckl, B. Yaakobi, and J. D. Zuegel, Phys. Plasmas **22**, 056308 (2015).

31. D. K. Bradley, P. M. Bell, J. D. Kilkenny, R. Hanks, O. Landen, P. A. Jaanimagi, P. W. McKenty, and C. P. Verdon, Rev. Sci. Instrum. **63**, 4813 (1992).

32. D. K. Bradley *et al.*, Rev. Sci. Instrum. **66**, 716 (1995).

33. D. T. Michel, A. K. Davis, W. Armstrong, R. Bahr, R. Epstein, V. N. Goncharov, M. Hohenberger, I. V. Igumenshchev, R. Jungquist, D. D. Meyerhofer, P. B. Radha, T. C. Sangster, C. Sorce, and D. H. Froula, High Power Laser Science and Engineering **3**, e19 (2015).

34. D. T. Michel, C. Sorce, R. Epstein, N. Whiting, I. V. Igumenshchev, R. Jungquist, and D. H. Froula, Rev. Sci. Instrum. **83**, 10E530 (2012).

35. A. K. Davis, D. T. Michel, S. X. Hu, R. S. Craxton, R. Epstein, V. N. Goncharov, I. V. Igumenshchev, T. C. Sangster, and D. H. Froula, Rev. Sci. Instrum. **85**, 11D616 (2014).

36. J. J. MacFarlane *et al.*, High Energy Density Phys. **3**, 181 (2007).

37. B. I. Bennett, J. D. Johnson, G. I. Kerley, and G. T. Rood, Los Alamos National Laboratory, Los Alamos, NM, Report LA-7130 (1978).

38. H. Takabe and T. Nishikawa, J. Quant. Spectrosc. Radiat. Transf. **51**, 379 (1994).

39. P. B. Radha, M. Hohenberger, D. H. Edgell, J. A. Marozas, F. J. Marshall, D. T. Michel, M. J. Rosenberg, W. Seka, A. Shvydky, T. R. Boehly, T. J. B. Collins, E. M. Campbell, R. S. Craxton, J. A. Delettrez, S. N. Dixit, J. A. Frenje, D. H. Froula, V. N. Goncharov, S. X. Hu, J. P. Knauer, R. L. McCrory, P. W. McKenty, D. D. Meyerhofer, J. F. Myatt, R. D. Petrasso, S. P. Regan, T. C. Sangster, H. Sio, S. Skupsky, and A. Zylstra, Phys. Plasmas **23**, 056305 (2015).

Time-Multiplexed Pulse Shaping

Introduction

Optical pulses are used to transmit information, perform remote sensing and metrology, and study physical processes in matter. These optics and photonics applications require the generation of pulses with control of their temporal characteristics, i.e., instantaneous power, timing, phase, and frequency variations over the pulse shape. Numerous techniques can be used to generate high-bandwidth optical waveforms.[1–8] Direct time-domain generation using high-bandwidth modulators is common in telecommunication applications and has benefited from the progress of high-bandwidth, direct-digital-signal synthesis and amplification. Commercial arbitrary waveform generators (AWG's) with an analog bandwidth higher than 10 GHz, sampling rates up to 65 GS/s, and a sampling depth of 8 bits can be used to drive electro-optic modulators and generate high-resolution optical waveforms.[9,10]

The precise generation of shaped optical waveforms is paramount to high-energy lasers that must deliver on-target pulse shapes optimized for laser–matter interaction. The front end of these facilities must generate optical pulses with low relative jitter and high-bandwidth pulse-shape control. The National Ignition Facility (NIF) (192 high-energy beams) uses 48 AWG's to precisely shape 48 seed pulses sent along distinct optical paths that include optical amplification, frequency conversion, beam smoothing, and focusing.[11,12] Full deployment of the Laser Mégajoule Facility (240 high-energy beams) will require 60 pulse-shaping units to precisely shape 60 seed pulses.[13]

This article presents a time-multiplexed pulse-shaping (TMPS) system generating up to eight synchronized optical waveforms that can be sent to eight distinct optical systems, e.g., sequences of optical amplifiers. A single pulse-shaping unit composed of an AWG and an electro-optic modulator generates a waveform composed of the shaped optical waveforms in different time slots. These waveforms are demultiplexed by a precisely calibrated $LiNbO_3$ 1×8 demultiplexer and then retimed. The use of a common pulse-shaping system significantly decreases the relative jitter between output waveforms, resulting in a significant cost reduction. The OMEGA Laser System now uses a single high-bandwidth AWG and a TMPS system to generate three high-resolution shaped pulses that can be propagated in different amplification systems.[14] The OMEGA EP Laser System will significantly benefit from the implementing a similar pulse-shaping system; in particular, higher-resolution waveforms with lower relative jitter will be generated to seed the four beamlines. A tentative layout for a redesigned fiber front end supporting direct drive on the NIF includes six eight-channel TMPS systems to generate 48 high-resolution shaped waveforms. The following sections describe the principle and implementation of the TMPS system and present experimental results focusing on the performance of the demultiplexer.

Principle and Implementation

1. General System Description

The purpose of time-multiplexed pulse shaping is to generate a plurality of shaped optical waveforms on physically distinct optical paths; for example, optical fibers, using a single high-performance pulse-shaping system [Fig. 146.12(a)]. The pulse-shaping unit generates a composite optical waveform composed of the shaped waveforms in their respective time slots. The composite waveform is sent to an optical demultiplexer configured to route different temporal slices to different outputs. In this work, the demultiplexer is configured to maximize the transmission of time slot j from demultiplexer input to output j while minimizing the transmission of other time slots to the same output. Optical fibers after each demultiplexer output relatively delay the demultiplexed waveforms; for example, when synchronized waveforms must propagate in different sections of a laser system and arrive on target with a predefined relative timing.

TMPS allows for significant performance improvement and cost reduction compared to the implementation of multiple pulse-shaping systems. The relative jitter between the generated waveforms is limited only by the short-term variations of the pulse-shaping system's time base, without any impact from the jitter between the pulse-shaping system and an external trigger. Lowering the relative jitter between waveforms is an important

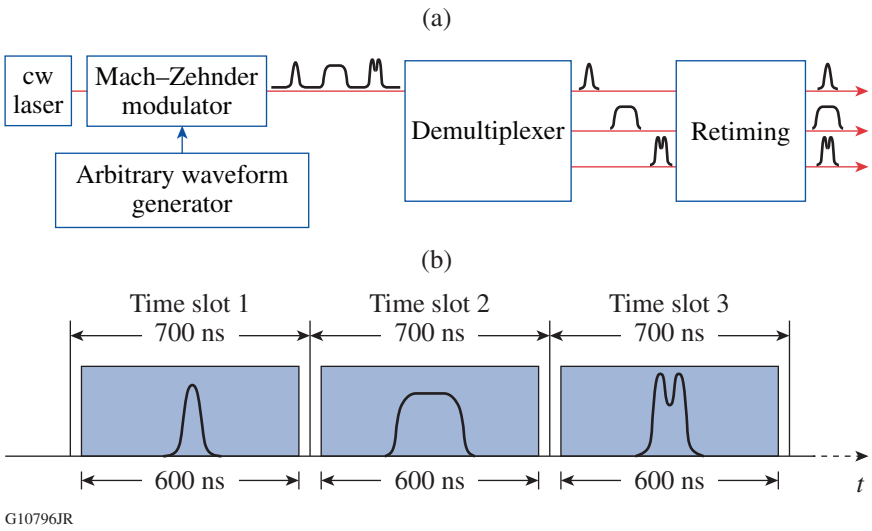

Figure 146.12
(a) Schematic of a time-multiplexed pulse-shaping (TMPS) system. Shaped optical waveforms are generated by modulating a continuous-wave (cw) laser using a Mach–Zehnder modulator driven by an arbitrary waveform generator, demultiplexed, and retimed relative to one another. (b) Timing diagram for the shaped waveforms in the composite waveform generated by the pulse-shaping unit.

consideration when the shaped pulses must be recombined into a single optical waveform later in the system or arrive on target with well-controlled relative timing. Generating multiple shaped optical waveforms with a single pulse-shaping unit instead of several units can significantly reduce the overall cost.

2. Typical Parameters

The required TMPS performance is application dependent. The application we focus on is the seeding of multiple high-energy laser systems. For the seed of each laser system, we allocate a time slot in which the seed pulse can be arbitrarily timed [Fig. 146.12(b)]. This ensures sufficient flexibility to modify the relative timing between seed pulses without reconfiguration or recalibration. In this work, consecutive 700-ns time slots are used because of an operation requirement for OMEGA,[14] where sub-10-ns seed pulses must be temporally tunable by as much as ±300 ns relative to their average timing. The 700-ns slots allow one to tune the seed pulses in a 600-ns range while leaving a 100-ns buffer window for transitioning the demultiplexer between different demultiplexing states.

For an N-channel system (N outputs, N time slots), the demultiplexer performance can be described by the $N \times N$ transmission matrix (T_{ij}), where T_{ij} is the transmission of time slot j from input to output i. Ideally, the diagonal elements are equal to 1 (no loss) and nondiagonal elements are equal to 0 (infinite extinction ratio). In practical conditions (i.e., with insertion losses, demultiplexer and driver imperfections), optimal demultiplexer operation corresponds to maximizing the diagonal elements while minimizing the nondiagonal elements.

3. Demultiplexer Technology

A custom lithium niobate ($LiNbO_3$) waveguide structure composed of fifteen 1×2 $\Delta\beta$ phase-reversal switches[15,16] has been procured from EOSPACE[17] to demonstrate an eight-channel TMPS (Fig. 146.13). In the absence of propagation

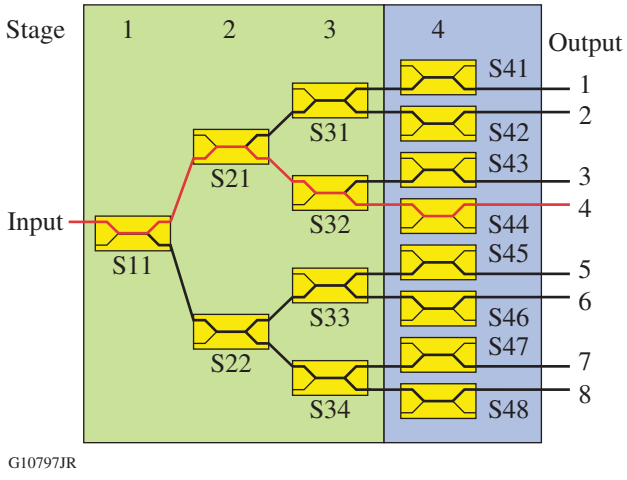

Figure 146.13
Layout of the 1×8 demultiplexer with three demultiplexing stages and one extinction-enhancement stage. Possible optical paths are traced with thick lines. The routing from input to output 4 is traced in red.

losses, the coupling ratio between two adjacent waveguides of length L is described by

$$T_{12} = T_{21} = \frac{1}{1+\left(\Delta\beta L_c/\pi\right)^2} \sin^2\left[\frac{\pi L}{2L_c}\sqrt{1+\left(\Delta\beta L/\pi\right)^2}\right], \quad (1)$$

where $\Delta\beta$ is the difference in propagation constant and L_c is the coupling length. The difference $\Delta\beta$ is controlled by applying a voltage that modifies the local refractive index via the electro-optic effect. Figure 146.14 shows an example of the measured transmission characteristics versus applied voltage for a 1053-nm monochromatic source propagating in a packaged $LiNbO_3$ 1×2 $\Delta\beta$ phase-reversal switch. Two voltages corresponding to the bar (no coupling between waveguides, i.e., $T_{12} = 0$) configuration and cross (all light from each waveguide is coupled to the other waveguide, i.e., $T_{12} \sim 1$) configurations of each 1×2 switch must be identified for optimal routing.

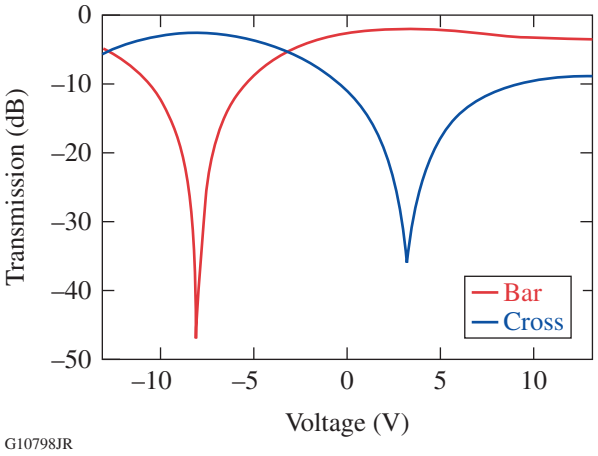

Figure 146.14
Measured transmission from the input to the cross and bar outputs versus voltage for a 1×2 $\Delta\beta$ phase-reversal switch.

The 1×8 demultiplexer designed and fabricated by EOSPACE[17] is organized in four stages (Fig. 146.13):

- Each 1×2 switch in the first three stages (switches S11, S21, S22, S31, S32, S33, and S34) can route its input to either of its outputs for demultiplexing.
- Each switch in the fourth stage (S41 to S48) can route its input to either an output connected to an optical fiber or an unconnected output to enhance the demultiplexer extinction ratio.

4. Driver Technology

To operate the demultiplexer, one must apply control voltages to each of the fifteen 1×2 switches. The most-general driver implementation consists of 15 AWG's that provide a time-dependent voltage to each switch, but this solution is complex, expensive, and cumbersome to integrate. Because demultiplexing requires operating each 1×2 switch in either the bar or cross configuration, a custom driver that produces two independent voltages and switches between them has been designed (Fig. 146.15). The bar and cross voltages are generated by two 12-bit digital-to-analog converters (DAC's) with output voltage between 0 and 5 V, followed by a fast analog switch. An operational amplifier level-shifts and amplifies the analog-switch output to the [–13-V, +13-V] range. A field-programmable gate array (FPGA) drives the fast analog switches. The FPGA uses a 200-MHz clock to specify the state of each analog switch in any 5-ns time window.

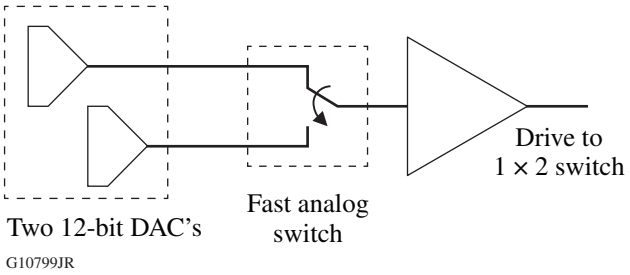

Figure 146.15
Elementary block diagram of the driver for each of the fifteen 1×2 switches in the 1×8 demultiplexer. The field-programmable gate array (FPGA) drives the fast analog switch to produce the voltage value generated by either of the 12-bit digital-to-analog converters (DAC's) and drive the 1×2 switch after amplification.

The state of the 15 analog switches, i.e., the state of each 1×2 switch in the demultiplexer, is defined in a routing table for each output. For example, routing from input to output 4 requires that switch S11 be in the bar configuration, switch S21 in the bar configuration, switch S32 in the cross configuration, and switch S44 in the bar configuration (red path in Fig. 146.13). All other fourth-stage switches are set to the cross configuration to route unwanted light to their unconnected output and enhance the extinction. The FPGA allows for arbitrary demultiplexing patterns, but the switch is sequentially driven for our application, i.e., time slot j is sent to output port j for a given number of cycles of the 200-MHz clock. When externally triggered, the FPGA runs through the defined sequence and waits until the next trigger. The driver and demultiplexer have been successfully operated at trigger rates up to 1 MHz. All results presented here have been obtained at much lower rates (1 kHz

and lower), which are more representative of the operating repetition rates of fiber front ends for high-energy laser systems (300 Hz at LLE and 960 Hz on the NIF).

Experimental Results

1. General Information

The experimental results focus on the performance of the 1×8 demultiplexer supporting the TMPS system at 1053 nm. A trigger and 76-MHz reference signals were provided to the FPGA by a digital-delay generator (Stanford Research DG645) and a waveform generator (Agilent 33250A), respectively. The eight demultiplexer output fibers were connected to fiber-coupled DSC30 photodiodes (Discovery Semiconductors) connected to the two sets of four measurement channels of two 12-GHz oscilloscopes (Agilent). The oscilloscopes record the temporally resolved transmission of the demultiplexer between its input and each of its eight outputs.

In static operation, the voltages applied to the fifteen 1×2 switches are constant and the time-independent transmission between the demultiplexer and its eight outputs is characterized by an 8×8 matrix T_{ij}. This matrix has diagonal elements T_{ii} and nondiagonal elements T_{ij} corresponding to the transmission to output i when the demultiplexer is set to route the input light to output i and to other outputs j, respectively. In dynamic operation, the drives applied to the fifteen 1×2 switches change between their two binary voltage values set by the respective DAC's following a pattern determined by the FPGA. The FPGA keeps the drive voltages constant over time slots of specified duration. When 700-ns time slots are used, the transmission between input and each of the eight outputs is averaged over 600-ns intervals at the center of the eight time slots to quantify the demultiplexing performance because no significant transmission variation was observed in these intervals. This allows one to characterize the demultiplexer performance with an 8×8 matrix for specific dynamic conditions (demultiplexing sequence and time-slot duration). Because of details of the experimental implementation, each line of the transmission matrix in dynamic conditions is scaled to the transmission observed for the diagonal element; therefore, the extinction ratios are defined relative to the outputs.

2. Eight-Channel Static Operation

The demultiplexer is first calibrated with static voltages applied to all fifteen 1×2 switches. The static voltage applied to a specific switch is varied and the transmission between the input and one particular output is measured. The path between input and the chosen output must contain the switch being calibrated (e.g., one can choose output 4 to calibrate switches S11, S21, S32, and S44). This yields 15 transmission curves similar to one of the curves plotted in Fig. 146.14. Each of these curves is fitted with a second-order polynomial around its respective minimum and maximum to identify the optimal operation voltages. This calibration leads to the 30 optimal DAC voltages for static routing between input and outputs by the 15 switches.

The static transmission properties of the calibrated demultiplexer were characterized using a high-dynamic-range power meter. With the power meter connected to output i, the driver was sequentially configured to send light to each output j, therefore leading to a measurement of the transmission T_{ij} after normalization by the input power. The measured transmission matrix T_{ij} (Fig. 146.16) has diagonal elements, i.e., insertion losses, ranging from –4.6 to –5 dB and nondiagonal elements ranging from –55 dB to –70 dB, the latter being the measurement detection limit.

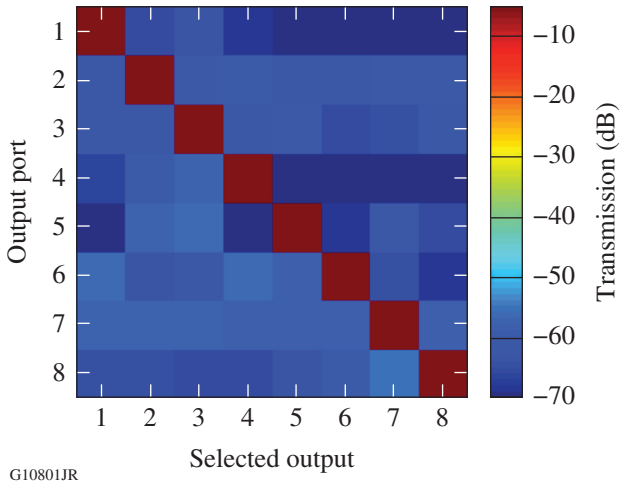

Figure 146.16
Transmission matrix on a logarithmic scale for eight-channel static operation. The transmission is measured at the eight output ports (vertical axis) when the multiplexer is driven to route light to each of the eight ports (horizontal axis).

3. Eight-Channel Dynamic Operation

When the voltage driving a 1×2 switch quickly changes between two different values, e.g., the values corresponding to the bar and cross configurations, the time-resolved switch transmission has a fast component and a slow component. The fast component measured on our system is of the order of 5 ns, including the response time of the custom driver. The slow component is, in comparison, extremely slow (hundreds of microseconds). The existence of these two components implies that drive voltages optimized for static routing are not optimal for dynamic demultiplexing. Non-optimal voltages

increase the insertion losses and decrease the extinction ratios. Drive voltages must be calibrated in dynamic operation, i.e., when driving the demultiplexer to route different time slots (with ~μs duration) of the input signal to different outputs. A general formalism has been developed to ensure that the calibration process is computationally efficient and exhaustive. For a particular switch, the temporally resolved demultiplexer outputs are measured and processed to identify the two drive voltages that optimize the switch transmission in dynamic operation. Optimization consists in maximizing transmission for combinations of time slots and output ports where it must be high and minimizing transmission for combinations of time slots and output ports where it must be low.

The demultiplexer was optimized for dynamic operation with eight output channels. The optimal voltages for dynamic operation were found to be significantly different from the optimal static voltages. The 8×8 transmission matrix with these voltages is shown in Fig. 146.17(a). The lowest observed extinction is –46 dB, and all but five out of the 56 nondiagonal elements of the extinction matrix are lower than –50 dB. For comparison, the eight-channel TMPS system has been characterized when using the drive voltages optimized for static routing [Fig. 146.17(b)]. The observed performance degradation confirms that adequate operation in dynamic operation can be obtained only by calibration in dynamic conditions. The transmission properties of the demultiplexer driven with the optimized static voltages are clearly seen in the resulting time-resolved signals measured on the eight output ports (Fig. 146.18).

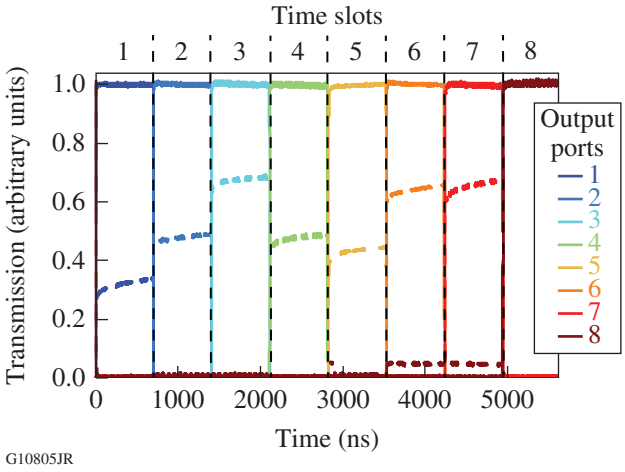

Figure 146.18
Time-resolved transmission measured on the eight output ports in dynamic operation. The continuous and dashed lines correspond to the transmission measured with voltages optimized in dynamic operation and static operation, respectively.

Conclusions

A system architecture to efficiently extend the performance of a single pulse-shaping unit by high-performance demultiplexing has been described. The time-multiplexed pulse-shaping concept generates multiple waveforms in different time slots that are demultiplexed and retimed relative to one another. An experimental implementation of the demultiplexing subsystem based on a 1×8 $LiNbO_3$ demultiplexer based on four stages of 1×2 $\Delta\beta$ phase-reversal switches has been described

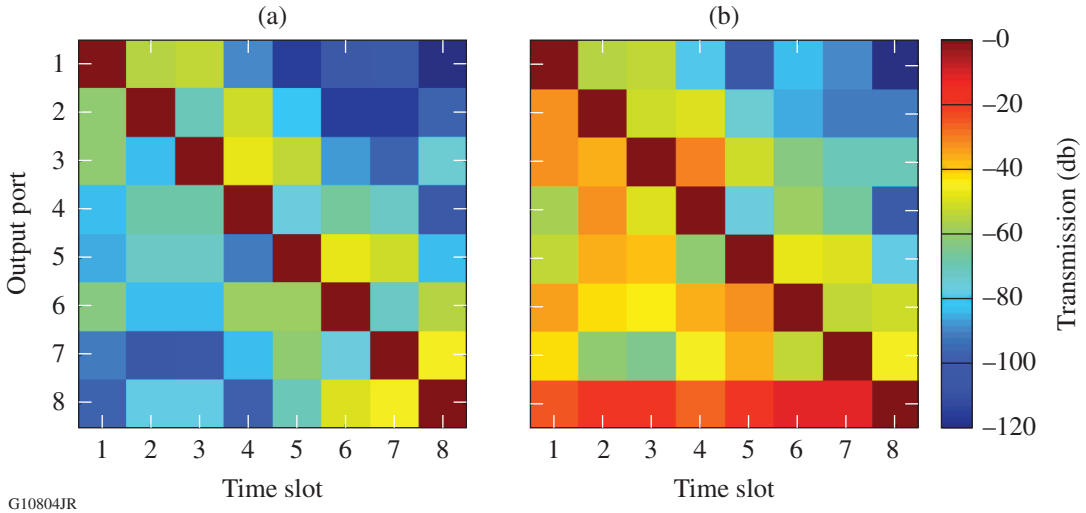

Figure 146.17
Transmission matrix on a logarithmic scale for eight-channel dynamic operation with voltages optimized for (a) dynamic operation and (b) static operation.

and characterized. High-performance demultiplexing has been demonstrated for an eight-channel system (50-dB extinction ratio) by determining optimal values of the drive voltages for each 1×2 switch for dynamic routing.

The demultiplexer was optimized for four-channel operation to support its deployment on OMEGA and OMEGA EP. When demultiplexing of the input waveform to only four output ports is required, the third-stage switches can be used to enhance the extinction ratio of the demultiplexed waveforms. This has led to a measured contrast of the order of 70 dB in dynamic conditions. Operation of the demultiplexer on signals generated at 1064 nm with drive voltages optimized for operation at 1053 nm has led to no significant performance degradation, indicating that the demultiplexer can operate with tunable signals and signals with an optical spectrum broadened by phase modulation.

ACKNOWLEDGMENT

The authors thank G. Kick, R. Hopf, and D. Hassett (Laboratory for Laser Energetics) for their work on the switch driver, and G. Abbas and S. Thaniyavarn (EOSPACE) for fruitful discussion about the demultiplexer. This material is based upon work supported by the Department of Energy National Nuclear Security Administration under Award Number DE-NA0001944, the University of Rochester, and the New York State Energy Research and Development Authority. The support of DOE does not constitute an endorsement by DOE of the views expressed in this article.

REFERENCES

1. A. M. Weiner, Rev. Sci. Instrum. **71**, 1929 (2000).
2. T. Yilmaz *et al*., IEEE Photonics Technol. Lett. **14**, 1608 (2002).
3. P. K. Kondratko *et al*., IEEE Photonics Technol. Lett. **17**, 2727 (2005).
4. A. Monsterleet *et al*., Electron. Lett. **41**, 332 (2005).
5. J. Yao, F. Zeng, and Q. Wang, J. Lightwave Technol. **25**, 3219 (2007).
6. Z. Jiang *et al*., IEEE J. Quantum Electron. **43**, 1163 (2007).
7. Y. Dai and J. Yao, J. Lightwave Technol. **26**, 3329 (2008).
8. M. Bolea *et al*., IEEE Photonics Technol. Lett. **23**, 618 (2011).
9. Arbitrary Waveform Generation Model No. AWG70001A, Tektronix, Inc., Beaverton, OR 97077, http:/www.tek.com (24 May 2016).
10. Keysight Technologies, Inc., Santa Rosa, CA 95403-1738, http://www.keysight.com/main/home.jspx?cc=US&lc=eng (21 April 2016).
11. P. J. Wisoff *et al*., Proc. SPIE **5341**, 146 (2004).
12. C. A. Haynam *et al*., Appl. Opt. **46**, 3276 (2007).
13. J.-F. Gleyze *et al*., Proc. SPIE **7916**, 79160I (2011).
14. T. Z. Kosc, J. H. Kelly, E. M. Hill, C. Dorrer, L. J. Waxer, and W. R. Donaldson, Proc. SPIE **9345**, 93450H (2015).
15. H. Kogelnik and R. Schmidt, IEEE J. Quantum Electron. **12**, 396 (1976).
16. S. Thaniyavarn, Proc. SPIE **578**, 192 (1985).
17. EOSPACE, Inc., Redmond, WA 98052, http://www.eospace.com (17 May 2016).

Continuous Distributed Phase-Plate Advances for High-Energy Laser Systems

Introduction

The symmetric-direct-drive (SDD) and polar-direct-drive (PDD) configurations utilized in inertial confinement fusion[1,2] (ICF) driven by high-power lasers require target illumination that conforms to the design shape or objective with a high degree of fidelity. Nonuniformity in the lower spherical-harmonic ℓ modes can have a significant impact on ICF target performance since these modes imprint for the longest period of time and are the most difficult to smooth.

Continuous phase plates are used in SDD and PDD ICF applications because they offer control of the far-field intensity envelope in the presence of typical laser system phase aberrations. The resultant time-averaged, far-field spot intensity has a well-controlled shape. The goal is to design phase-dislocation–free continuous phase plates that produce a speckled far field whose envelope and spectrum are controlled, unaffected by system aberrations and speckle that can be smoothed.

This article describes a novel distributed phase plate (DPP) design process that achieves higher fidelity to the design objectives relative to existing methods. The novel DPP design code is called *Zhizhoo*' and is capable of producing a continuous phase-dislocation–free DPP with low near-field modulation that achieves a <1% to 2% weighted σ_{rms} error of the far-field spot shape in a few minutes using a multicored personal computer with optional GPU accelerations.

The versatility of the *Zhizhoo*' design technique is evident in its ability to craft far-field envelopes from simple super-Gaussian to rather arbitrary shapes.[3] The phase-plate design techniques presented here can be applied to phase plates with or without constraining the far-field power spectrum to lower spectral power in the long-wavelength band. The ability of this technique to calculate phase-dislocation–free continuous phase plates is closely linked to maintaining a correlation with the speckle pattern and minimizing the phase gradient.[3] Various phase-plate designs will be presented for a few high-power laser systems that highlight the various capabilities of *Zhizhoo*'.

Zhizhoo' DPP Design Tool

The *MATLAB*-based tool *Zhizhoo*'[3,4] crafts continuous DPP's; the salient features of *Zhizhoo*' are as follows:

(a) Employs a feedback loop: Unlike other methods currently in use, *Zhizhoo*' employs a novel feedback technique as a fundamental tool to generate DPP profiles with tight control of the resultant far-field spot shape and phase plate; e.g., far-field shape, arbitrary azimuthal and radial variations, DPP phase gradient, DPP phase spectral control, and phase anomaly-free designs.[3] The algorithm employs a highly modified Fienup-type algorithm as part of the whole feedback loop.[5,6] The overall technique is novel in its approach and is very fast because of the feedback (which distinguishes *Zhizhoo*' as it hastens convergence via augmentation) and the *FFTW*-based methods.[7] In addition, a robust phase-unwrapping algorithm is employed that solves Poisson's equation in the least squares sense (algorithm adapted from Ref. 8).

(b) Designs far-field envelopes from simple super-Gaussian to rather arbitrary shapes: Simple or exotic far-field envelope shapes are effortlessly handled with *Zhizhoo*'. Wide design objectives and/or steep profiles will require correspondingly higher surface or phase gradients in the DPP. *Zhizhoo*' can maintain envelope control, even down to the ~1% σ_{rms} level.

(c) Uses an optimal filter: An important aspect of the *Zhizhoo*' feedback loop is the Wiener or optimal filter.[3] The Wiener filter employs the well-known speckle statistics from Goodman[9,10] to model the speckle "noise" to create an optimal filter that accurately extracts the true envelope shape.

Zhizhoo' Intermediate NIF Polar-Direct-Drive Distributed Phase Plate Designs

The National Ignition Facility's (NIF's) PDD asymmetric far-field spot design objective is an ideal candidate to test the shape control capabilities of *Zhizhoo*'. The NIF PDD asymmetric spot shape is a composite spot consisting of a primary super-Gaussian plus an offset secondary ellipse that

is modulated by an offset aperturing function referred to as "spot-masking apodization" (SMA). The asymmetric far-field spot objective for NIF PDD cannot be considered an ellipse nor can it be accurately represented as a distorted ellipse. The 43×43-cm-sq–aperture intermediate NIF PDD design for one of the equatorial spots is shown in Fig. 146.19(a) along with the resultant speckled spot in Fig. 146.19(b). The effect of SMA is clearly observed in Fig. 146.19(b), where the over-the-horizon portion of the spot is occluded.

It is crucial to the success of NIF PDD experiments that the DPP design prepared for the manufacturing process be as close as possible to the design objective. Otherwise, the far-field spot's integrity severely degrades in the presence of both manufacturing phase error (MPE) and near-field wavefront error (WFE). A DPP design that initially has the highest integrity level will remain more intact, relative to an insufficient design. NIF's WFE was measured and imposed upon the DPP's for a worst-case analysis via *DRACO* hydrodynamic simulations. The strongest NIF beamline WFE was a weaker aberration than a 25-μm-rms (root-mean-square) MPE, setting the acceptable MPE tolerance to 25-μm rms.

During the NIF's PDD (intermediate and ignition-scale) DPP design process, a potential manufacturing problem surfaced. The issue was the result of a combination of interferometric measurements and the machine's internal phase-unwrapping algorithms. The resulting unwrapped phase would produce areas of phase dropouts and occasionally large regions of π discontinuities. However, the phase-unwrapping procedure incorporated within *Zhizhoo*' is designed to be immune to areas of noise and regions of π discontinuities. It was demonstrated that the phase-unwrapping algorithm was more than capable of removing and correcting the corrupted phase data from the instrument.[11] Utilizing the phase-unwrapping algorithm from *Zhizhoo*' is a cost-effective alternative to procuring expensive interferometers. The algorithm is able to correct the phase errors from the intermediate energy scale up to the ignition-scale designs.

Steep-Profile, Low-Ripple, Flattoped Round Spots

Low-ripple, flattopped spots with steep profiles are additional design objectives compatible with the *Zhizhoo*' DPP design method. Traditionally, DPP's have had difficulty designing low-ripple, flattopped spots because the designs tended to ring as the spot shape rolls off to zero. In contrast, *Zhizhoo*'-crafted DPP's tend not to suffer the same fate because of the feedback control with augmentation of the design profile.

The OMEGA EP laser required a redesign for its 1.8-mm-wide spot because of damage that the turning mirror suffered from high-level modulation caused by a retroreflection back through the focusing lens. The close proximity of the turning mirror posed a design challenge for *Zhizhoo*' by mandating wavelength control of the DPP's feature size. The design for the far-field envelope demanded a large flat area with a fast roll-off.

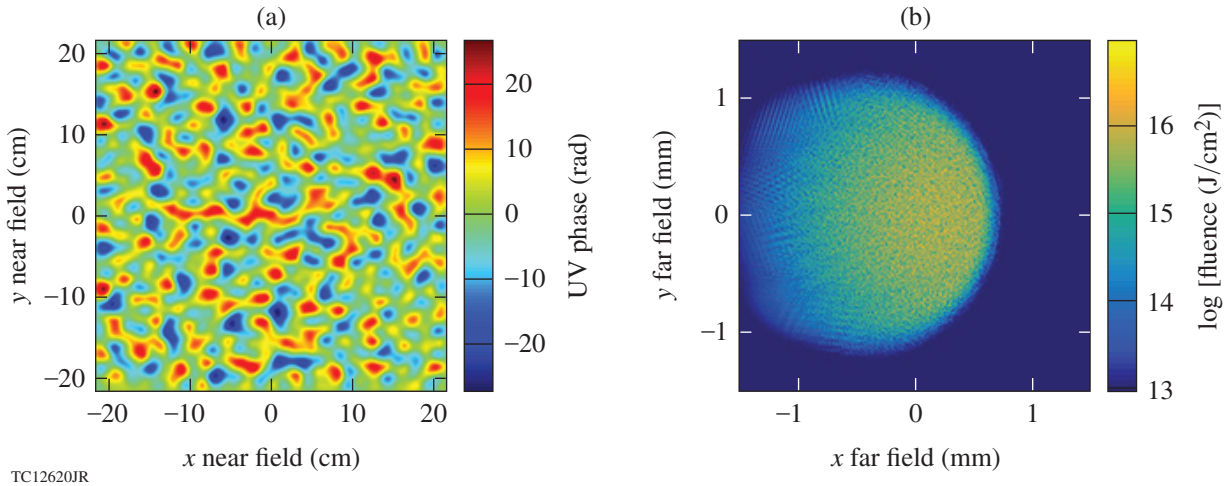

Figure 146.19
The intermediate NIF polar-direct-drive (PDD) distributed phase plate (DPP) design crafted for (a) an equatorial beam profile and (b) the resultant speckled spot. The speckled image on the log scale demonstrates the remarkable speckle rejection and smooth profile at low intensity not obtainable using other methods. Note that the design objective function and the extracted envelope are nearly indistinguishable at a <1% rms (root-mean-square) error.

The low-ripple (2.5%) resultant extracted envelope is shown in Fig. 146.20(a). The equivalent free-space back-propagation was determined to be 6 m, which drove the DPP design to use large feature sizes to minimize near-field modulations [see Fig. 146.20(b)]. The larger feature sizes had the side effect of driving up the peak-to-peak phase depth of the DPP because of the smaller bandwidth distribution of the phase, which also increased local phase gradients.

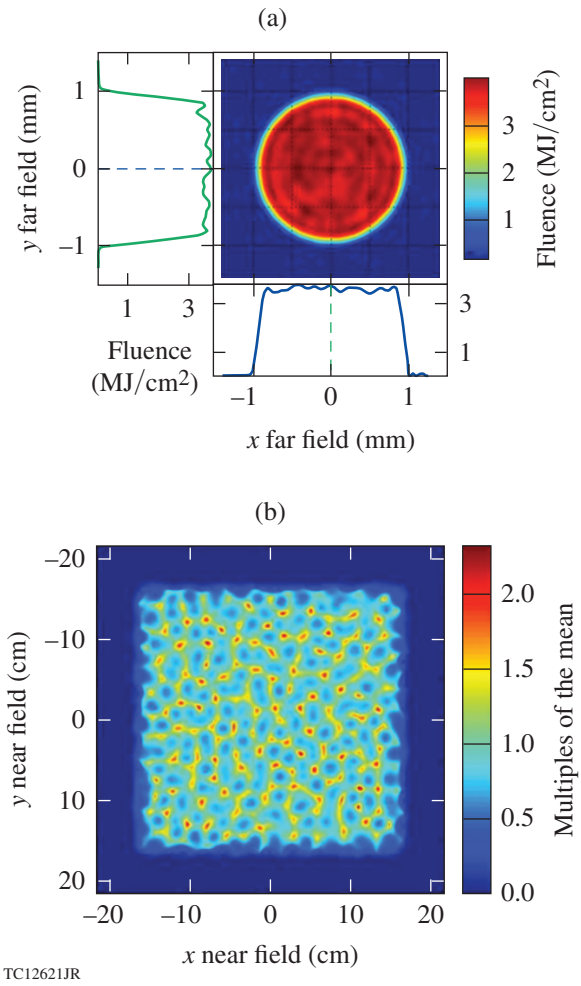

Figure 146.20
(a) The OMEGA EP low-ripple, 1.8-mm-wide far-field extracted envelope. (b) The resulting near-field low-level modulation from a retroreflection is indicative of the large DPP feature sizes.

The Dynamic Compression Sector (DCS) laser also required a low-ripple, flattopped spot but with two additional attributes: decreased mid-range spectrum (high pass) and a flexible spot shape via dispersion control. The high-pass DPP design procedure, similar to the method reported in Ref. 3, successfully reduced the power in the long- to mid-wavelength modes, even in the presence of predicted DCS WFE (see Fig. 146.21). The DCS DPP design provides a trade-off among several smoothing attributes, including spot shape and intensity on target, by adjusting a differential grating that changes the dispersion experienced by the 1-D, multi-FM smoothing by spectral dispersion system.[12]

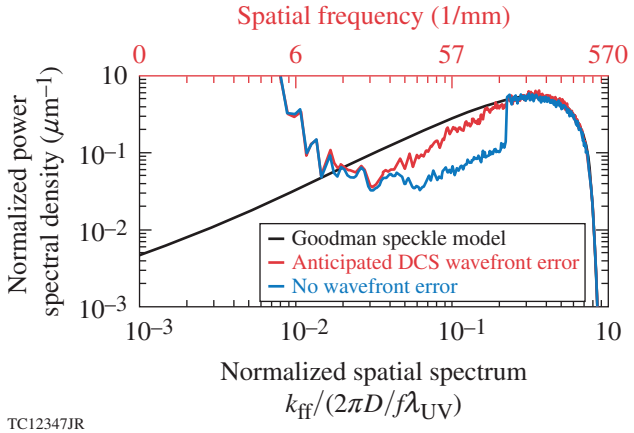

Figure 146.21
The far-field speckled spot spectrum for the DCS Laser System. The Goodman speckle model is shown as a reference to indicate the ability of the high-pass DPP design to modify the far-field spot's spectrum (blue curve). In the presence of predicted DCS laser WFE, the high-pass DPP design still maintains a decreased spectrum over the spectral band (red curve). DCS: Dynamic Compression Sector; WFE: wavefront error.

Conclusion

The continuous phase-plate design code *Zhizhoo*' is capable of crafting DPP's for a variety of high-power laser systems, each having different design constraints. *Zhizhoo*' designs continuous DPP's with simple envelope shapes or exotic shapes with asymmetry. The code *Zhizhoo*' crafts DPP's with a high degree of fidelity to the design objective. A higher-fidelity DPP design results in a more-faithful representation of the desired objective function when the DPP is subjected to WFE and MPE. The flexibility of the *Zhizhoo*' design code makes it easy to create multiple designs, even when the design requirements change because *Zhizhoo*' can respond in a short period of time or produce multiple realizations to improve beam-overlap nonuniformity reduction.

ACKNOWLEDGMENT

This material is based upon work supported by the Department of Energy National Nuclear Security Administration under Award Number DE-NA0001944, the University of Rochester, and the New York State Energy Research and Development Authority. The support of DOE does not constitute an endorsement by DOE of the views expressed in this article.

REFERENCES

1. C. P. Verdon, Bull. Am. Phys. Soc. **38**, 2010 (1993).
2. S. E. Bodner, D. G. Colombant, J. H. Gardner, R. H. Lehmberg, S. P. Obenschain, L. Phillips, A. J. Schmitt, J. D. Sethian, R. L. McCrory, W. Seka, C. P. Verdon, J. P. Knauer, B. B. Afeyan, and H. T. Powell, Phys. Plasmas **5**, 1901 (1998).
3. J. A. Marozas, J. Opt. Soc. Am. A **24**, 74 (2007).
4. Inspired by Anishinaabe words *Zhizhoo'*, meaning "spreads someone using something," and *zhizhoo'an*, meaning "spreads something using something," just as the phase plate spreads out the diffraction-limited, far-field spot to match the far-field objective. J. D. Nichols and E. Nyholm, *A Concise Dictionary of Minnesota Ojibwe* (University of Minnesota Press, Minneapolis, 1995).
5. R. W. Gerchberg and W. O. Saxton, Optik **35**, 237 (1972).
6. J. R. Fienup, Appl. Opt. **21**, 2758 (1982).
7. M. Frigo and S. G. Johnson, Proc. IEEE **93**, 216 (2005).
8. D. C. Ghiglia and L. A. Romero, J. Opt. Soc. Am. A **11**, 107 (1994).
9. J. W. Goodman, *Introduction to Fourier Optics* (McGraw-Hill, New York, 1988).
10. J. W. Goodman, in *Laser Speckle and Related Phenomena*, edited by J. C. Dainty, Topics in Applied Physics (Springer-Verlag, Berlin, 1984), Vol. 9, Chap. 2, pp. 9–75.
11. LLNL kindly fabricated *Zhizhoo'*-crafted DPP prototypes and measured them using their interferometers, which provided the data for this analysis.
12. J. A. Marozas, J. D. Zuegel, and T. J. B. Collins, Bull. Am. Phys. Soc. **52**, 145 (2007); *ibid*. **53**, 249 (2008); *ibid*. **54**, 306 (2009); *ibid*. **55**, 294 (2010).

Nanomechanics and Laser-Induced Damage in Optical Multilayer Dielectric Gratings

Introduction

Multilayer dielectric (MLD) pulse-compressor gratings are critical components used in a high-peak-power laser system's amplification system and have been a focus of recent research and development efforts because of their low damage thresholds.[1,2] At LLE, the peak-power capability—and, therefore, the overall performance of the petawatt-class OMEGA EP Laser System—is limited by the laser-damage resistance of diffraction gratings in the chirped-pulse–amplification (CPA) pulse compressors for each beamline.[3–6] Increasing the damage thresholds of these components is, therefore, an important objective.

A low-temperature chemical cleaning approach developed by Howard *et al.*[7] to improve the performance of these MLD gratings has demonstrated that grating coupons that were cleaned using the optimized method consistently met OMEGA EP requirements on diffraction efficiency (>97%) and 1053-nm laser-damage resistance at 10 ps (>2.7 J/cm^2). They also observed that, for samples with the highest damage threshold, there were minimal laser-conditioning effects, suggesting a transition from a contamination-driven laser-damage mechanism to defect-driven damage for well-cleaned components. Hereafter, this metric—laser-induced–damage threshold (LIDT)—will be referred to as optical testing. Such optical testing is the most common way to characterize the performance and, therefore, the quality of an MLD grating that has been cleaned for use in a high-power laser system.

There is some concern that cleaning procedures and/or fabrication techniques for gratings can mechanically weaken the fragile grating pillars, possibly affecting the grating's resistance to laser damage and, therefore, warrant mechanical characterization. The development of a methodology to monitor a grating's mechanical properties will enable one to better understand the fabrication and cleaning processes and will point to appropriate modifications that will preserve or enhance the grating's integrity.

Nano-indentation of MLD gratings[8] is our adopted approach, and the indents that invoke fracture of the silica walls are treated in detail. Nano-indentation and/or uniaxial compression of patterned surfaces manufactured by techniques such as focused ion-beam (FIB) milling and lithography[9] have shown tremendous potential in isolating the ductile response of the material from its brittle response. These studies prominently feature the uniaxial compression of metallic high-aspect-ratio micro- and nanopillars,[10–13] produced by FIB milling, with diameters ranging from 75 nm to 7.5 μm. Such structures are used to study the ductile deformation of metals, specifically size effects and their dependence on properties such as yield strength.

Experiments on micropillars of amorphous silica subjected to uniaxial compression have recently been reported by Lacroix *et al.*[14,15] Their findings indicate that silicate glasses are very suitable for micropillar compression because the ratio of the yield stress to Young's modulus is comparatively high compared to a typical metal. They also demonstrated the experimental conditions under which plastic flow can be obtained in compression of these pillars without catastrophic failure and accompanied only by minor, well-defined radial crack patterns.

The LIDT of amorphous silica gratings for ultrahigh intensity laser systems has been studied extensively in literature.[16,17] The electric field is known to be maximum at the top area of the grating walls. It is in this region of local enhancement that damage initiates, defining the ultimate damage threshold.

Both tests (laser-induced damage and nano-indentation), although vastly different in nature and implementation, inherently measure the performance of the grating (optical versus mechanical). Fracture, caused by a concentration of mechanical stresses, is an integral part of these measurements. Therefore, it is imperative and almost intuitive to explore mechanical testing (nano-indentation) as a means to complement and even precede optical testing to establish the "quality" and performance of an MLD grating sample. We are guided by the observation that both optical fields (electric and magnetic) and mechanical fields (stress and strain), when interacting with the grating

geometrical features and with defects and inhomogeneities, will show significant concentrations.

Materials and Methods

1. Fabrication of MLD Gratings

The process of manufacturing MLD gratings has been detailed extensively in published literature[7,8,18] and is summarized here for completeness.

The first step is to deposit the MLD coating on the glass substrate (fused silica or BK7) by reactive evaporation at 200°C as a thick, modified-quarter-wave thin-film stack[19] with hafnia (HfO_2) and silica (SiO_2) used as the high- and low-index materials, respectively. Next, a bottom antireflective coating (BARC) layer (organic polymer) may be applied to the multilayer mirror, followed by a layer of photoresist coating. Interference lithography is used to pattern the grating (grooves, 1740 lines per mm). Once patterned, etching is performed to remove the BARC and a portion of the top MLD layer, leaving the silica wall geometry.

Finally, organic (BARC, photoresist layers, etch products, and environmental contamination) and inorganic residues (metallic contaminants) are stripped away in a final cleaning process. For the grating samples used in this work, the silica walls were ~440 nm high with a slightly tapered geometry (~250 nm wide at the base and ~150 nm wide at the top).[8]

2. An Optimized Procedure for Cleaning MLD Gratings to Maximize Laser-Damage Thresholds

For this study, cleaning experiments were performed on small-scale MLD grating coupons. Round hafnia/silica MLD gratings (100 mm in diameter, 3 mm thick) were broken into eight equally sized, wedge-shaped coupons. All cleaning experiments described in this section were performed on uncleaned gratings with BARC and photoresist still intact (that is, they were not subjected to any photoresist stripping or cleaning operations other than those described here). Uncleaned gratings can be easily distinguished by their characteristic brown and hazy appearance (which disappears when a grating is well cleaned), attributed to the residual organic materials.

Acid piranha, the most widely used chemical cleaning agent at higher temperatures,[18] was insufficient for our low-temperature (40°C) process; a multistep technique is warranted to ensure a wide-range removal of performance-limiting contaminants. This cleaning methodology—discussed in Howard's work[2,7,8,18–20] and adapted by improvising on existing literature for cleaning gratings (such as Refs. 18 and 21) and semiconductor wafer processing—was split into two parts: a partial clean consisting of six steps and a final clean that included a plasma step. The cleaning process is summarized in Table 146.II.

The final clean, which is a third plasma treatment, can be either an air plasma[7] or an oxygen plasma (conventionally used

Table 146.II: Cleaning process for the MLD gratings used in this work.

Cleaning Process				Process Steps	
	Step	Temperature (°C)	Time (min)	Chemical	Purpose
Partial clean	1	40	15	5:1 piranha spray	Strip photoresist and etch residues
	2	40	15	2:1 piranha spray	Strip photoresist and etch residues
	3	23	10	Air plasma (6.8-W power)	Completely remove BARC
	4	40	10	1:1:6 SC-2 no-stir soak	Remove metallic contamination
	5	23	10	Air plasma (6.8-W power)	Remove light organic matter
	6	23	5	2800:1 BOE* soak	Reduce grating duty cycle
Final step	7	23	15	Air plasma (6.8-W power) OR Oxygen plasma (6.8-W power)	Remove organics from grating surface

*buffer oxide etch

in grating cleaning procedures). As shown later, this choice can have a decisive effect on the laser-damage threshold attained by a grating sample.

3. Laser-Damage Testing

Damage testing was carried out at LLE's damage-testing facility on the short-pulse (10-ps) system with operating capabilities in both air and high vacuum (4×10^{-7} Torr). The MLD grating samples studied here were tested in air using *s*-polarized light at 1053 nm at an incident beam angle of 61° with an irradiation spot size of 370 μm (e^{-1} in intensity) in the far field. Beam analysis and fluence calculations were performed using the Ophir–Spiricon commercial laser-beam profiler. Laser damage was assessed *in situ* using a white-light imaging system (~100× magnification). Damage was defined as a feature on the sample's surface that was not observed before laser irradiation.[20,22] Damage thresholds are reported as beam-normal fluences. An example of a damage site on grating 566-5 is shown in Fig. 146.22.

Our damage tests employed the *N*-on-1 testing regime performed in air. Particulars of this testing protocol and others, such as 1-on-1, can be found in literature.[23] *N*-on-1 (stepwise ramped fluence) testing is conducted by irradiating the sample site at a fluence that is well below the 1-on-1 threshold for ten shots. If no damage is detected, the same site is irradiated with five more shots at a slightly increased fluence. This is continued until damage is observed in white light, at which point the damage onset fluence is recorded as the *N*-on-1 threshold for that site. The *N*-on-1 test is repeated for five sites on each MLD grating sample to generate an average and a standard deviation, which are reported as the *N*-on-1 threshold and measurement error, respectively.

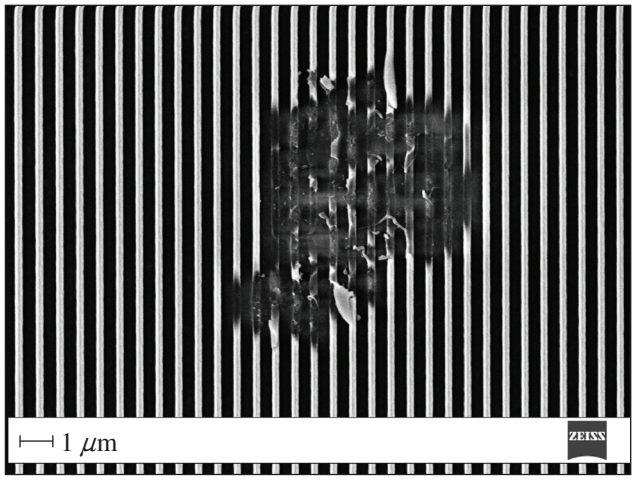

G10719JR

Figure 146.22
A scanning electron microscope (SEM) image of an *N*-on-1 laser-induced–damage site on the multilayer dielectric (MLD) grating structure.

4. Nano-Indentation of MLD Gratings

An MTS Nanoindenter XP fitted with a conical tip (60° included angle, 1-μm tip radius) was used in this work. The system was calibrated by performing nano-indentation on fused silica. Because of the limited imaging capabilities of the instrument and given the submicron scale of the pillar structures, it was not possible to resolve the impressions made by the indenter using the nano-indenter's built-in microscopy; instead, the sample had to be transferred to a scanning electron microscope (SEM) to observe the indents and "wall" damage. Loads in the 0.1- to 0.5-mN range were used and three types of indents could be produced by simply displacing the location of the indentation tip on the grating: centered, partially off-centered, and mostly off-centered indents.

Experimental Results

1. LIDT Results for Gratings and Cleaning Processes

In this study, the fabrication method of gratings was the same across the three samples: 13P-11-56/#566-3, 13P-11-56/#566-5, and 5P-12-56/#644-1. The cleaning procedures detailed earlier were used to prepare these gratings before they were subjected to laser-damage testing. The details of the cleaning methods for our samples are included in Table 146.III. Hereafter, for purposes of brevity, the grating samples will be addressed as #566-3, #566-5, and #644-1.

Two of the gratings (#566-3 and #566-5) that originated from the same coating run were processed together until the cleaning step. The third grating specimen (#644-1) was fabricated a year later using an identical coating process (5P-12-56).

Table 146.III: Summary of LIDT results for gratings and specific cleaning methods used.

Grating	Cleaning Process	Diffraction Efficiency Results (%)	*N*-on-1 LIDT (J/cm^2); air
13P-11-56/#566-3	Partial + air plasma	97.3±0.2	3.66±0.51
13P-11-56/#566-5	Partial + O_2 plasma	97.3±0.5	4.30±0.25
5P-12-56/#644-1	Partial + O_2 plasma	97.9±0.5	1.82±0.08

2. Nano-Indentation Data and Grating Brittleness

Nano-indentation tests were performed on all three grating samples at loads of 0.1, 0.2, 0.3, 0.4, and 0.5 mN. For each sample and at each load, nine indents were made at locations several microns apart. The aim here was to make as many decentered indents as possible. As mentioned in detail elsewhere,[8,24] the centered indents are useful in measuring the yield strength of silica at nanoscale corresponding to this unique geometry. Conversely, off-centered indents are inherently related to fracture of the grating walls, which can now be used to explore a connection with LIDT (associated with fracture as well). This is shown in Fig. 146.23.

Therefore, after performing indentations on the samples, we analyzed each corresponding load-displacement curve to separate the off-centered indents from the centered ones. An example for #566-5 indented at a load of 0.2 mN is shown in Fig. 146.24. The load-displacement curves make a clear distinction between centered and off-centered indents. The centered indent looks similar to an indent in a bulk material[8,24] and has no wall fracture associated with it. The difference, however, from bulk nano-indentation is that in bulk nano-indentation the surrounding material laterally constrains the material deformation. In grating ("wall") nano-indentation, such lateral constraint is reduced because of the small thickness of the silica wall. The other two curves, showing the off-centered indents, include fracture that is seen by the sudden break in the curve (leading to a "plateau") followed by additional loading.

For the purpose of extracting a metric that can be useful in analyzing the mechanical performance of gratings, which can then be compared to their optical performance (LIDT), we located the point of fracture initiation for each of the load-displacement curves. This is illustrated in Fig. 146.25 for grating #566-3 at a load of 0.2 mN. The location of the fracture initiation point (penetration depth Δ) for each indent depends on the amount of decentering; naturally, this is different for each indent (see Fig. 146.25). To evaluate the grating as a whole at

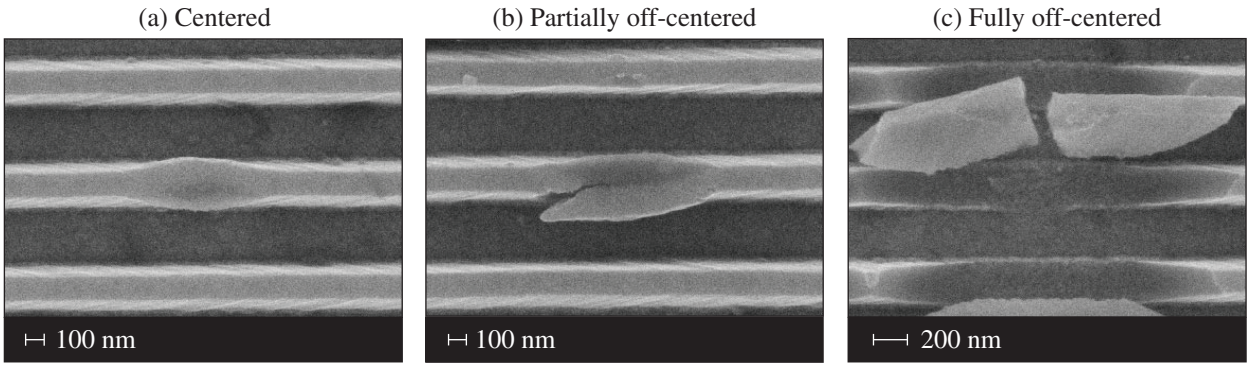

Figure 146.23
Three distinct nano-indentation responses are seen in MLD gratings.

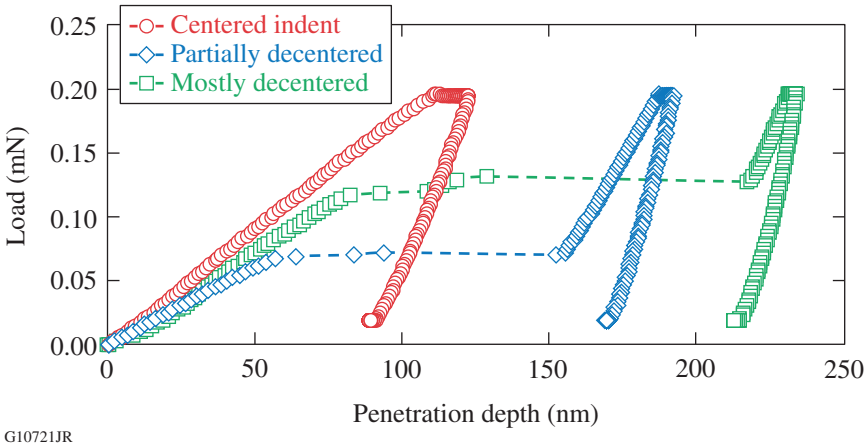

Figure 146.24
Load-displacement curves of nano-indentation for grating #566-5 with a 0.2-mN load.

that particular load, however, we chose the smallest penetration depth across all indents to represent the value at which fracture is initiated. In this example (Fig. 146.25), a penetration depth of 81 nm is the weakest site for failure under a nanomechanical load of 0.2 mN and will be designated as Δ_{min}. Similarly, data can be collected across all three grating samples for a load range of 0.2 to 0.5 mN.

We considered only those indents made at loads varying from 0.2 to 0.5 mN since indentations made at the 0.1-mN load did not yield any discernible instances of fracture.

3. Brittleness, Deformation, and LIDT

The penetration depths corresponding to the weakest sites for fracture initiation (Δ_{min}) at each load and sample are plotted against the measured values of LIDT in Fig. 146.26.

Using the methodology discussed in literature[8] based on the geometry of the grating walls (width at the top of the wall, $w \sim 150$ nm) and contact area a (function of radius of indenter R and load applied P) defined at the time of initiation of fracture corresponding to Δ_{min}, we can determine the yield "strength" of the grating and plot it against measurements of LIDT. The yield strength is a stress found for the maximum load and the impression area. The contact area radius a is found by

$$a = \sqrt{2R\Delta_{min}} \tag{1}$$

and the corresponding uniaxial yield strength by

$$\sigma_Y = \frac{P}{2aw}. \tag{2}$$

The extracted yield stress is correlated to the LIDT in Fig. 146.27.

4. Geometrical Discontinuities and Surface Heterogeneities

The MLD gratings, after cleaning treatments, are observed to have a distinctive type of surface defect as seen in SEM images—disfiguration along the top of the wall (also referred to as "undulations").

Observations from several SEM images such as the ones shown in Fig. 146.28 reveal a direct correlation between the

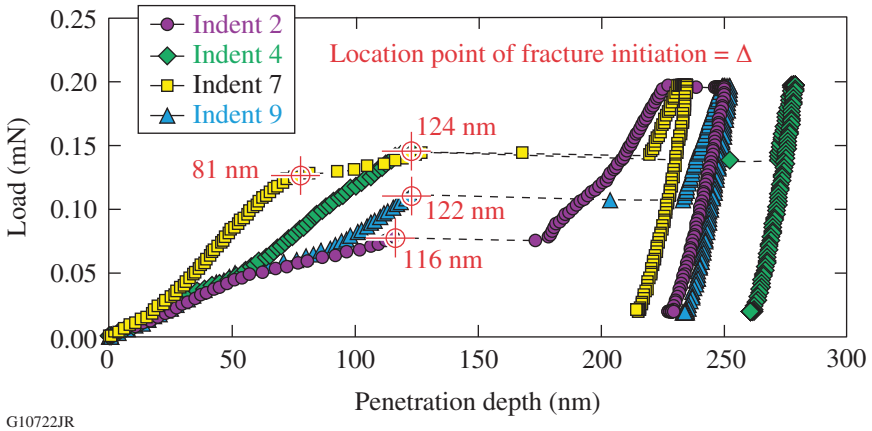

Figure 146.25
The location of fracture initiation is measured using the load-displacement curves for off-centered indents made on MLD grating #566-3 with a 0.2-mN load.

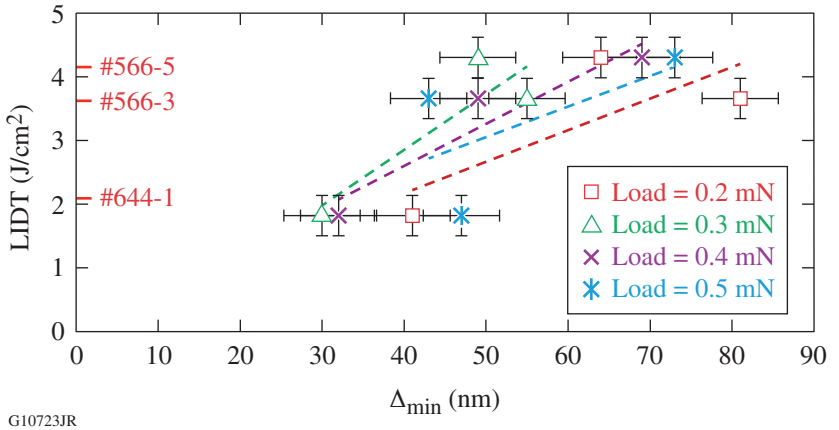

Figure 146.26
Relationship of laser-induced–damage threshold (LIDT) and the minimum depth of penetration into the MLD grating needed to initiate fracture.

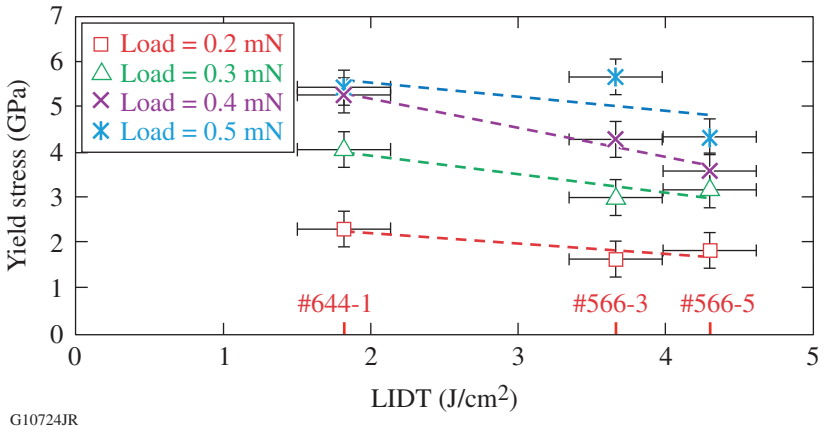

Figure 146.27
Relationship of LIDT and the extracted yield stress.

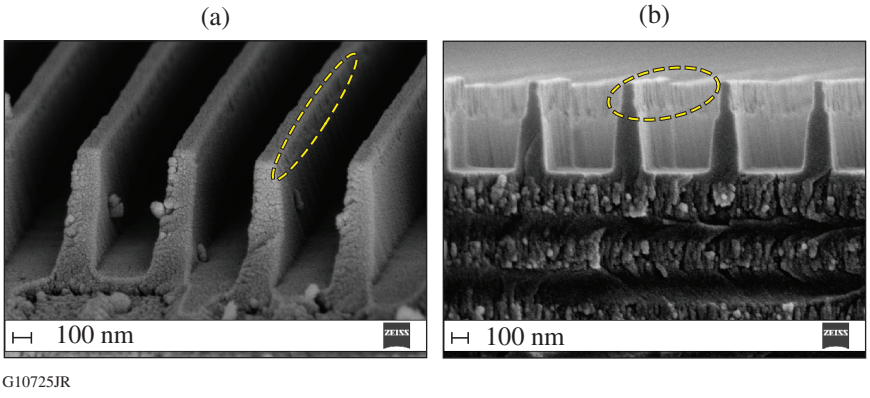

Figure 146.28
Severity of the undulations on the grating walls are related to the measured LIDT.

sizes of the undulations, seen as disfigurement at the top of the grating walls [circled in Figs. 146.28(a) and 146.28(b)], and the measured LIDT. Stronger undulations are associated with gratings that performed poorly in the optical testing, yielding lower values of laser-damage thresholds. Such surface defects (numerically modeled in the next section) are expected to play an important role in determining the quality of a particular grating since they would concentrate electric fields and mechanical stresses associated with nano-indentation. Therefore, they are an important consideration to our experiments.

These defects are thought to be regions of concentration of both mechanical and optical fields and are, therefore, important features to be included in our numerical modeling.

Numerical Simulations

For the numerical simulations, we used the commercial finite element package ABAQUS® (version 6.14-1). Guided by 2-D finite element analysis (FEA) performed previously,[8,25] the nano-indentation experiment was modeled as a 3-D problem using hexagonal, eight-node linear brick elements for the grating structure. The indentation region was significantly smaller than the size of the sample modeled; therefore, this area of large deformation was modeled using a highly refined mesh as compared to regions surrounding it.

The grating structure is defined as an elastic–plastic material composed of silica with an underlying layer of hafnia (~130 nm). The elastic modulus of silica was selected as 95 GPa (Ref. 26) and a Poisson ratio of 0.17. Isotropic hardening was implemented to model plasticity in the material corresponding to a yield stress of 2.8 GPa (based on the work described in Chap. 4 of Ref. 25). Hafnia was modeled as an elastic material with a Young's modulus of 130 GPa and a Poisson ratio of 0.25 (Ref. 26). The indenter tip (~1400-GPa diamond, elastic modulus) was modeled as an analytical rigid body since we did not expect it to deform during the experiment.

The nano-indentation problem was set up for simulation in four different ways as seen in Fig. 146.29. Since the purpose of this work is to correlate optical and mechanical damage fields in grating testing, we will mainly consider simulations of off-centered indents—namely the 25%, 50%, and fully decentered models (details of the centered model are discussed elsewhere[8,25]). Our goal is to simulate the nano-indentation testing. These analyses can then be used

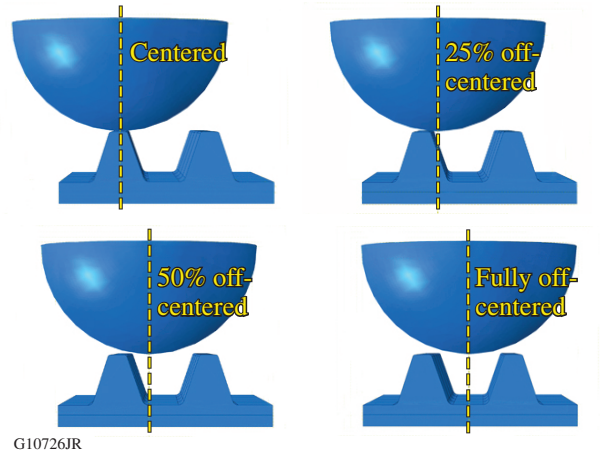

Figure 146.29
The ABAQUS® simulations were run using four setups to represent "centered" and "off-centered" indents.

to evaluate the different regions in a grating structure where stresses are concentrated.

1. Simulation of Off-Centered Nano-Indentation

We have observed (Sec. 4.3.1 of Ref. 25) that a high degree of indenter tip off-center coupled with a relatively deep penetration depth (≳150 nm) of indenter tip corresponds to catastrophic indents on the grating structure. Such "slightly"-to-"mostly" off-centered indents include effects of both ductility and brittle deformation.

Figures 146.30(a)–146.30(d) show the evolution of localized deformation and damage for a 50% decentered indent as the depth of penetration of the indenter tip is increased from 50 nm to 250 nm. The regions of highest concentration of maximum principal stress are seen in the regions of the grating wall that are "stretched" at lower penetration depths. As greater penetration depths of 170 nm and 250 nm are reached, the highest concentrations of maximum principal stress also extend to the adjacent wall since it is also now in significant contact with the indenter tip. This not only causes both the walls to stretch excessively but also affects the "foot" of the wall, which is found to concentrate maximum principal stress. It should be noted here that we have not modeled crack growth in this simulation; therefore, it is highly likely that excessive stretching seen in off-centered indents corresponding to high depths of penetration would indeed fracture the silica walls. In summary, the sequence of events in off-centered indentation consists of mechanical stretching of the grating top, followed by load shearing with neighboring pillars and load transmission to the base of the grating.

2. Simulation of Geometric Discontinuities

The 3-D simulations discussed previously assume that the shape of the grating is rectilinear. We now take into account some of the inhomogeneities that are encountered with gratings that can potentially act as regions to concentrate mechanical stresses in a nano-indentation test and have a direct impact on its laser-damage threshold.

The off-centered nano-indentation experiment is now modeled as a plane-strain simulation in 2-D and is meshed using four-node bilinear plane-strain quadrilateral elements. Highly refined meshing is used near the area of contact with a progressively coarser mesh away from the zone of maximum deformation (grating walls and the top few layers of the grating). The grating structure is modified to include the effects of thickness

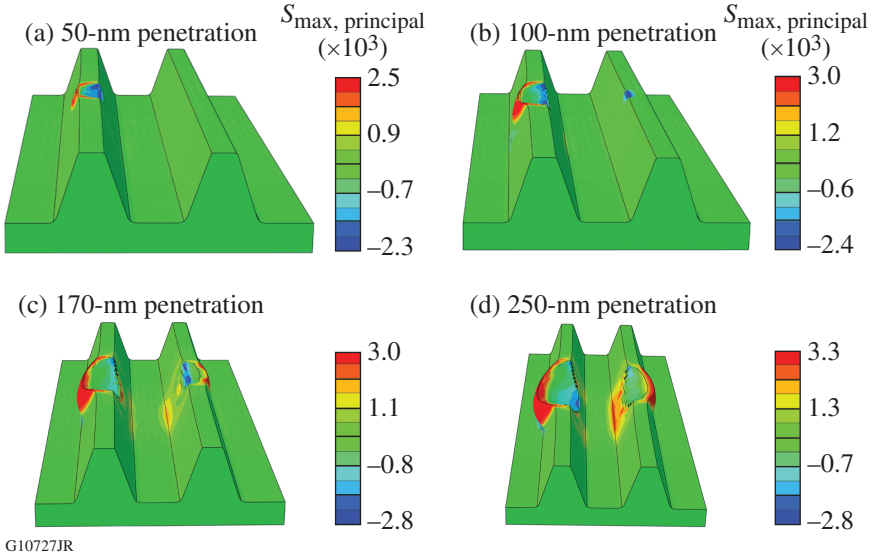

Figure 146.30
Damage is restricted to a single wall for penetration of 50 nm but extends to the adjacent wall as the penetration increases, eventually leading to fracture (stress is given in MPa).

discontinuity evident as disfigurement of the grating walls (undulations shown in SEM images in an earlier section). The results from the simulation are compared to those from an ideal grating structure and illustrated in Figs. 146.31(a) and 146.31(b).

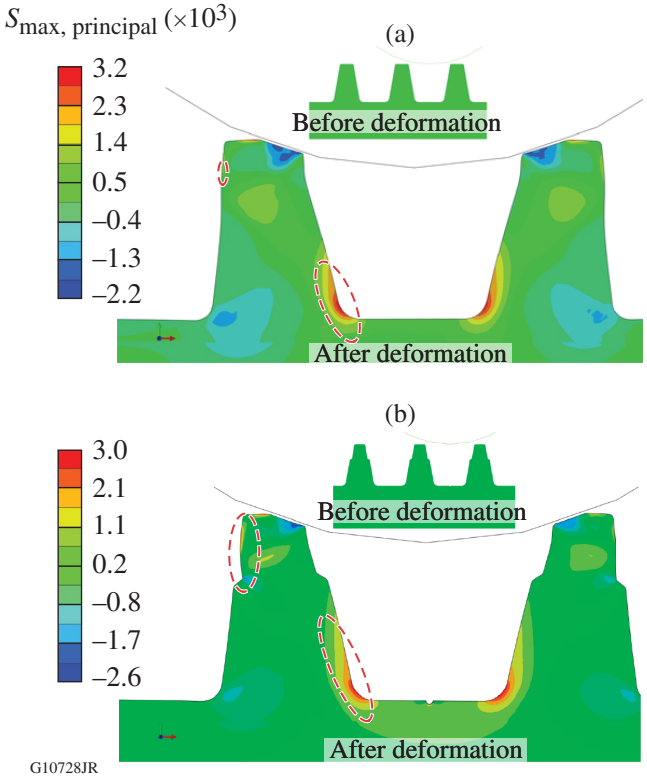

Figure 146.31
Comparison of (a) an ideal grating (no defects) with (b) a disfigured grating simulated for a penetration depth of 50 nm.

It is evident that, for a penetration depth of only 50 nm, the "disfigured" grating concentrates maximum principal stresses at the foot of the grating wall as well as along the undulation (peak stress ~3 GPa), whereas there is no significant accumulation of stresses along the wall of the ideal grating shape.

In addition to the stress concentration along the foot of the grating, the thickness discontinuity includes an additional effect, reminiscent of concentrated plastic shear deformation (shear banding).

The plastic strain (maximum principal component) for ideal and disfigured gratings at a penetration depth of 50 nm is plotted in Figs. 146.32(a) and 146.32(b), respectively. This helps to further assess the areas of the grating structure that are exposed to stress concentration in a nano-indentation test. It is seen that there is a "banding" effect in the upper region of the grating

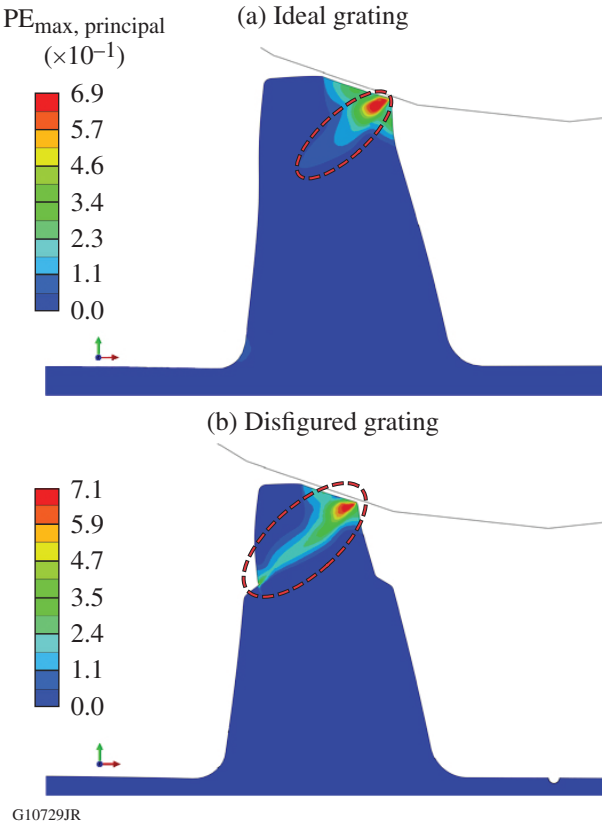

Figure 146.32
(a) A shear band caused by the plastic strain is prominent only in the area of contact with the indenter tip. (b) The shear band for the ideal shape is prominent in the disfigured grating and extends across the top width of the grating wall.

wall where it makes contact with the indenter tip. This "band," or the region under plastic strain, is significantly evolved in the disfigured grating as compared to the ideal grating structure.

We have also modeled nanometer-sized porosity at the grating "floor." A 100-nm pore is shown in Figs. 146.30(b) and 146.31(b). Such pores also concentrate tensile mechanical stresses, exactly as they concentrate electrical fields[27–30] by enhancing localized absorption effects.[31]

Discussion

1. Effect of Cleaning Procedures on LIDT

The cleaning procedure is widely reported to have a significant impact on the damage threshold of these pulse-compression gratings.[18,20] Extensive research dedicated to studying the effects of various cleaning processes (Piranha at different temperatures, Nano-Strip)[9,32–36] on the threshold at 10 ps, 1053 nm shows that the efficiency of the process (measured by reduction in traces of photopolymers and organic contaminants after cleaning) is linked to the LIDT measured for the grating.

For our purposes, subtle differences in the cleaning processes (shown in Table 146.III), such as using air plasma over oxygen plasma, cause significant changes in the measured LIDT for the respective gratings. Specifically, this is the only difference between gratings #566-3 and #566-5 (which were processed identically until this point), and yet the latter performed much better in optical testing (LIDT 4.3±0.25 J/cm^2). The same is true in comparing #566-3 and #644-1. Therefore, it must be emphasized that, although these differences in cleaning procedures might seem insignificant, they lead to critically different optical performances.

It must also be noted that although we have shown that changes in cleaning methods have led to vastly different values of measured LIDT, this is not the main purpose of this study, and they are discussed elsewhere.[2,7,20]

2. Thickness Undulation and Concentration of Mechanical Fields

Guided by SEM images (in Fig. 146.28) and LIDT data, an apparent relationship between the shape of the top of the grating wall and the optical performance of the grating can be summarized as follows:

- Undulations can amplify electric-field intensification in those regions, leading to higher damage probability.

- Two-dimensional finite element analysis shows higher stress concentrations and shear band development in a disfigured grating for the same ~50-nm penetration depths.

The primary purpose of the 3-D simulation was to identify the regions of the grating structure that are affected in a nano-indentation test and then use these regions to compare nano-indentation to the results from a laser-damage–threshold test. Specifically, for a 50% off-centered indent, Fig. 146.30 shows that the highest levels of maximum principal stress are concentrated in the stretched part of the wall at lower levels of penetration depth. This region can be thought of as the site of fracture initiation in the nano-indentation experiment.

The indentation depth at which the maximum principal stress exceeds the fracture stress of silica corresponds to the location of the point of fracture initiation (compare to Δ_{min} indicated in load-displacement curves; see Fig. 146.25). The numerical simulations (Fig. 146.30) indicate that this indentation depth is in the 50-nm to 100-nm range, which corresponds well with experimental data. As indentation depths increase, fracture becomes imminent and is suggested by the spatial increase in stretched regions of the grating wall (near the top) as well as adjoining areas where stress is concentrated—the stretched region in the adjacent grating wall and foot of the grating.

It is widely reported in literature[16,17,19,37,38] that in a laser-damage–threshold test, the damage to the MLD grating appears to start at the upper edge of the silica walls—where the modulus of the square of the electric field is highest.[16,17] SEM images of our gratings (Fig. 146.28) after cleaning show distinctive disfigured regions at the top of the grating wall, which in some cases have thinned the gratings to a great extent. Guided by these SEM images and LIDT data, there is an apparent relation between the shape of the top of the grating (or, severity of undulations created) and the respective values of damage threshold measured in optical testing. Gratings with smaller degrees of thickness disfigurement are associated with higher values of laser-damage thresholds. Any inhomogeneity along the top of the grating wall will amplify the catastrophic effects of the laser energy used to irradiate these gratings.

Having established that analyzing these undulations is an important aspect of understanding why gratings behave differently in LIDT, we can now discuss how nanomechanical testing of these silica walls can be used to understand their performance. For a penetration depth of 50 nm, it is observed in the 2-D finite element model that the two highlighted regions in the figure for the ideal [Fig. 146.31(a)] and disfigured [Fig. 146.31(b)] grating concentrate the highest levels of (tensile) maximum principal stress. Based on the area around the top of the grating wall, it is clear that for a given penetration depth, the disfigured grating experiences much higher levels of stress (~2.5 GPa) as compared to an ideal grating in the same region (<1 GPa). This shows that mechanical stresses are amplified greatly for a disfigured grating, and, as the severity of undulations increases, it can be expected that stresses would also increase, ultimately leading to a mechanical failure of the grating wall.

Plastic strains are also useful in understanding deformation of these gratings, and it is seen that during the nano-indentation test, a "shear band" develops as contact proceeds. Figures 146.32(a) and 146.32(b) compare the shear bands of ideal and disfigured grating structures, respectively. Clearly, the banding effect is more severe in the case of the grating with an undulation and extends across the width of the wall along the region where it is disfigured. Strains as high as 45% are seen in regions away from the contact area and are highlighted in the figure. The shear band in the ideally shaped grating is contained mostly within the area that is in contact with the indenter tip.

It must also be noted that the penetration depth chosen here (50 nm) to model the nano-indentation stresses in the grating is similar to the values of Δ_{min}, from the load-displacement curves, which represents the point of fracture initiation. Therefore, it can be inferred that under nanomechanical testing, the gratings with more-severe undulations will fracture before gratings that are relatively free of these features. This result is critical in explaining why gratings with a lower Δ_{min} have a lower LIDT (shown in Fig. 146.26). We also note that these simulations highlight that a nanomechanical test exposes regions of the grating structure that are impervious to its laser-threshold performance statistics.

3. Correlation of Optical and Mechanical Tests (LIDT and Δ_{min})

Figure 146.26 shows LIDT for the three differently cleaned gratings against Δ_{min} at various loads used to measure the nano-indentation. It is apparent that there is a strong linear dependence of Δ_{min} on the measured LIDT (J/cm^2). LIDT increases with increasing values of Δ_{min}; that is, the more "brittle" a grating, the lower its damage threshold. This correlation is novel and important for two different reasons. First, it provides us with a quantitative metric that can be used to predict optical performance of gratings based on nanomechanical tests alone. Simply put, a grating that shows an earlier initiation of fracture in an off-centered nano-indentation test (tracked using load-displacement curves) has a greater likelihood to be associated with a lower LIDT value as compared to a grating that could absorb more mechanical stress before fracture initiation. Second, this result can also be extended to correlate yield stress in these gratings (at the time of first fracture) to their respective laser-damage thresholds. The relation of LIDT and yield stress in Fig. 146.27 indicates that a grating with a higher LIDT will have a lower value of yield stress. This means that for decreasing yield strength, the grating is more ductile or can absorb more mechanical energy before it fractures. In summary, gratings with higher ductility demonstrate higher LIDT.

It is also worth noting from Fig. 146.26 that the correlating lines, when extended, have intercepts near zero. Of course, all gratings have a nonzero LIDT; however, this observation indicates that, if the deflection Δ_{min} to fracture is practically nil, the resulting LIDT also vanishes. Such a correlation of fracture and LIDT is in agreement with the discussion in this section.

We will now discuss first-principles–based dimensionless metrics for correlating our results between nano-indentation and optical performance. Our goal is to cast our results in a way that may extend their range of validity to experimental conditions, other than the ones we have used here. In essence, we are seeking appropriate ways to cast our experimental results in a dimensionless form.

Higher ductility in grating structures can be considered in terms of stretched zones as indicated in finite-element simulations [Fig. 146.30(c)]. This stretching before fracture initiation in an off-centered indent is attributed to the (tangential) stress (hoop) exerted by the indenter. This phenomenon is broadly analogous to an internally pressurized cylinder. The pressure causes the cylinder to expand or stretch and we can calculate a hoop strain ($\varepsilon_{\theta\theta}$) associated with it. The fracture strain is calculated for the penetration depth (Δ_{min}) at which stretching leads to fracture initiation and also depends on the indenter's radius and the grating pitch.[25] We can now normalize Δ_{min} by the hoop strain ($\varepsilon_{\theta\theta}$).

We also need to normalize LIDT's to some nominal threshold fluence. It is reported in Ref. 39 that the damage in the optical material is established once the temperature of the defect-surrounding material reaches its melting point. Therefore, threshold fluence as a function of this critical temperature (melting point of the optical material, which, in our case, is silica) can be now estimated as

$$F_0 = \frac{3.1\,T_c K_h \sqrt{\tau}}{\gamma \sqrt{D}} = 2.8 \text{ J/cm}^2, \tag{3}$$

where F_0 is the threshold damage fluence, T_c is the critical temperature or the melting point of silica ≈1900 K, K_h is the thermal conductivity = 1.4 W/(mK), τ is the pulse duration = 10 ps, D is the thermal diffusivity (for silica) = 0.0075 cm^2/s, and γ is the absorptivity at 1053 nm = 10^{-3}.

Therefore, the LIDT of the gratings can be normalized to F_0. The dimensional plot shown earlier in Fig. 146.26 is replotted in Fig. 146.33 by using dimensionless quantities. This plot may be used to ascertain the trend that, for increasing fracture strains, the normalized laser-induced–damage fluence will also increase. As the correlating lines pass through the origin, the implication is that high brittleness would lead to very low LIDT.

Conclusions

A novel analysis has been presented to show that nano-indentation testing, supported by SEM images and finite-element simulations, can be effectively used to interpret the quality of a grating post-cleaning. The most widely accepted metrics to rate the performance of MLD gratings used in

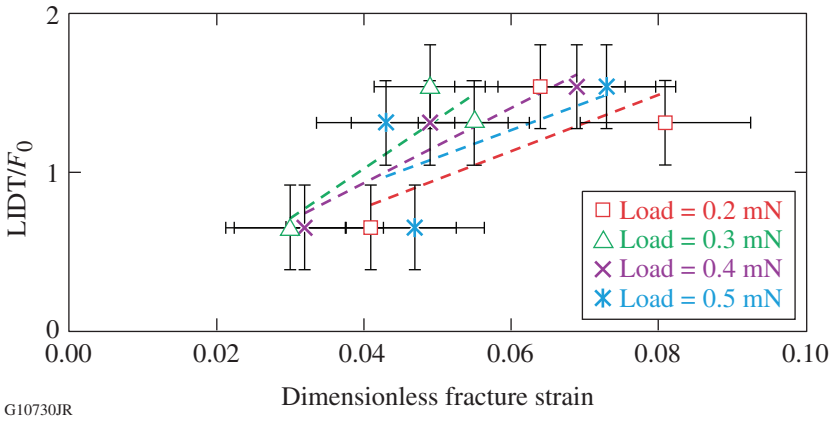

Figure 146.33
Normalized plot showing the dependence of damage thresholds on fracture strain developed in gratings during nano-indentation testing.

high-powered laser systems are expressed through optical tests in the form of LIDT's. Not only do nanomechanical tests naturally complement laser-damage testing by providing a fracture-derived metric (Δ_{min}) that distinguishes between grating samples based on their propensity to fracture, but they also expose identical regions of the grating structure to stresses as in a laser-damage test. The analogy is illustrated in Fig. 146.34. Therefore, we have argued that nanomechanical testing carried out in the proposed way (that is, identifying the weakest mode of the grating deformation) can be implemented as a rapid first test to predict how MLD gratings will perform when subjected to more-rigorous and specialized optical tests such as laser-damage testing.

In Fig. 146.34, we summarize schematically the analogy between stress/strain field concentration and electromagnetic-field concentration.

The main conclusions from this study are as follows: (1) Subtle changes in grating cleaning techniques lead to significant changes in the measured LIDT. (2) Our work shows a strong correlation between the nanomechanical fracture-based metric Δ_{min} and LIDT measured through optical testing for the grating samples evaluated. It is observed that a smaller value of LIDT is associated with a smaller Δ_{min} or, simply, a grating that has a tendency to fracture easily in a nano-indentation test will most likely have the lowest laser-damage threshold. (3) LIDT decreases as the measured yield stress for the grating samples increases. In other words, the less-deformable gratings lead to reduced LIDT. (4) The presence and size of undulations, or surface heterogeneities, on the grating structure have a direct impact on how the grating performs in both mechanical and optical tests. A grating with severe disfigurement at the top of the wall is more likely to have a low value of LIDT, as compared to a grating that was relatively free of this artifact. (5) Off-centered nano-indentation and LIDT measurements expose the same regions of the structure of the MLD grating and, therefore, can be seen as complementary tests.

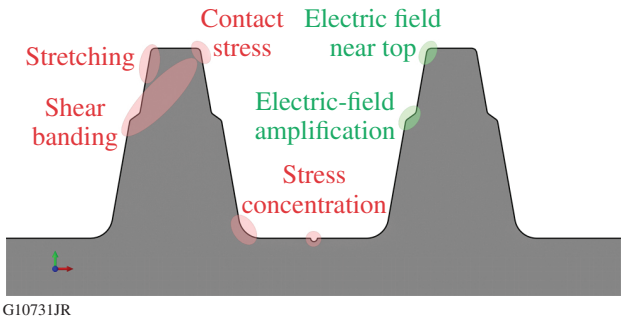

Figure 146.34
Nano-indentation exposes the same areas of the grating structure as an optical test by concentrating mechanical fields (stress, strain) in the regions normally associated with amplified electric fields.

In summary, we have presented a novel way of using nano-indentation testing, electron microscopy, and finite-element simulations to interpret the LIDT's of amorphous silica optical gratings.

ACKNOWLEDGMENT

The authors express their appreciation to the University of Rochester's Laboratory for Laser Energetics (LLE) for continuing support. One of the authors (K. Mehrotra) is supported by an LLE Horton Fellowship. This material is based upon work supported by the Department of Energy National Nuclear Security Administration under Award Number DE-NA0001944, the University of Rochester, and the New York State Energy Research and Development Authority. The support of DOE does not constitute an endorsement by DOE of the views expressed in this article.

The authors thank the late Dr. S. D. Jacobs for useful discussions that helped in conceiving this work. We also thank B. Patterson for her help in numerical simulations.

REFERENCES

1. F. Kong *et al*., Opt. Laser Technol. **73**, 39 (2015).
2. H. P. H. Liddell, "Enhancing the Performance of Multilayer-Dielectric Diffraction Gratings Through Cleaning Process Modifications and Defect Mitigation," Ph.D. thesis, University of Rochester, 2013.
3. D. Strickland and G. Mourou, Opt. Commun. **56**, 219 (1985).
4. G. A. Mourou, in *Encyclopedia of Modern Optics*, edited by R. D. Guenther, D. G. Steel, and L. P. Bayvel (Elsevier Academic Press, Amsterdam, 2005), pp. 83–84.
5. L. J. Waxer, D. N. Maywar, J. H. Kelly, T. J. Kessler, B. E. Kruschwitz, S. J. Loucks, R. L. McCrory, D. D. Meyerhofer, S. F. B. Morse, C. Stoeckl, and J. D. Zuegel, Opt. Photonics News **16**, 30 (2005).
6. J. A. Britten *et al*., Proc. SPIE **2714**, 511 (1996).
7. H. P. Howard, A. F. Aiello, J. G. Dressler, N. R. Edwards, T. J. Kessler, A. A. Kozlov, I. R. T. Manwaring, K. L. Marshall, J. B. Oliver, S. Papernov, A. L. Rigatti, A. N. Roux, A. W. Schmid, N. P. Slaney, C. C. Smith, B. N. Taylor, and S. D. Jacobs, Appl. Opt. **52**, 1682 (2013).
8. K. Mehrotra, H. P. Howard, S. D. Jacobs, and J. C. Lambropoulos, AIP Adv. **1**, 042179 (2011).
9. M. L. Schattenburg *et al*., the International Symposium on Nano-manufacturing (ISNM 2006), Cambridge, MA, 1–3 November 2006 (Paper TS3C-44).
10. J. R. Greer, W. C. Oliver, and W. D. Nix, Acta Mater. **53**, 1821 (2005).
11. J.-Y. Kim and J. R. Greer, Acta Mater. **57**, 5245 (2009).
12. J.-Y. Kim, D. Jang, and J. R. Greer, Acta Mater. **58**, 2355 (2010).
13. W. D. Nix *et al*., Thin Solid Films **515**, 3152 (2007).
14. R. Lacroix *et al*., International Journal of Applied Glass Science **3**, 36 (2012).
15. R. Lacroix *et al*., Acta Mater. **60**, 5555 (2012).
16. J. Neauport *et al*., Opt. Express **15**, 12508 (2007).
17. S. Hocquet, J. Neauport, and N. Bonod, Appl. Phys. Lett. **99**, 061101 (2011).
18. *LLE Review Quarterly Report* **112**, 228, Laboratory for Laser Energetics, University of Rochester, Rochester, NY, LLE Document No. DOE/SF/19460-790 (2007).
19. J. B. Oliver, T. J. Kessler, H. Huang, J. Keck, A. L. Rigatti, A. W. Schmid, A. Kozlov, and T. Z. Kosc, Proc. SPIE **5991**, 59911A (2005).
20. *LLE Review Quarterly Report* **131**, 149, Laboratory for Laser Energetics, University of Rochester, Rochester, NY, LLE Document No. DOE/NA/28302-1034 (2012).
21. H. T. Nguyen, C. C. Larson, and J. A. Britten, Proc. SPIE **7842**, 78421H (2010).
22. J. Keck, J. B. Oliver, T. J. Kessler, H. Huang, J. Barone, J. Hettrick, A. L. Rigatti, T. Hoover, K. L. Marshall, A. W. Schmid, A. Kozlov, and T. Z. Kosc, Proc. SPIE **5991**, 59911G (2005).
23. C. R. Wolfe *et al*., in *Laser Induced Damage in Optical Materials: 1989*, edited by H. E. Bennett *et al*., Natl. Inst. Stand. Technol. (U.S.), Spec. Publ. 801 (U.S. Government Printing Office, Washington, DC, 1990), pp. 360–375.
24. K. Mehrotra, H. P. Howard, S. D. Jacobs, and J. C. Lambropoulos, in *Local Probing Techniques and* In-Situ *Measurements in Materials Science*, edited by N. Balke *et al*., Mater. Res. Soc. Symp. Proc. Vol. 1474, mrss12-1474-ccc08-13 (Materials Research Society, Pittsburgh, PA, 2012).
25. K. Mehrotra, "Nano-Mechanics of Optical Structures for High Laser-Damage Threshold Applications," Ph.D. thesis, University of Rochester, 2016.
26. K. Mehrotra, J. B. Oliver, and J. C. Lambropoulos, Appl. Opt. **54**, 2435 (2015).
27. N. Bloembergen, Appl. Opt. **12**, 661 (1973).
28. Y. Jee, M. F. Becker, and R. M. Walser, J. Opt. Soc. Am. B **5**, 648 (1988).
29. A. Salleo *et al*., Proc. SPIE **3244**, 341–347 (1998).
30. F. Y. Génin *et al*., J. Opt. Soc. Am. A **18**, 2607 (2001).
31. S. Papernov and A. W. Schmid, J. Appl. Phys. **82**, 5422 (1997).
32. D. J. Smith *et al*., in *International Conference on Ultrahigh Intensity Lasers: Development, Science and Emerging Applications (ICUIL 2008)* (ICUIL, Tongli, China, 2008), pp. 78–79.
33. B. Ashe *et al*., Proc. SPIE **6720**, 67200N (2007).
34. B. Ashe, K. L. Marshall, C. Giacofei, A. L. Rigatti, T. J. Kessler, A. W. Schmid, J. B. Oliver, J. Keck, and A. Kozlov, Proc. SPIE **6403**, 64030O (2007).
35. S. Chen *et al*., Proc. SPIE **7655**, 765522 (2010).
36. S. Chen *et al*., High Power Laser Part. Beams **23**, 2106 (2011).
37. J. A. Britten *et al*., Proc. SPIE **5273**, 1 (2004).
38. B. C. Stuart *et al*., Proc. SPIE **2714**, 616–629 (1996).
39. S. Papernov, in *Laser-Induced Damage in Optical Materials*, edited by D. Ristau (CRC Press/Taylor & Francis, Boca Raton, FL, 2014), Sec. I, Chap. 3, pp. 25–74.

Permeation Fill-Tube Design for Inertial Confinement Fusion Target Capsules

Introduction

In inertial confinement fusion (ICF)[1] a target capsule containing a cryogenic deuterium–tritium (DT) ice layer and low-density DT gases is imploded directly by intense laser pulses[2] or indirectly by x rays in a hohlraum.[3] During a typical implosion, intense illumination of the target rapidly heats and ablates the outer capsule material. Conservation of momentum drives the remaining capsule material and fuel toward the center of the target sphere, where the initially gaseous fuel forms a "hot spot" that ignites fusion reactions, which propagate radially outward through the main fuel layer.[3] The ultimate goal of ICF is to ignite the imploding target capsule, producing net energy gain; however, during an implosion, hydrodynamic instabilities in the ablation front can reduce the energy yield by distorting the hot spot or dispersing the main fuel layer.

Currently, two main methods are being used to fill the ICF target capsule with DT fuel—fill-tube filling[4] and permeation filling.[5] In fill-tube filling, a small fill tube provides a connection between the empty target capsule and a reservoir of gaseous DT. A valve downstream of the supply is opened, and DT flows into the target capsule. Once the desired amount of DT is inside the target capsule, the supply is shut off.

Permeation filling has no fill-tube connection between the empty target capsule and a reservoir of gaseous DT. Instead, this method relies on the target capsule being permeable to DT at the filling temperature and nonpermeable at some lower temperature. A valve downstream of the supply is opened and, at a controlled pressure ramp rate, DT flows into a heated pressure vessel containing an empty target capsule. The buckling strength and permeability of the target capsule shell limit the rate of DT pressure rise.[6] Once the desired amount of DT has entered the target capsule, corresponding to the maximum DT fill pressure, the supply valve is closed. The pressure vessel and target capsule are then cooled to a temperature at which the internal pressure will not cause the target capsule to rupture or leak extensively when DT in the chamber surrounding the target capsule is evacuated.

One common capsule material (i.e., ablator) used in permeation filling is made by using the glow-discharge polymerization (GDP) process.[7] Alternate ablators such as beryllium, silicon, and high-density carbon are of interest in ICF experiments that study hydrodynamic instabilities.[8] Unfortunately, target capsules made of these materials are not sufficiently permeable to DT to be used in permeation filling. The current infrastructure at LLE is based on permeation filling. To study alternate ablator materials, a new cryostat design based on a fill-tube fill system is required—a multiyear, multimillion dollar project. A novel design combining the attributes of permeation and fill-tube filling is described next. This design requires no changes to LLE's current infrastructure, which will allow the study of alternate ablator materials in cryogenic experiments to begin immediately.

Description of the Permeation Fill-Tube Design

The permeation fill-tube (PFT) target assembly is shown in Fig. 146.35, while a more detailed image of the upper portion of the assembly is shown in Fig. 146.36. The gravity vector points down in these images. The geometry of the target support is driven by the requirement that the target capsule must be at the same elevation or lower than the permeation cell, and the support structure must not interfere with the laser beams.

Figure 146.37 shows a typical PFT assembly. The permeation cell is connected to the target capsule by a fill tube with adhesive joints. The fill tube itself is made of two separate tubes that are also glued together. The larger-diameter tube is fused silica with an outer polymeric coating and has an outer diameter (OD) of 0.15 mm and inner diameter (ID) of 0.10 mm. The smaller-diameter tube is borosilicate glass and is tapered from an OD of 0.1 mm and ID of 0.080 mm to an OD of 0.030 mm and ID of 0.022 mm. Smaller diameters for fill tubes will be investigated in the future. The initial geometry was chosen because of its high rigidity and strength for initial filling and layering experiments.

The PFT method combines attributes of fill-tube filling[4] and permeation filling.[6] Here the target capsule is nonpermeable to

DT while the permeation cell is permeable to DT at the filling temperature and nonpermeable at some lower temperature. A valve downstream of the supply is opened and, at a controlled pressure ramp rate, DT flows into a heated pressure vessel containing an empty PFT target assembly (shown in Fig. 146.35). The buckling strength and permeability of the target capsule shell limit the rate of DT pressure rise.[6] DT flows through the permeation cell's shell through the fill tube and into the target capsule. At a steady state the gas pressure is equal in both capsules. Once the desired amount of DT has entered the PFT assembly, corresponding to the maximum DT fill pressure, the supply valve is closed. The pressure vessel and the PFT target assembly are then cooled to a temperature at which the internal assembly's pressure will not cause the target capsule or the permeation cell to rupture or leak appreciably when DT in the chamber surrounding the PFT assembly is finally evacuated.

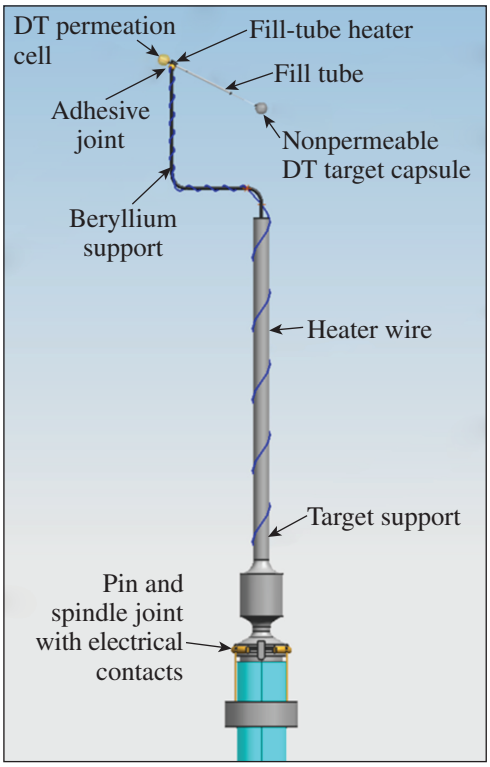

Figure 146.35
Permeation fill-tube target assembly. DT: deuterium–tritium.

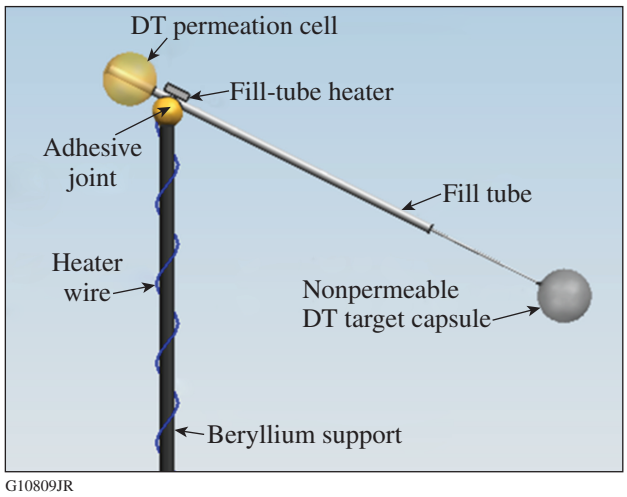

Figure 146.36
Detailed view of the upper portion of a permeation fill-tube target assembly.

The heater glued to the fill tube (shown in Figs. 146.35 and 146.36) is a microchip resistor (ERJ-XGNF1–1Y) capable of delivering up to ~1 mW. The heater creates a pressure delta to drive more fuel into the target capsule than the permeation cell during the layering process. Without this heater, the pressures in the target capsule and the permeation cell would be equal.

The initial PFT prototype did not use nonpermeable ablators, such as beryllium, silicon, and high-density carbon (HDC), since, because of their opacity to visible light, the ice layers would not have been visible. LLE uses optical backlit shadowgraphic characterization of cryogenic target ice layers with submicron resolution.[9] The initial PFT assembly with a HDC target capsule, used for our manufacturing studies, is shown in Fig. 146.38(a). The PFT assembly in our layering studies used GDP capsules for both the permeation cell and the

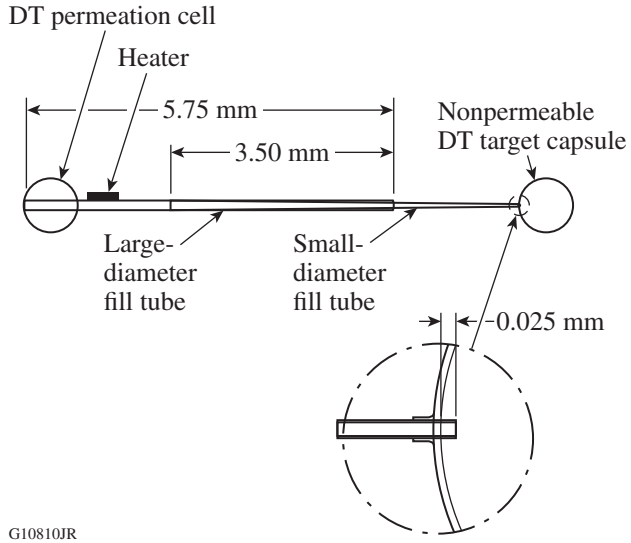

Figure 146.37
Permeation fill-tube assembly. (All dimensions are in millimeters.)

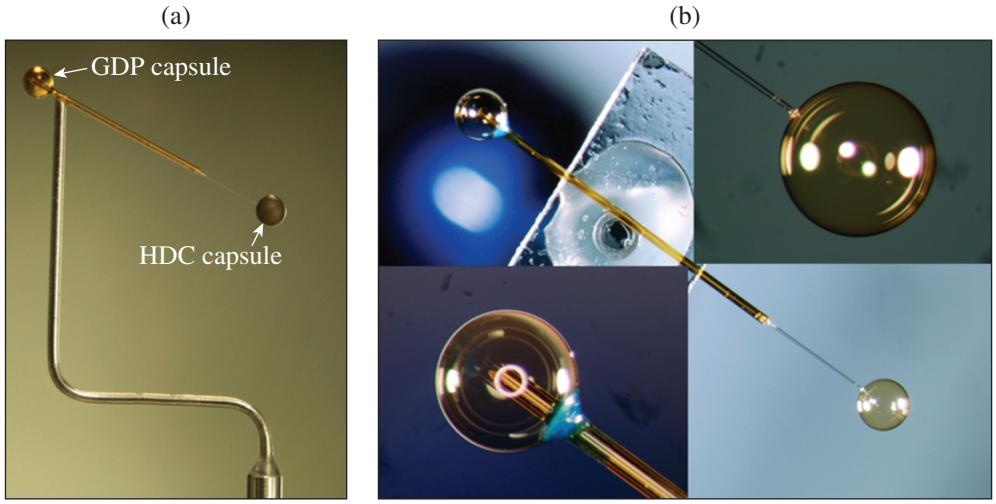

Figure 146.38
(a) Image of a PFT target assembly with a glow-discharge polymerization (GDP) permeation cell and high-density carbon (HDC) nonpermeable target capsule; (b) image of a PFT assembly with a GDP permeation cell and GDP target capsule.

target capsule [see Fig. 146.38(b)]. The target capsule was made from GDP so the ice layer would be visible for layering studies. Both capsules had an OD of 0.430 mm, with wall thicknesses of 0.022 and 0.008 mm for the permeation cell and the target capsule, respectively. A future fill will use a nonpermeable multilayer (GDP/Si/GDP) target capsule shell.

PFT Layering Process

The PFT assembly is located inside a copper layering sphere filled with helium (see Fig. 146.39). Initially DT in the PFT assembly is rapidly cooled (~1 K/s) to several degrees below its triple point. Next, the temperature of the copper layering sphere is gradually raised until all of the solid DT in the target capsule is gone and the solid DT in the fill-tube section nearest the target capsule begins to melt. At this point the temperature of the layering sphere is dropped ~0.001 mK every 15 min. This causes the DT to solidify and an ice crystal "seed" to grow out of the fill tube into the target capsule. The initial growth of a single ring (shown in Fig. 146.40) indicates that, as the temperature continues to drop, the final ice layer will contain a single hexagonal close-packed (hcp) crystal, as required for high-yield ICF implosions.[10]

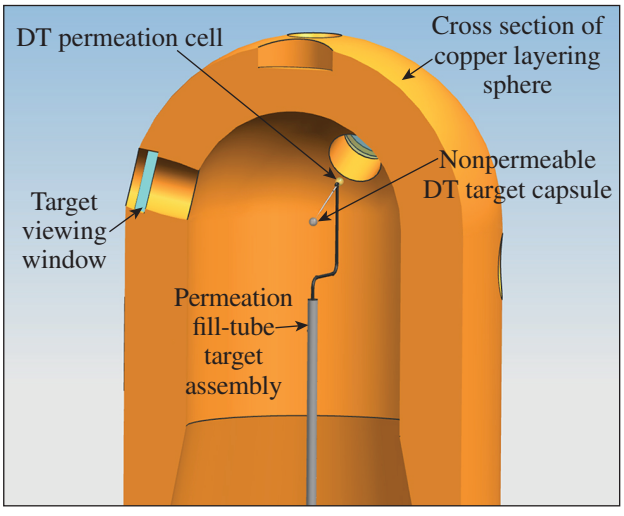

Figure 146.39
PFT assembly located inside a copper layering sphere.

Layering experiments were successful using the same layering protocol as existing stalk-mounted (non-fill-tube)

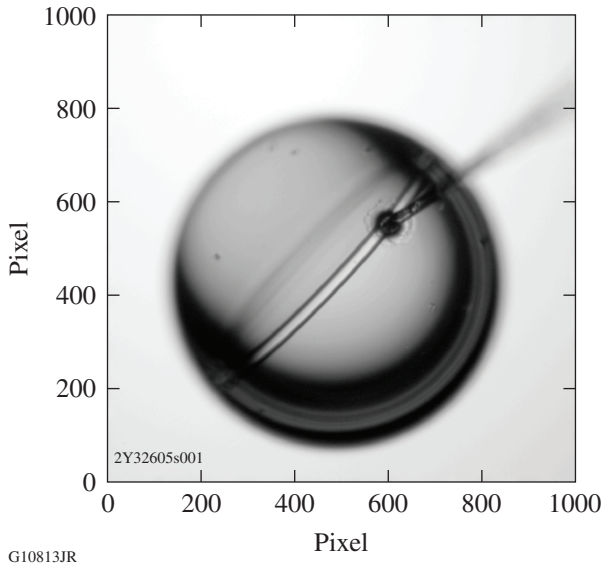

Figure 146.40
Image of single crystal seed that grows out of the fill tube. The initial growth of a single ring is indicative of a final ice layer that will be composed of a single hexagonal close-packed (hcp) crystal, which is required for high-yield ICF implosions.[10]

targets. An image of the resulting single-hcp-crystal ice layer characterized by optical backlit shadowgraphy is shown in Fig. 146.41(a). The inner ice surface roughness is 0.98-μm rms (root mean square) and the average ice thickness is 61 μm. Figure 146.41(b) shows the inner ice surface radius in red and outer ice surface radius in blue. The difference between the blue curve and the red curve is the ice thickness. (A smaller radius of the inner ice surface, shown in red, corresponds to a thicker ice layer.) The image is unwrapped with the zero position referring to the 3:00 position in Fig. 146.41(a). The stalk position is ~50°, leading to thick ice near the fill tube (highlighted). The test ice layer is significantly thicker near the fill tube because of the higher (~6×) thermal conductivity of borosilicate glass compared to helium. From Fig. 146.41(b) it appears that the maximum variation in ice thickness near the fill tube is ~7 μm, but it is actually larger because the fill tube obscures the shadowgraph data, causing the image analysis to fail in this area. From Fig. 146.41(b), the effect of the fill tube is seen over ~±23° on either side of the fill tube. The thick spot will be discussed further in the next section.

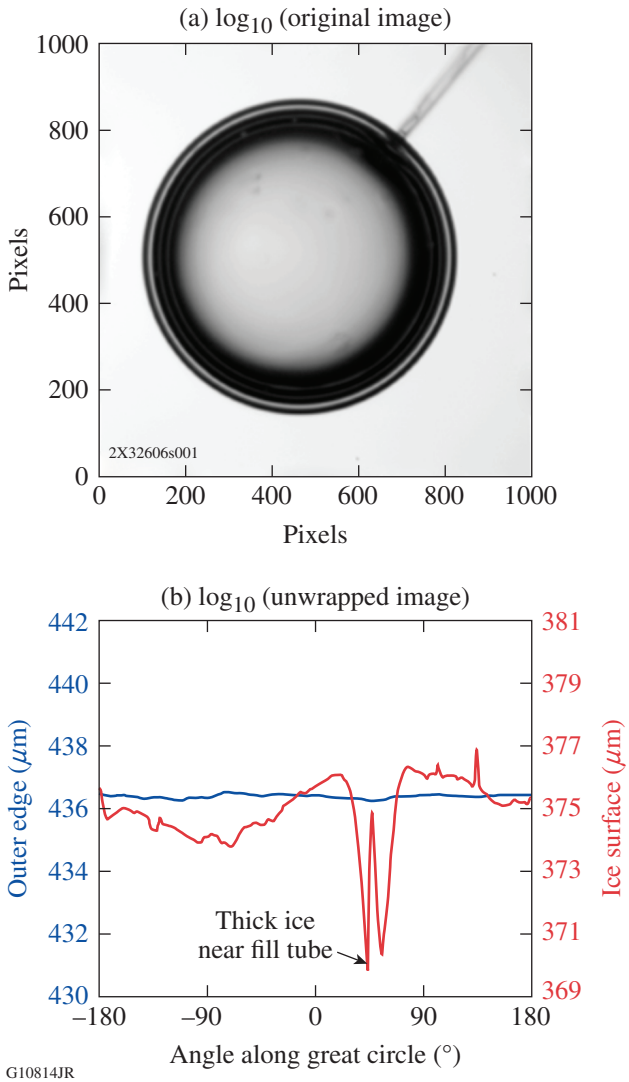

Figure 146.41
(a) An image of a final single hcp crystal ice layer characterized by optical backlit shadowgraphy; (b) the inner ice surface radius is shown in red and the outer ice surface radius in blue.

It is possible to control the relative pressure of DT in the two capsules by using the PFT heater located near the permeation cell shown in Fig. 146.36. With the heater turned on (~1 mW) and the layering-sphere temperature above the critical point of DT, ~40 K, gas is preferentially driven toward the target capsule. Next, the DT in the layering sphere is rapidly cooled (~1 K/s) several degrees below DT's triple point, causing the DT in the target capsule and the fill tube's end attached to the target capsule to freeze. At this point the PFT heater is turned off and the layering process described previously can begin. As long as the ice plug remains in the fill tube during the subsequent layering process, the amount of DT in the target capsule will remain constant.

Heat-Transfer Model

It is preferable to use a heat-transfer model to investigate the effects of the fill tube, glue spot, target capsule geometry, and material properties on layer-thickness uniformity for PFT ICF targets. If the layer-thickness uniformity of the current design can be accurately modeled, we are confident that we will be able to numerically evaluate future ICF target designs. Using models to design targets is more efficient than building physical prototypes.

The DT solid/gas phase boundary is represented by an isotherm at DT's triple point of ~19.7 K. The PFT temperature profile was modeled by a finite volume method (FVM) using ANSYS *FLUENT* v16. A two-dimensional axisymmetric model of the PFT target assembly inside a 1-in.-diam copper layering sphere filled with ~2 Torr of helium was constructed. The model includes both capsules, the fill tube, the glue spot connecting the target capsule to the fill tube, DT decay heating, and sublimation/deposition of DT in the permeation cell, fill tube, and target capsule. The layering sphere was treated as a complete surface and is represented by a uniform-temperature boundary condition. Holes in the layering sphere were ignored so a computationally efficient axisymmetric model can be used.

Decay heating of DT causes the target to be hotter than its surroundings. Helium was used to conduct the heat generated

by DT to the surrounding copper sphere. In the model, DT can exist in only one of two phases—solid or gaseous. The sublimation/deposition temperature used for DT was 19.7 K. Initial models used *FLUENT*'s two-phase routines. Since only steady-state results were of interest, a more-efficient solution procedure was developed. Using user-defined DT material properties (density and conductivity) that were a function of temperature yielded identical steady-state results as *FLUENT*'s two-phase routine and were more efficient to run. Both solution procedures model only heat transfer by conduction, and mass conservation is not automatically taken into account. In either modeling method, conservation of DT mass is controlled by a manual iterative process. Knowing the actual total mass of DT in the PFT assembly, the layering sphere's fixed-temperature boundary condition can be adjusted until the desired mass of DT contained in the PFT assembly is obtained.

Figure 146.42 shows the model geometry. The outer portion of the DT physically touching the target capsule shell uses a cell size of 1×1 μm to resolve the gas/ice-phase boundary (shown in Fig. 146.43). Other areas of the model use a coarser mesh for a more-efficient solution. Based on a mesh refinement study, the results presented are mesh independent. Thermal conductivities at ~20 K are 0.0255, 0.009, 0.35, 0.05, 0.333, 0.15, 0.15, and 59 W/m/K for He (Ref. 11), DT gas,[12] DT solid,[12] GDP plastic shell,[13] Stycast 1266 (Ref. 14), fused silica,[15] borosilicate glass,[15] and beryllium,[16] respectively. Densities are 0.0065, 0.7, 260, 1420, 1120, 2640, 2640, and 1851 kg/m^3 for He, DT gas, DT solid, GDP plastic shell, Stycast 1266, fused silica, borosilicate glass, and beryllium, respectively. A user-defined function (UDF) was used for the 200-W/kg decay heat of DT (Ref. 13). (Note: Borosilicate glass conductivity was used for fused silica and polyimide conductivity was used for the GDP capsule because of the lack of cryogenic material property data.)

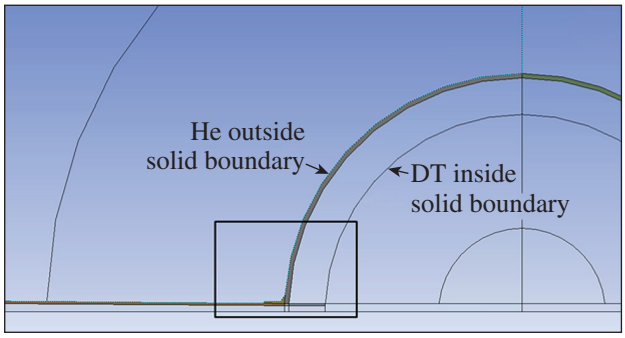

Figure 146.42
Model geometry near the target capsule.

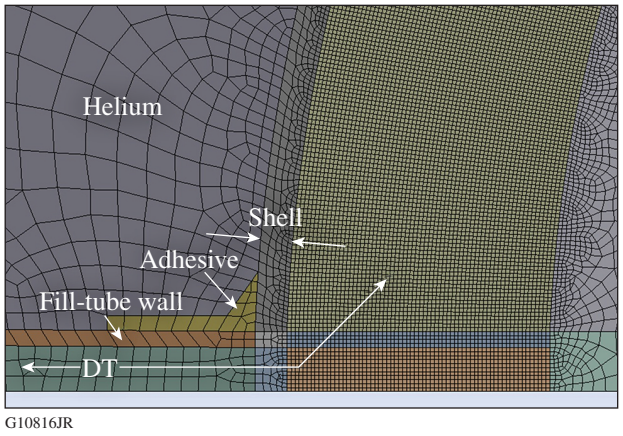

Figure 146.43
Image of the fine mesh required to resolve the solid/gas phase boundary near the target capsule.

Figure 146.44 shows temperature contours predicted by the model. The temperature is hottest at the center of the target (radioactive decay) and coldest at the isothermal boundary condition representing the copper layering sphere. Figure 146.45 illustrates the resulting solid/gas phase boundary predicted by the model (DT ice is shown in red). Figure 146.46 is an unwrapped image of the model ice thickness overlaid on the measured ice thickness of the layer in the experimental PFT target; the fill tube is located at ~50°. The model thickness profile is very similar to experimental results. One difference is that the actual ice layer shows a thick spot in the ice above the hole in the layering sphere (required to insert the target

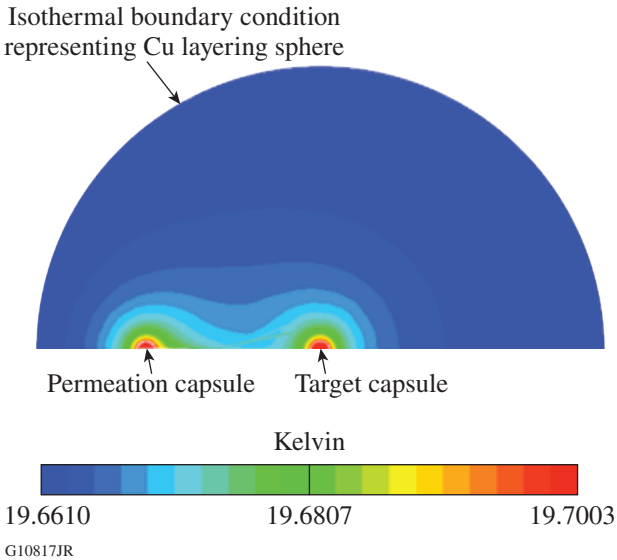

Figure 146.44
Modeled temperature contours of the target and copper layering sphere.

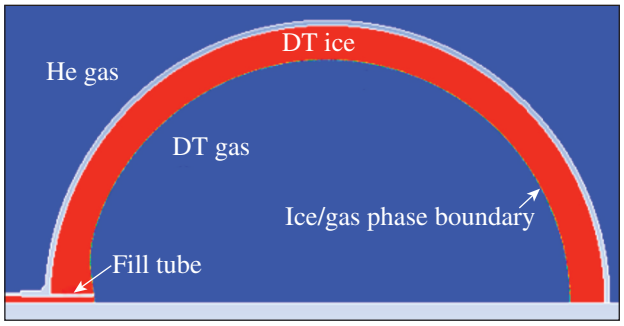

Figure 146.45
The ice/gas phase boundary predicted by the model (DT ice is shown in red).

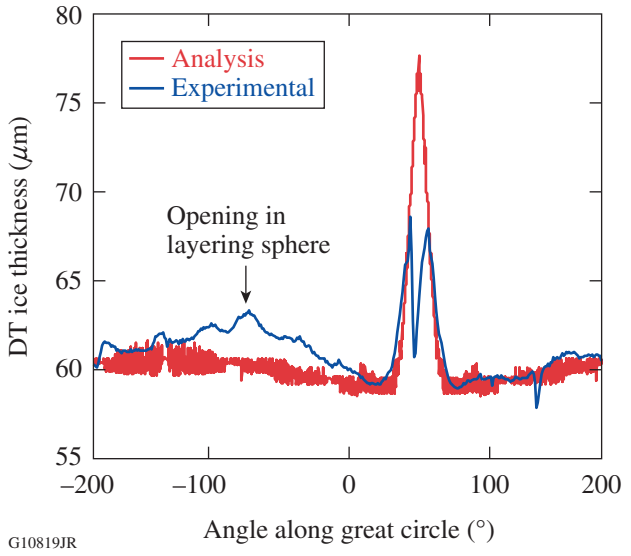

Figure 146.46
Unwrapped image of the model prediction of ice thickness overlaid on actual ice thickness; the fill tube is located at ~50°.

into the layering sphere). The hole cannot be modeled since the axis for the axisymmetric model is aligned with the fill tube. The thermal model estimates the peak thickness variation to be ~17 μm near the fill tube, and the effect of the fill tube is apparent ~±20° on either side. The model accurately predicts the uniformity of the actual ice-layer thickness. This verifies the modeling methodology so good estimates of ice uniformity for other ICF target designs can be made numerically.

The nonuniformity in the ice thickness near the fill tube for the target design discussed above is too large for high-yield ICF implosions. Three critical design parameters affecting this nonuniformity are (1) the fill tube's size, (2) the target shell's thermal conductivity, and (3) the fill tube's thermal conductivity. The decay heat from the target is conducted (radially) away from the target shell. Nonuniformities in this conduction path distort the isotherms, resulting in ice-thickness nonuniformity. If the isotherms were perfectly concentric about the target shell, the ice thickness would be uniform. The thermal conductivity of borosilicate glass is ~6× higher than helium, causing a cold spot near the fill tube that results in locally thicker ice. Minimizing the borosilicate glass cross-sectional area or its thermal conductivity will minimize this effect. Less obvious is the effect of shell conductivity on ice-thickness uniformity. The fill-tube causes temperature variations in the θ direction in the axisymmetric model, resulting in nonconcentric isotherms. When the shell has high thermal conductivity, it "short circuits" the θ temperature variations, resulting in more-concentric isotherms.

Here we use the model to quantify the effect of alternate target designs on ice-layer nonuniformities near the fill tube. First we investigate the effect of a fill tube's cross-sectional area on the ice-thickness uniformity near the fill tube. The effect of borosilicate fill-tube size on ice-thickness uniformity with a GDP (low thermal conductivity of 0.05 W/m/K) shell is shown in Fig. 146.47. The fill-tube size has a significant effect on variations in ice-layer thickness near the fill tube. The variation decreases from ~30% for the 30-μm-OD fill tube to ~10% for the 10-μm-OD fill tube.

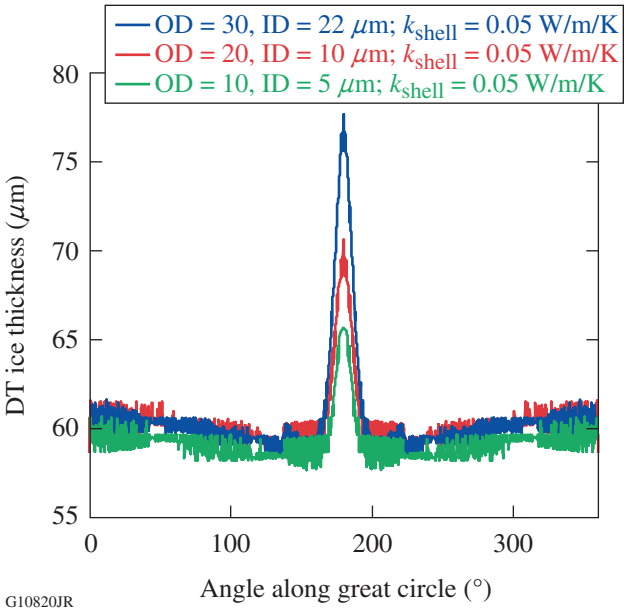

Figure 146.47
Unwrapped image of the model prediction of ice thickness for three different fill-tube cross sections with a GDP shell having a thermal conductivity of 0.05 W/m/K.

The effect of the shell's thermal conductivity for a 20-μm-OD, 10-μm-ID borosilicate fill tube with 20 μm of penetration into the shell is shown in Fig. 146.48. The shell's thermal conductivity has a significant effect on variations in ice-layer thickness near the fill tube. Bulk beryllium at ~20 K has a thermal conductivity of ~59 W/m/K. If a target shell has a thermal conductivity approaching that of bulk beryllium, it would almost completely negate the ice-thickness variations near the fill tube.

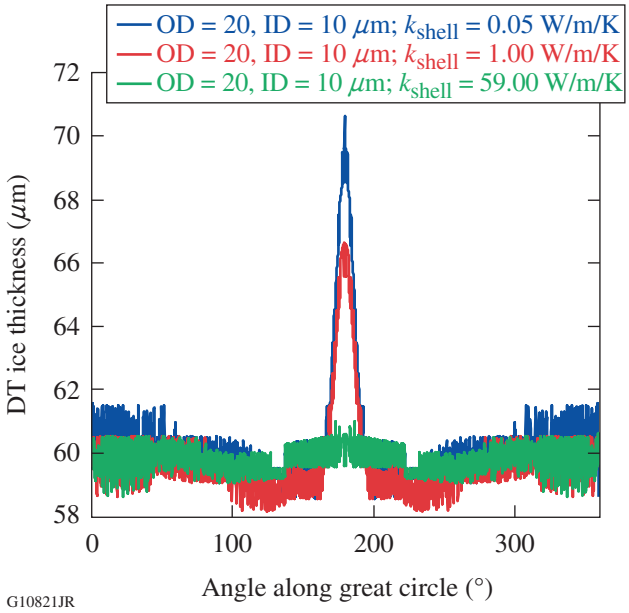

Figure 146.48
Unwrapped image of the model prediction of ice thickness for three different shell thermal conductivities with a 20-μm OD, 10-μm ID borosilicate fill tube.

Conclusions

An ICF target has been successfully filled and a <1-μm-rms DT ice layer has been developed using a novel fill design that combines attributes of permeation and fill-tube filling. This new filling method allows LLE to immediately begin the study of nonpermeable cryogenic target capsules with their current infrastructure. A numerical model has been presented that accurately predicts the ice nonuniformities near the fill tube as seen in empirical data. Using this model, target designs with better ice-thickness uniformity have been proposed. One key but less obvious factor that improves ice uniformity is the target shell's conductivity. Numerical simulations show that high-conductivity shells (e.g., shells with the conductivity of bulk beryllium at ~20 K, 59 W/m/K) completely negate the fill-tube–induced ice nonuniformities.

ACKNOWLEDGMENT

This material is based upon work supported by the Department of Energy National Nuclear Security Administration under Award Number DE-NA0001944, the University of Rochester, and the New York State Energy Research and Development Authority. The support of DOE does not constitute an endorsement by DOE of the views expressed in this article.

REFERENCES

1. J. Nuckolls *et al.*, Nature **239**, 139 (1972).
2. R. L. McCrory, D. D. Meyerhofer, R. Betti, R. S. Craxton, J. A. Delettrez, D. H. Edgell, V. Yu. Glebov, V. N. Goncharov, D. R. Harding, D. W. Jacobs-Perkins, J. P. Knauer, F. J. Marshall, P. W. McKenty, P. B. Radha, S. P. Regan, T. C. Sangster, W. Seka, R. W. Short, S. Skupsky, V. A. Smalyuk, J. M. Soures, C. Stoeckl, B. Yaakobi, D. Shvarts, J. A. Frenje, C. K. Li, R. D. Petrasso, and F. H. Séguin, Phys. Plasmas **15**, 055503 (2008).
3. J. D. Lindl, Phys. Plasmas **2**, 3933 (1995).
4. D. E. Solomon and T. M. Henderson, J. Phys. D: Appl. Phys. **8**, L85 (1975).
5. S. O. Kucheyev and A. V. Hamza, J. Appl. Phys. **108**, 091101 (2010).
6. *LLE Review Quarterly Report* **81**, 6, Laboratory for Laser Energetics, University of Rochester, Rochester, NY, LLE Document No. DOE/SF/19460-335 (1999).
7. A. Nikroo *et al.*, General Atomics, San Diego, CA, Report GA–A23881 (2002).
8. A. J. MacKinnon, N. B. Meezan, J. S. Ross, S. Le Pape, L. Berzak Hopkins, L. Divol, D. Ho, J. Milovich, A. Pak, J. Ralph, T. Döppner, P. K. Patel, C. Thomas, R. Tommasini, S. Haan, A. G. MacPhee, J. McNaney, J. Caggiano, R. Hatarik, R. Bionta, T. Ma, B. Spears, J. R. Rygg, L. R. Benedetti, R. P. J. Town, D. K. Bradley, E. L. Dewald, D. Fittinghoff, O. S. Jones, H. R. Robey, J. D. Moody, S. Khan, D. A. Callahan, A. Hamza, J. Biener, P. M. Celliers, D. G. Braun, D. J. Erskine, S. T. Prisbrey, R. J. Wallace, B. Kozioziemski, R. Dylla-Spears, J. Sater, G. Collins, E. Storm, W. Hsing, O. Landen, J. L. Atherton, J. D. Lindl, M. J. Edwards, J. A. Frenje, M. Gatu-Johnson, C. K. Li, R. Petrasso, H. Rinderknecht, M. Rosenberg, F. H. Séguin, A. Zylstra, J. P. Knauer, G. Grim, N. Guler, F. Merrill, R. Olson, G. A. Kyrala, J. D. Kilkenny, A. Nikroo, K. Moreno, D. E. Hoover, C. Wild, and E. Werner, Phys. Plasmas **21**, 056318 (2014).
9. D. H. Edgell, W. Seka, R. S. Craxton, L. M. Elasky, D. R. Harding, R. L. Keck, M. Pandina, M. D. Wittman, and A. Warrick, presented at the 46th Annual Meeting of the Division of Plasma Physics, Savannah, GA, 15–19 November 2004.
10. T. C. Sangster, R. Betti, R. S. Craxton, J. A. Delettrez, D. H. Edgell, L. M. Elasky, V. Yu. Glebov, V. N. Goncharov, D. R. Harding, D. Jacobs-Perkins, R. Janezic, R. L. Keck, J. P. Knauer, S. J. Loucks, L. D. Lund, F. J. Marshall, R. L. McCrory, P. W. McKenty, D. D. Meyerhofer, P. B. Radha, S. P. Regan, W. Seka, W. T. Shmayda, S. Skupsky, V. A. Smalyuk, J. M. Soures, C. Stoeckl, B. Yaakobi, J. A. Frenje, C. K. Li, R. D. Petrasso, F. H. Séguin, J. D. Moody, J. A. Atherton, B. D. MacGowan, J. D. Kilkenny, T. P. Bernat, and D. S. Montgomery, Phys. Plasmas **14**, 058101 (2007).

11. N. B. Vargaftik *et al*., *Handbook of Thermal Conductivity of Liquid Gases* (CRC Press, Boca Raton, FL, 1994)

12. P. C. Souers, *Hydrogen Properties for Fusion Energy* (University of California Press, Berkeley, CA, 1986).

13. Material Properties: Polyimide (Kapton), http://cryogenics.nist.gov/MPropsMAY/Polyimide%20Kapton/PolyimideKapton_rev.htm (24 May 2016).

14. S. Laumann *et al*., J. Mater. Res. **26**, 1861 (2011).

15. Thermal and Mechanical Properties of Glass (Quartz, Pyrex, Borosilicate), http://www.yutopian.com/Yuan/prop/Glass.html (24 May 2016).

16. Be Properties, https://www.bnl.gov/magnets/staff/gupta/cryogenic-data-handbook/Section7.pdf (24 May 2016).

Acidic Magnetorheological Finishing of Infrared Polycrystalline Materials

Introduction

Magnetorheological finishing (MRF) is a polishing technique used to produce high-precision optics. It is known for its relatively high material-removal rate (mrr);[1] subnanometer surface roughness on various materials, especially glass;[2–4] good figure/shape accuracy;[5] deterministic nature;[1] and the ability to polish complex shapes at a large size range.[6] For some materials, however, the conventional alkaline water-based magnetorheological (MR) fluid tends to leave noticeable artifacts and a relatively high roughness on the surface;[7–10] e.g., Jacobs *et al.*[7] talked about the difficulties in using a conventional MR fluid to polish calcium fluoride (CaF_2) and potassium dihydrogen phosphate (KDP). It was shown that since CaF_2 is a soft material [H_V = 1.65 GPa (Ref. 11)], it is easily chipped and tends to experience a large number of fine scratches. On the other hand, KDP is particularly soluble in water; therefore, any water-based MR fluid is not recommended when polishing this material. The alternative MR fluid for finishing CaF_2 was based on a lubricant component (PEG 200) instead of water to soften the MR fluid and prevent fine scratches. The magnetic-field strength on the MRF machine was also reduced to further soften the MR fluid. The results showed a root-mean-square (rms) surface roughness of ~1 nm for this material. For KDP, the water component was replaced with dicarboxylic acid ester. Surface-roughness results (when using nanodiamond as a polishing abrasive) were as low as ~20-nm peak-to-valley (p–v) and ~1.6-nm rms. Similarly, Menapace *et al.*[12] [Lawrence Livermore National Laboratory (LLNL)] successfully polished a 50 × 50-mm^2 KDP substrate using an optimized nonaqueous MR fluid. The surface microroughness achieved was in the mid-angstrom level, along with a 5× improvement in the surface figure. More recently, Pattanaik *et al.*[13] described the use of an MRF setup for polishing a nonmagnetic copper substrate using an oil-based MR fluid. By modifying both the MR fluid composition [mainly the concentration of carbonyl iron (CI), a polishing abrasive, and an oil-based medium] and the experimental setup (relative rotational movement between the workpiece and MR fluid), they found the optimal conditions at which a smooth surface roughness is achieved.

Another group of materials that is relatively challenging to finish by using MRF [and other techniques (see Refs. 14–16)] consists of crystalline[8,17] and polycrystalline materials.[9,10,18] The difficulty arises because of the material anisotropy in the unit cell regime (mostly found at the less-symmetric lattice systems, such as hexagonal) and/or in the grain-array regime.[19–21] Kozhinova *et al.*[9] (and later Hallock *et al.*[10]) demonstrated the use of an altered MR fluid to finish an infrared (IR) polycrystalline material—chemical-vapor–deposited (CVD) ZnS. They showed that when this material is processed with a conventional alkaline MR fluid, surface-artifact phenomena known as "pebbles"[9,22] (in the mesostructured regime) and "orange peel" (in the grain-structure regime)[23] are raised on the finished surface; furthermore, the more material removed by MRF, the rougher the surface. They experimented with the MRF process by using a modified MR fluid in which the CI particles were replaced with a "soft" CI type and the carrier medium was modified from alkaline to acidic. When using this type of modified MR fluid, the surface artifacts and roughness can be minimized.

In our ongoing research, we investigate the role of chemical and mechanical effects on the mrr during MRF of IR polycrystalline materials, with considerable focus on CVD ZnS. Seeking an explanation to Kozhinova's findings, we investigated[19] the anisotropy of ZnS during MRF using four dominant single-crystal orientations of ZnS (100, 110, 111, and 311). The relative mrr's between the different orientations were examined during MRF, using three chemomechanically modified MR fluids: pH 6 with viscosity (η) of ~197 cP, pH 5 with $\eta \approx 117$ cP, and pH 4 with $\eta \approx 47$ cP. We used unique CI particles coated with a thin layer of zirconia to protect the iron particles from rapid corrosion in acidic conditions.[24–26] We found that the minimal variation in the removal rate between the four crystalline orientations was obtained with a pH 4 and low-viscosity (~47-cP) MR fluid. This suggested that during MRF, most of the grains within the polycrystalline material are polished at relatively the same rate (uniformly), leaving a few surface artifacts (pebbles) and a relatively low surface roughness. When this formulation was tested on several CVD ZnS substrates, we found that

pebble artifacts were minimal with this composition; however, surface microroughness was relatively high at ~44-mm rms. The missing part in our previous work[19] was lacking polishing abrasive in the acidic MR fluid. In this article we describe our efforts to further reduce the appearance of pebbles and improve surface roughness on several CVD ZnS substrates and other important IR polycrystalline materials using an acidic, low-viscosity MR fluid. A modified version of zirconia-coated CI particles to further increase the acidic MR fluid's lifespan at pH 4.5 (Refs. 27 and 28) is used. We first examine the effect of two polishing abrasives—alumina and nanodiamond—on the removal-rate uniformity of single-crystal orientations of ZnS and then examine the surface finish of several IR polycrystalline materials that were polished with two acidic, low-viscosity MR fluids containing these two polishing abrasives.

Experimental Details

1. IR Optical Substrates

The crystalline materials and their relevant properties are listed in Table 146.IV. All single-crystal ZnS samples were grown, cut, and supplied by the same supplier.[29] Polycrystalline CVD ZnS materials were obtained from different suppliers, each providing one sample (samples A, B, C, and D in Table 146.IV). Technically the material is listed as CVD ZnS; however, differences are anticipated because of variations in detailed manufacturing conditions with each supplier.[20,30] Also, samples A–C are forward-looking IR (FLIR) ZnS, while sample D is elemental ZnS.

Hot isostatic pressed (HIP) ZnS, CVD ZnSe, and MgF_2 were also provided from different suppliers. All materials were ground and pre-polished in-house, as described in Ref. 9, to a flatness of 1 to 2 λ, a p–v roughness of <40 nm, and an rms of <4 nm.

2. Acidic MR Fluids

The MR fluids we used are based on the "advanced zirconia-coated CI particles." The particles' synthesis and characterization are widely described in Refs. 27 and 28. The use of the coated particles in an acidic suspension greatly improves the MR fluid's lifespan by suppressing oxidation of the carbonyl iron particles. The primary formulation of the acidic MR

Table 146.IV: Characteristics and properties of IR crystalline materials.

Sample ID	Sample Type	Crystal Structure	H_V (GPa)*	Grain Size (μm)
ZnS (100)	Single crystal	Cubic	1.89±0.03 (Ref. 19)	N/A
ZnS (110)	Single crystal	Cubic	1.71±0.04 (Ref. 19)	N/A
ZnS (111)	Single crystal	Cubic	2.93±0.04 (Ref. 19)	N/A
ZnS (311)	Single crystal	Cubic	2.17±0.12 (Ref. 19)	N/A
ZnS A†	Polycrystalline; CVD; FLIR	Cubic	1.86±0.02 (Ref. 28)	1.18±0.34**
ZnS B†	Polycrystalline; CVD; FLIR	Cubic	1.72±0.02 (Ref. 28)	2.03±0.64**
ZnS C‡	Polycrystalline; CVD; FLIR	Cubic	1.61±0.14 (Ref. 28)	—
ZnS D‡	Polycrystalline; CVD; elemental	Cubic	2.00±0.03 (Ref. 28)	1.94±0.46**
HIP ZnS	Polycrystalline; CVD; HIP	Cubic	1.33±0.05 (Ref. 28)	75 to 150 (Ref. 22)
ZnSe	Polycrystalline; CVD	Cubic	0.90±0.06 (Ref. 28)	43±9.00 (Ref. 31)
MgF_2	Polycrystalline	Tetragonal	2.29±0.05 (Ref. 28)	~0.45*** (Ref. 32)

*Taken with a Tukon 300 BM Micro-Indenter at 100-g force for single-crystal samples and 400-g force for all other samples.
**The lineal-intercept method for determining average grain size was used.
***An image-analyzing software was used.
†From U.S. vendors
‡From Chinese vendors

fluid, given in Table 146.V, was blended off-line using a shaft mixer. Small portions of powder were incrementally added to a mixture of water and a particle-dispersant agent [polyethylene-imine (PEI), Sigma Aldrich] to form a slurry. The acid (glacial acetic acid, Sigma Aldrich) was added last. Polishing abrasives—alumina and diamond (see Table 146.VI for more details)—were added (to separate fluids) at a different stage of the experiment, when the fluids were circulating on the MRF machine. This had no effect on the fluids' viscosity or pH value. For the alumina-based MR fluid, the abrasive concentrations evaluated, in volume percent (vol %), were 0 vol %, 1 vol %, 2 vol %, and 3 vol %. For the nanodiamond-based MR fluid, the abrasive concentrations evaluated were 0 vol %, 0.06 vol %, 0.12 vol %, and 0.18 vol %. Note that the diamond-abrasive concentration is one order of magnitude lower than that of alumina because the nanodiamond abrasive is more aggressive than alumina. The acidic MR fluids had an off-line viscosity of ~45 cP. The pH of the fluids throughout the experiments was 4.53±0.09 and 4.54±0.11 for the alumina and diamond-based fluids, respectively. One liter from each fluid was prepared and loaded on the MRF machine.

Table 146.V: Acidic MR-fluid formulation showing the different components, their original form of supply, and their relative portion in the fluid (in volume percent).

Component	Form of Supply	MR Fluid (vol %)
Advanced zirconia-coated CI particles	Powder	27.97
DI (de-ionized) water	Liquid	49.30
Polyethylene-imine	50 wt% in water	20.71
Acetic acid	~16-M solution	2.02

3. MRF Spotting Experiment

An MRF spotting experiment was conducted on a research MRF machine, referred to as the "spot-taking machine" (STM).[7] The STM has features similar to a conventional MRF machine; however, it is not designed to perform a full run of polishing. It is capable of taking single spots at a time because of a lack of part movement. An example of an MRF spot and the removal function is shown in Fig. 146.49. The acidic MR fluids (containing different abrasive types and concentrations) were used in a screening spotting experiment on single-crystal orientations of ZnS. Each single-crystal substrate was spotted twice with a given acidic fluid for 1 min. The peak removal rate (prr) was then measured. Following the screening experiment with single-crystal ZnS, the fluids with the highest abrasive concentration (i.e., 3 vol% alumina and 0.18 vol% diamond) were used in the second spotting stage of polycrystalline IR materials. Each polycrystalline substrate was spotted once for 15 min to remove between 0.7 to 1.0 μm of material at the deepest depth of penetration (ddp). The spotting time was chosen

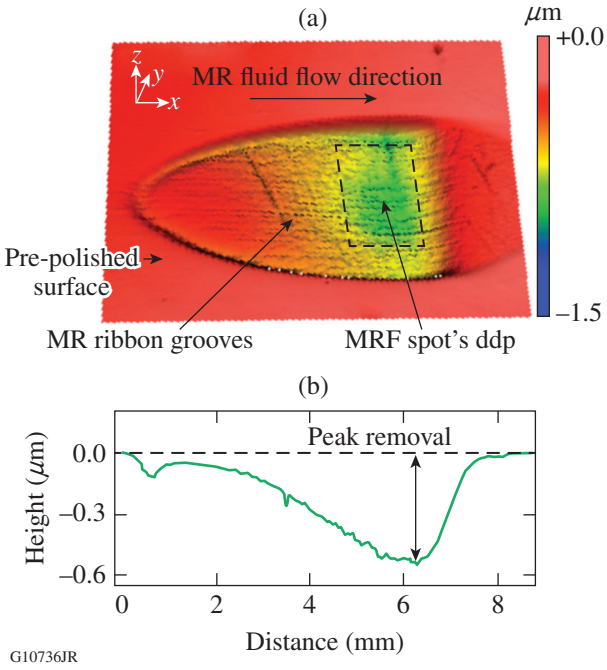

Figure 146.49
(a) A 3-D white-light interferometer image (12 × 8 mm^2) of a magnetorheological finishing (MRF) spot taken on a pre-polished chemical-vapor–deposited (CVD) ZnS substrate (sample A) designating the spot's depth of deepest penetration (ddp), MR ribbon grooves, and MR fluid-flow direction. (b) The MRF removal function shows the peak removal around the spot's ddp.

Table 146.VI: Polishing abrasives, their source, and characteristics.

Polishing Abrasive	Source	Form of Supply	Particle Size* (nm)
Alumina (alpha)	NanoTek	Dry powder	d_{15} = 19; d_{50} = 52; d_{80} = 169
DIANAN® nanodiamond	Straus Chemical	Dry powder	d_{15} = 13; d_{50} = 28; d_{80} = 143

*Particle-sized data were obtained with the AcoustoSizer IIS-Particle size and zeta potential analyzer.[33] Samples contained 0.5 wt% of abrasive in DI water. All suspensions were dispersed using a sonication bath for 20 min prior to measurement.

based on Ref. 9, which states that pebbles on a pre-polished CVD ZnS surface are exposed after ~0.5 μm of material has been removed. Machine settings were 1.3-mm ribbon height, 0.2-mm (for single crystals) and 0.3-mm (for polycrystalline) penetration depth, 220-rpm wheel speed, 110-rpm pump speed, and a 15-A electric current.

4. Metrology

a. Material removal rate of single-crystal ZnS substrates. Peak removal rates for all spots taken on the single-crystal substrates were obtained with a Zygo Mark IV laser interferometer[34] by subtracting the spotted area from the original surface and dividing the difference by the spotting time, i.e., 1 min. The peak removal is measured as the deepest vertical depth of material removed by MRF (see Fig.146.49).

b. Surface artifacts and microroughness of polycrystalline materials. The submillimeter- and millimeter-sized pebbles on the spotted polycrystalline materials, which are a direct result of the CVD growth technique,[9,22,35,36] were evaluated using a Zygo white-light, non-contact interferometer—the NewView™ 100 (Ref. 37). A 5× objective (with a 1.39 × 1.04-mm^2 field of view) was used to capture two areal-roughness measurements at the ddp of the spots. These measurements were analyzed, using a low-pass filter option in MetroPro, to screen out the roughness and leave only the surface waviness.[38] An example of a low-pass filtered measurement is given in Figs. 146.50(a)–146.50(c), where (a) the original measurement is decomposed to (b) a waviness plot and (c) a roughness plot. The waviness data provide an indication on the pebbles' severity on the surface. Surface microroughness, which captures submicron- and micron-sized features, such as pits, scratches, and grain boundaries (known as orange peel[23]), was measured using the NewView 100™ with a 20× objective (a 0.35 × 0.26-mm^2 field of view). Four areal measurements were taken at the ddp of each spot. Within each areal measurement, five lineout scans were collected in the direction of the MR fluid flow. This helps to avoid the grooves created by the MR ribbon during MRF (see Fig. 146.49), which are a direct result of the workpiece being stationary and not rotating on the STM. We believe that the lineout data better reflect the roughness one would obtain if a conventional MRF machine with a full run would have been used. All p–v and rms-roughness data were averaged and are presented in Tables 146.VII and 146.VIII for CVD ZnS and Tables 146.IX and 146.X for the other IR materials.

Results

1. Material Removal Rate of Single-Crystal ZnS

The average prr for all four single-crystal ZnS substrates finished with various amounts of alumina and diamond abrasives in the acidic MR fluids is given in Table 146.VII and Figs. 146.51(a) and 146.51(b). Both sources indicate that the addition of abrasives increased the overall prr of the acidic fluids. When alumina was first added to the acidic fluid, the average prr of all four orientations increased by ~59%—from ~0.029 μm/min to ~0.046 μm/min (see the highlighted line in Table 146.VII); when diamonds were first added to the acidic fluid, the average increased by ~46%—from ~0.026 μm/min to ~0.038 μm/min. For the acidic fluids with alumina, an additional amount of abrasive has no real effect on the prr. Observation of the data within the standard deviation shows little change in the average prr with increased abrasive concentration after the first dose is added [Fig. 146.51(a)]. For the acidic fluid containing the diamonds, however, an additional amount of abrasive linearly increases the average prr of the fluid [Fig. 146.51(b)]. The highest average prr of the fluid is achieved when 3× the amount of diamond abrasive is used—i.e., 0.18 vol %.

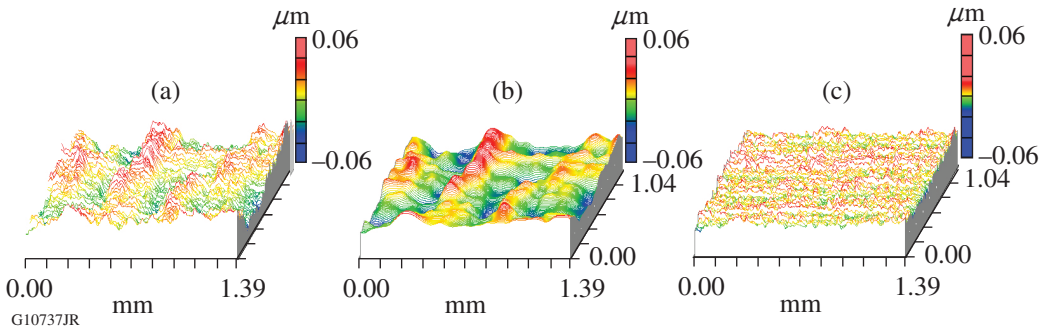

Figure 146.50
A set of 3-D white-light interferometer images (1.39 × 1.04 mm^2) of a CVD ZnS (sample A) substrate finished with a conventional alkaline MR fluid. (a) Original measurement showing both surface waviness and roughness, (b) low-pass filter analysis showing surface waviness (indication of pebbles), and (c) screened-out high-frequency roughness.

Table 146.VII: Average peak removal rate (μm/min) for single-crystal substrates of ZnS finished with acidic MR fluids that contain various amounts of alumina and nanodiamond abrasives. Note that the alumina-abrasive concentration is an order of magnitude higher than the nanodiamond.

Single-Crystal Orientation	Acidic MR Fluid with Alumina Abrasive				Acidic MR Fluid with Nanodiamond Abrasive			
	0 vol %	1 vol %	2 vol %	3 vol %	0 vol %	0.06 vol %	0.12 vol %	0.18 vol%
100	0.030±0.002	0.045±0.001	0.040±0.001	0.041±0.000	0.029±0.000	0.035±0.000	0.046±0.007	0.053±0.001
110	0.028±0.000	0.046±0.004	0.048±0.002	0.039±0.000	0.029±0.002	0.043±0.003	0.050±0.003	0.056±0.004
111	0.032±0.003	0.045±0.000	0.049±0.003	0.041±0.002	0.020±0.002	0.036±0.008	0.046±0.003	0.051±0.005
311	0.028±0.001	0.048±0.002	0.040±0.003	0.045±0.002	0.025±0.001	0.037±0.001	0.040±0.007	0.053±0.000
Average	0.029±0.002	0.046±0.001	0.044±0.005	0.042±0.002	0.026±0.004	0.038±0.004	0.046±0.004	0.053±0.002

Table 146.VIII: Surface waviness as p–v and rms collected with a 5× objective at the spots' ddp of four polycrystalline, CVD ZnS substrates provided by different suppliers. Data were obtained using a low-pass filter.

CVD ZnS Sample ID	Acidic MR Fluid with Alumina Abrasive			Acidic MR Fluid with Nanodiamond Abrasive		
	ddp (μm); removal rate (μm/min)	p–v (nm)	rms (nm)	ddp (μm); removal rate (μm/min)	p–v (nm)	rms (nm)
Sample A	0.76; 0.051	62.26±33.02	7.06±1.76	0.95; 0.063	64.51±1.31	9.24±0.86
Sample B	0.77; 0.051	54.83±13.33	7.22±1.34	0.84; 0.056	47.29±0.48	5.51±0.22
Sample C	0.69; 0.046	194.67±42.24	24.14±0.82	1.10; 0.073	55.47±.91	7.35±1.76
Sample D	0.79; 0.053	147.85±1.91	16.43±0.72	0.94; 0.063	71.46±12.43	7.81±2.34

Table 146.IX: Surface microroughness as areal and lineout p–v and rms collected with a 20× objective at the spots' ddp of four polycrystalline, CVD ZnS substrates provided by different suppliers.

Sample	Acidic MR Fluid with Alumina Abrasive				Acidic MR Fluid with Nanodiamond Abrasive			
	Areal		Lineouts		Areal		Lineouts	
	p–v (nm)	rms (nm)	p–v (nm)	rms (nm)	p–v (nm)	rms (nm)	p–v (nm)	rms (nm)
A	694.23±8.10	18.53±1.58	75.70±7.88	14.22±1.35	1361.11±147.15	14.33±1.01	28.46±4.54	6.10±1.24
B	694.68±25.87	20.38±1.79	79.39±15.19	15.58±2.75	775.50±285.04	10.32±2.54	27.66±4.38	5.93±0.76
C	903.72±110.06	39.48±1.80	111.67±52.06	29.83±4.47	1364.06±53.33	26.94±1.70	32.87±7.58	7.79±1.98
D	1160.39±343.47	36.08±4.74	136.03±20.64	28.39±4.32	1215.28±138.67	18.35±2.91	30.08±4.26	6.94±0.85

Table 146.X: Surface waviness as p–v and rms, collected with a 5× objective at the spots' ddp of three polycrystalline IR substrates. Data were obtained using a low-pass filter.

Sample	Acidic MR Fluid with Alumina Abrasive		Acidic MR Fluid with Nanodiamond Abrasive	
	p–v (nm)	rms (nm)	p–v (nm)	rms (nm)
HIP ZnS	331.37±84.21	58.52±14.01	379.21±13.35	58.35±3.04
ZnSe	377.94±21.65	53.06±0.71	236.33±83.42	29.31±6.67
MgF_2	45.69±8.01	5.76±1.33	9.81±0.75	4.84±4.15

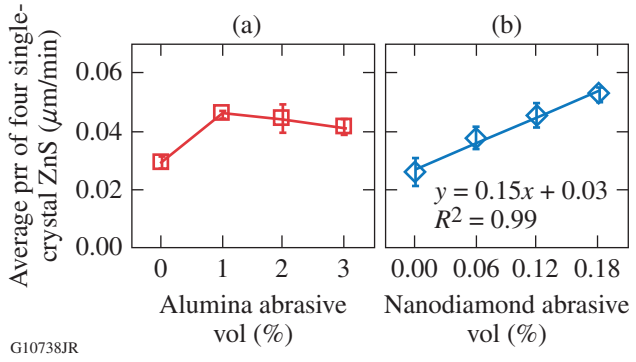

Figure 146.51
Average peak removal rate (prr) of all four single-crystal orientations versus abrasive concentration in the acidic MR fluid. (a) Alumina-based acidic MR fluid and (b) nanodiamond-based acidic MR fluid. Note that the alumina-abrasive concentration is ~10× higher than that of the nanodiamond abrasive.

For the next stage of the experiment—MRF of polycrystalline IR substrates—acidic formulations that contained the maximum amount of alumina and nanodiamond abrasives were used (i.e., a concentration of 3 vol % of alumina and 0.18 vol % of nanodiamonds).

2. Surface Finish of Polycrystalline CVD ZnS

The surface finish at the spots' ddp for all CVD ZnS samples (A–D) measured with 5× and 20× objectives is shown in Tables 146.VIII and 146.IX, respectively. Pebbles were studied using data from Table 146.VIII representing surface waviness (original roughness data are provided in **Appendix A**, p. 107). Surface microroughness was studied using data from Table 146.IX. Table 146.VIII indicates that the alumina-based acidic MR fluid produced less waviness on the surface of samples A and B than on samples C and D, in which the waviness was ~50% higher. When the samples were finished with a nanodiamond-based acidic MR fluid, similar surface waviness was observed for samples A and B. For samples C and D, however, the level of waviness is closer in value to that of samples A and B. Surface microroughness data in Table 146.IX show a similar trend to what was seen with surface waviness. When finished with an alumina-based acidic MR fluid, the microroughness of samples A and B was similar; the microroughness of samples C and D was similar, but ~40% higher than that of samples A and B. When the samples were finished with a nanodiamond-based acidic MR fluid, all samples showed a remarkable surface microroughness as a lineout of ~30-nm p–v and ~6-nm rms, and the large difference in roughness among samples A–D was diminished. A power spectral density (PSD) analysis of samples A–D, given in Fig. 146.52, also shows that MRF using the nanodiamond-based acidic MR fluid resulted in less pebbles on the surface and improved surface microroughness. At a spatial frequency below 100 mm^{-1} (corresponding to a lateral distance of 0.1 mm and higher), all CVD ZnS samples show a flatter and lower power density (PD) trend line. This indicates a reduction in pebbles on the surfaces that are finished with an acidic MR fluid containing nanodiamonds. At a spatial frequency above 100 mm^{-1} (a range that represents microroughness), samples A and B reach the lowest PD value, indicating that their microroughness is lower compared to samples C and D. Overall, the PSD results support the waviness and roughness analyses presented in Tables 146.VIII and 146.IX.

White-light interferometer micrographs taken with a 20× objective (given in Figs. 146.53 and 146.54) show the different

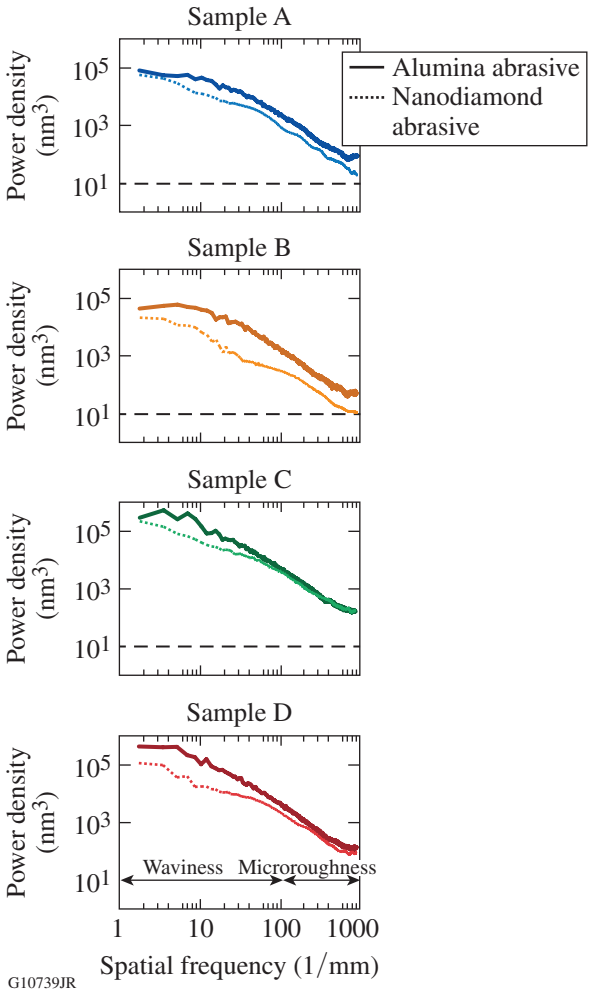

Figure 146.52
Power spectral density (PSD) for CVD ZnS samples A–D. The solid curves designate an acidic MR fluid with an alumina abrasive; the dotted curves designate acidic MR fluid with a nanodiamond abrasive.

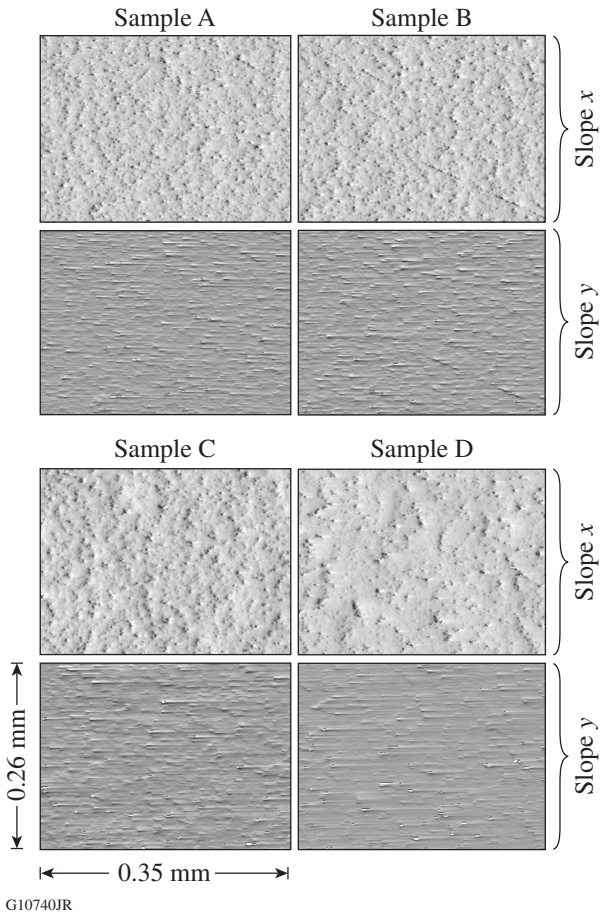

Figure 146.53
White-light interferometer (Zygo NewView™ 100) micrographs (20× objective; 0.35 × 0.26 mm^2) at the ddp of CVD ZnS samples A–D finished with an acidic MR fluid containing an alumina abrasive. The top micrographs designate "slope *x* surface maps;" the bottom micrographs designate "slope *y* surface maps." Pits on the surface (seen in the *x* slope maps) correspond to MR ribbon grooves (seen in the *y* slope maps) in the direction of the MR fluid flow.

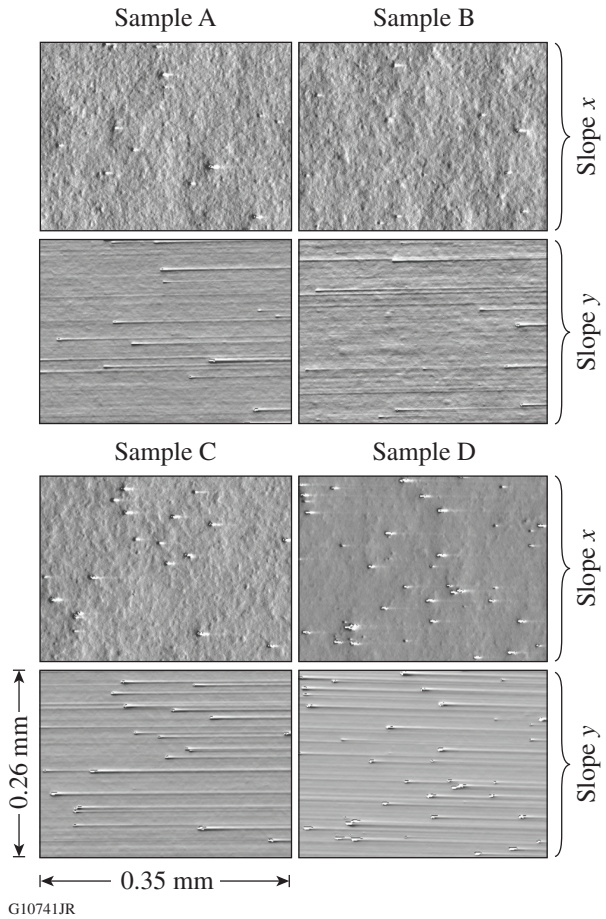

Figure 146.54
White-light interferometer (Zygo NewView™ 100) micrographs (20× objective; 0.35 × 0.26 mm^2) at the ddp of CVD ZnS samples A–D finished with an acidic MR fluid containing a nanodiamond abrasive. The top micrographs designate "slope *x* surface maps;" the bottom micrographs designate "slope *y* surface maps." Pits on the surface (seen in the *x* slope maps) correspond to MR ribbon grooves (seen in the *y* slope maps) in the direction of the MR fluid flow.

textures on surfaces finished with the two acidic MR fluids. For the alumina-based MR fluid (Fig. 146.53), a pitted pattern appears on all CVD ZnS samples (A–D). These pits seem to be a result of the grooves created by the MR ribbon in the direction of the MR fluid flow ("slope *y* surface map" micrographs in Fig. 146.53). A similar observation was found when nanodiamonds were used in the acidic MR fluid. In this case, however, the amount of pits and grooves is significantly lower, especially for samples A and B.

3. Surface Finish of Other Polycrystalline IR Optical Materials

The two acidic MR fluids used with polycrystalline, CVD ZnS substrates A–D, described in **Surface Finish of Polycrystalline CVD ZnS** (p. 103), were also used on CVD HIP ZnS, CVD ZnS, and MgF_2—which is not a CVD-grown material. Tables 146.X and 146.XI show the surface waviness and surface microroughness, respectively, of these materials (original data collected with a 5× objective are given in **Appendix A**, p. 107). Table 146.X indicates that CVD HIP ZnS and CVD ZnSe share similar values of waviness when finished with alumina-based acidic MR fluid. The pebbles on the surfaces are of the same order of magnitude. No change is seen in the emergence and size of pebbles on the CVD HIP ZnS surface when using nanodiamond abrasives instead of alumina in the acidic fluid. The surface waviness of CVD ZnSe, however, improves by ~40% when using a nanodiamond abrasive in the acidic MR fluid, indicating a reduction in the appearance of pebbles on the sur-

Table 146.XI: Surface microroughness as areal and lineout p–v and rms collected with a 20× objective at the spots' ddp of three polycrystalline IR substrates.

Sample	Acidic MR Fluid with Alumina Abrasive				Acidic MR Fluid with Nanodiamond Abrasive			
	Areal		Lineout		Areal		Lineout	
	p–v (nm)	rms (nm)	p–v (nm)	rms (nm)	p–v (nm)	rms (nm)	p–v (nm)	rms (nm)
HIP ZnS	1180.68±158.00	47.48±8.72	160.62±31.7	36.39±9.56	1476.20±251.10	58.80±15.90	191.30±57.67	54.30±20.60
ZnSe	1734.16±230.39	81.49±9.57	193.55±38.2	46.37±9.77	2270.10±351.85	66.80±8.31	87.39±26.31	21.20±5.72
MgF_2	554.91±142.89	7.72±0.72	38.81±5.881	6.68±0.75	43.54±12.72	1.32±0.13	6.06±0.92	1.09±0.18

face. Magnesium fluoride does not experience the pebble-like structure seen in CVD-grown materials. However, an ~80% improvement is seen in p–v and rms values of this material when using the acidic MR fluid with nanodiamond abrasives.

Surface microroughness results seen in Table 146.XI show that better surface roughness for the CVD HIP ZnS surface was obtained when an alumina abrasive was used in the acidic MR fluid. This is also seen in Figs. 146.55 and 146.56, in which the substrate's roughness is somewhat less pronounced and defined in Fig. 146.55 than in Fig. 146.56. When avoiding the MR ribbon grooves by taking roughness measurements as lineouts (see "Lineout" columns in Table 146.XI), a remarkable reduction in the p–v and rms values is observed. Overall, the alumina-based MR fluid provided better surface roughness for HIP CVD ZnS than the nanodiamond-based fluid.

The microroughness of CVD ZnSe finished with the acidic MR fluid and alumina abrasive is relatively high. A significant reduction in surface roughness, however, was found when this material was finished with nanodiamonds in the MR fluid.

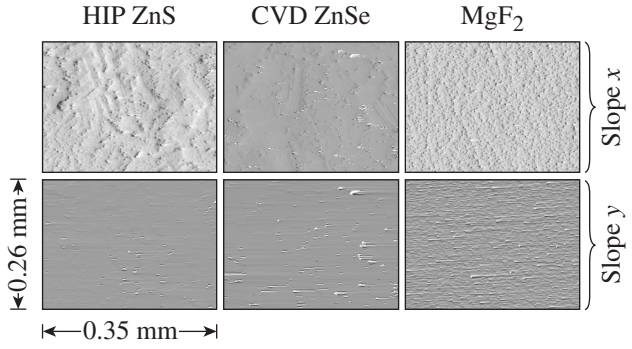

Figure 146.55
White-light interferometer (Zygo NewView™ 100) micrographs (20× objective; 0.35 × 0.26 mm^2) at the ddp of CVD HIP ZnS, CVD ZnSe, and MgF_2 finished with an acidic MR fluid containing an alumina abrasive. Pits on the surface (seen in the *x* slope maps) correspond to MR ribbon grooves (seen in the *y* slope maps) in the direction of the MR fluid flow.

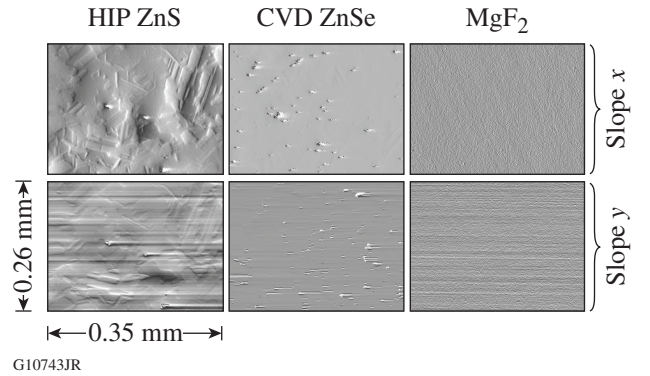

Figure 146.56
White-light interferometer (Zygo NewView™ 100) micrographs (20× objective; 0.35 × 0.26 mm^2) at the ddp of CVD HIP ZnS, CVD ZnSe, and MgF_2 finished with an acidic MR fluid containing a nanodiamond abrasive. Pits on the surface (seen in the *x* slope maps) correspond to MR ribbon grooves (seen in the *y* slope maps) in the direction of the MR fluid flow.

Figure 146.56 demonstrates the diminished small-scale pebbles on the surface of a CVD ZnSe substrate finished with an acidic MR fluid containing nanodiamonds. PSD data (Fig. 146.57) show similar observations. The power-density versus spatial-density plot of the surface finished with nanodiamonds shows significantly lower values than the alumina abrasive, indicating a reduction in the surface roughness (and pebbles) on the surface. For the MgF_2 substrate, finishing this material with an acidic MR fluid containing alumina provided a relatively good surface roughness (~38-nm p–v and ~7-nm rms as lineout). Roughness was significantly improved by more than 80% when using fluid containing nanodiamonds (~7-nm p–v and ~1-nm rms as lineout), with similar improvements in PSD results for this material obtained with the acidic MR fluid containing nanodiamonds being substantially better than that of an alumina-based MR fluid.

Discussion

Adding polishing abrasives to the acidic MR fluid increased the overall material removal rate of the fluid, while maintaining relatively good uniformity among the different single-crystal orientations of ZnS. Adding an alumina abrasive to the fluid

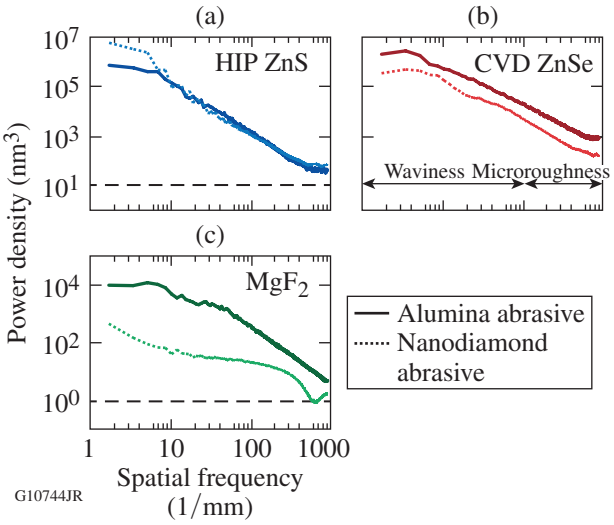

Figure 146.57
Power spectral density (PSD) for (a) CVD HIP ZnS, (b) CVD ZnSe, and (c) MgF_2 samples. The solid curves designate an acidic MR fluid with an alumina abrasive; the dotted curves designate an acidic MR fluid with nanodiamond abrasive.

caused saturation in the material removal rate with the first addition of a 1-vol % abrasive. With a nanodiamond abrasive, a constant increase in the material removal rate of ~18% was seen with any additional portion of abrasive. Surface waviness and PSD results show a significant reduction in the emergence of pebbles on the surface of several CVD ZnS substrates (samples A–D) finished with an acidic MR fluid containing nanodiamonds. The surface microroughness achieved was as low as ~30-nm p–v and ~6-nm rms. Furthermore, the variation in surface artifacts and roughness among the different CVD ZnS substrates, which is known to result from differences in detailed manufactory conditions of different suppliers,[30] was also resolved when a nanodiamond abrasive was used in the acidic MR fluid. The pronounced pits and MR grooves on the finished surfaces are believed to contribute to the overall roughness data collected and presented in this work. Since these grooves result from parts being stationary and not rotating during the process, we assume that lower roughness data, especially p–v, could be obtained if these surfaces were polished on a commercial MRF machine. The nanodiamond-based acidic MR fluid seemed to reduce the surface artifacts and microroughness of CVD ZnSe and MgF_2, but not those of CVD HIP ZnS. This finding was unexpected since CVD HIP ZnS is most similar to CVD ZnS; therefore, we would expect it to show similar surface waviness and roughness findings. This led us to the conclusion that the ceramic's crystallite (grain) size might have an effect on the resultant finish of the samples. Among the four types of polycrystalline evaluated here, CVD ZnS and MgF_2 have a smaller grain size. For these two materials, a good surface roughness and a minimal level of surface artifacts and pebbles were observed. The CVD ZnSe has an intermediate grain size (~45 μm) among the four evaluated materials. For this material some degree of surface artifacts and a surface microroughness of ~87-nm p–v and 21-nm rms were observed. The CVD HIP ZnS has the highest grain size of all four materials (~75 μm) because of the high temperature (~1000°C) reached during the HIP process, where recrystallization of the grains occurs.[22] With this material, a high degree of surface artifacts and pebbles was found on the MR-finished surface with both acidic fluids containing alumina and nanodiamonds. The surface microroughness was fairly high as well (>160-nm p–v and >36-nm rms). Further investigation of this assumption is required.

Conclusion

The addition of a polishing abrasive to the low-pH, low-viscosity MR fluid did not seem to affect the relative mrr among the different single-crystal orientations of ZnS. The overall mrr of the single-crystal orientations increased with an increasing nanodiamond concentration in the fluid but remained more or less the same when the concentration of alumina abrasives was increased. Surface-waviness and PSD results have shown that the emergence of pebbles on the surface of several CVD ZnS substrates (samples A–D) finished with the acidic MR fluid containing nanodiamonds was significantly reduced and the surface microroughness achieved was as low as ~30-nm p–v and ~6-nm rms. Furthermore, the variation in surface artifacts and microroughness among the different CVD ZnS substrates was also resolved with this type of abrasive in the acidic MR fluid. The pronounced pits and MR grooves observed on the finished surfaces contributed to the overall roughness data we collected; we believe that lower roughness data, particularly p–v, can be obtained if these surfaces were to go through a complete finishing run on a commercial MRF machine. The acidic MR fluid with nanodiamonds seemed to reduce the surface artifacts and microroughness of CVD ZnSe and MgF_2 but not that of CVD HIP ZnS. We speculate that the ceramic's grain size might have some influence in this matter. Further investigation is clearly required.

ACKNOWLEDGMENT

We thank Dr. S. Gorodkin and QED Technologies for their help and guidance with the surface waviness analysis using MetroPro software. This material is based upon work supported by the Department of Energy National Nuclear Security Administration under Award Number DE-NA0001944, the University of Rochester, and the New York State Energy Research and Development Authority. The support of DOE does not constitute an endorsement by DOE of the views expressed in this article. This work is synergistic with the NSF I/UCRC Center for Freedom Optics (IIP-1338877 and IIP-1338898).

Appendix A: White-Light Interferometer Roughness Data Collected with a 5× Objective

The data in Tables 146.XII and 146.XIII were used to perform the waviness analysis described in **Results** (p. 101).

Table 146.XII: Surface roughness (areal and lineout) collected with a 5× objective at the spots' ddp of four CVD ZnS substrates.

CVD ZnS Sample ID	Acidic MR Fluid with Alumina Abrasive				Acidic MR Fluid with Nanodiamond Abrasive			
	Areal		Lineouts		Areal		Lineouts	
	p–v (nm)	rms (nm)	p–v (nm)	rms (nm)	p–v (nm)	rms (nm)	p–v (nm)	rms (nm)
Sample A	287.56±180.42	13.42±2.00	72.93±12.18	12.56±1.16	525.96±177.97	12.53±0.91	55.78±12.35	10.64±2.53
Sample B	737.48±486.54	15.12±2.32	76.91±13.84	13.60±1.46	360.24±10.53	8.21±0.45	36.27±7.01	7.08±0.94
Sample C	1292.91±1241.49	29.37±0.94	146.63±19.77	26.98±2.10	379.23±27.48	10.46±2.13	39.90±5.40	7.99±1.08
Sample D	918.48±599.05	36.52±0.76	184.47±27.50	32.05±5.13	529.31±155.43	11.85±3.54	50.42±9.49	9.19±1.74

Table 146.XIII: Surface roughness (areal and lineout) collected with a 5× objective at the spots' ddp of CVD HIP ZnS, CVD ZnSe, and MgF_2.

Sample	Acidic MR Fluid with Alumina Abrasive				Acidic MR Fluid with Nanodiamond Abrasive			
	Areal		Lineouts		Areal		Lineouts	
	p–v (nm)	rms (nm)	p–v (nm)	rms (nm)	p–v (nm)	rms (nm)	p–v (nm)	rms (nm)
HIP ZnS	1254.13±641.29	72.67±14.50	290.56±60.10	65.26±18.10	868.02±47.76	71.70±2.95	262.40±53.54	62.90±10.40
ZnSe	1528.77±784.67	74.25±1.96	308.96±43.77	68.19±10.90	1714.70±0.76	46.70±5.98	178.90±31.38	36.00±7.02
MgF_2	237.10±1.55	8.33±1.55	46.06±8.35	7.81±1.31	37.89±4.85	2.16±0.15	7.19±1.59	1.22±0.29

REFERENCES

1. S. D. Jacobs, D. Golini, Y. Hsu, B. E. Puchebner, D. Strafford, Wm. I. Kordonski, I. V. Prokhorov, E. Fess, D. Pietrowski, and V. W. Kordonski, Proc. SPIE **2576**, 372 (1995).
2. S. D. Jacobs, S. R. Arrasmith, I. A. Kozhinova, L. L. Gregg, A. B. Shorey, H. J. Romanofsky, D. Golini, Kordonski. W. I., P. Dumas, and S. Hogan, in *Finishing of Advanced Ceramics and Glasses*, edited by R. Sabia, V. A. Greenhut, and C. G. Pantano, Ceramic Transactions, Vol. 102 (The American Ceramic Society, Westerville, OH, 1999), pp. 185–199.
3. J. E. DeGroote, H. J. Romanofsky, I. A. Kozhinova, J. M. Schoen, and S. D. Jacobs, Proc. SPIE **5180**, 123 (2003).
4. S. N. Shafrir, J. C. Lambropoulos, and S. D. Jacobs, J. Manuf. Sci. Eng. **129**, 961 (2007).
5. D. Golini, in *Precision Science and Technology for Perfect Surfaces*, edited by Y. Furukawa, Y. Mori, and T. Kataoka, JSPE Publication Series No. 3 (The Japan Society for Precision Engineering, Tokyo, Japan, 1999), pp. 132–137.
6. M. Beier *et al*., Proc. SPIE **8884**, 88840S (2013).
7. *LLE Review Quarterly Report* **80**, 213, Laboratory for Laser Energetics, University of Rochester, Rochester, NY, LLE Document No. DOE/SF/19460-321, NTIS Order No. DE00761211 (1999).
8. S. D. Jacobs, F. Yang, E. M. Fess, J. B. Feingold, B. E. Gillman, W. I. Kordonski, H. Edwards, and D. Golini, Proc. SPIE **3134**, 258 (1997).
9. I. A. Kozhinova, H. J. Romanofsky, A. Maltsev, S. D. Jacobs, W. I. Kordonski, and S. R. Gorodkin, Appl. Opt. **44**, 4671 (2005).
10. B. Hallock *et al*., in *Frontiers in Optics 2008/Laser Science XXIV/Plasmonics and Metamaterials/Optical Fabrication and Testing*, OSA Technical Digest (CD) (Optical Society of America, Washington, DC, 2008), Paper OThB2.
11. "Calcium Fluoride Properties (CaF_2)," ISP Optics, Irvington, NY, 10533, http://www.janis.com/Libraries/Window_Transmissions/CalciumFluoride_CaF2_TransmissionCurveDataSheet.sflb.ashx.
12. J. A. Menapace, P. R. Ehrmann, and R. C. Bickel, Proc. SPIE **7504**, 750414 (2009).
13. L. N. Pattanaik and H. Agarwal, Int. J. Adv. Mech. Eng. **4**, 611 (2014).
14. L. L. Gregg, A. E. Marino, J. C. Hayes, and S. D. Jacobs, Proc. SPIE **5180**, 47 (2004).
15. J. D. Nelson *et al*., Proc. SPIE **8708**, 870815 (2013).
16. M. Brophy, J. D. Nelson, and T. Hordin, in *Classical Optics 2014*, OSA Technical Digest (online) (Optical Society of America, Kohala Coast, Hawaii, 2014), Paper OW3B.3.
17. I. Kozhinova, S. R. Arrasmith, J. C. Lambropoulos, S. D. Jacobs, and H. J. Romanofsky, Proc. SPIE **4451**, 277 (2001).
18. C. Supranowitz *et al*., Proc. SPIE **6545**, 65450S (2007).
19. S. Salzman, H. J. Romanofsky, Y. I. Clara, L. J. Giannechini, G. West, J. C. Lambropoulos, and S. D. Jacobs, Proc. SPIE **8884**, 888407 (2013).
20. J. McCloy *et al*., Proc. SPIE **8016**, 80160I (2011).
21. W. D. Callister, *Materials Science and Engineering*, 2nd ed. (Wiley, New York, 1991), pp. 131–141.

22. J. S. McCloy and R. W. Tustison, *Chemical Vapor Deposited Zinc Sulfide*, Vol. PM237 (SPIE, Bellingham, WA, 2013).

23. E. M. Gavrishchuk *et al*., Inorg. Mater. **43**, 579 (2007).

24. R. Shen, H. Yang, S. N. Shafrir, C. Miao, M. Wang, J. Mici, J. C. Lambropoulos, and S. D. Jacobs, U.S. Patent No. 8,808,568 B2 (19 August 2014).

25. S. N. Shafrir, H. J. Romanofsky, M. Skarlinski, M. Wang, C. Miao, S. Salzman, T. Chartier, J. Mici, J. C. Lambropoulos, R. Shen, H. Yang, and S. D. Jacobs, Appl. Opt. **48**, 6797 (2009).

26. R. Shen, S. N. Shafrir, C. Miao, M. Wang, J. C. Lambropoulos, S. D. Jacobs, and H. Yang, J. Colloid Interface Sci. **342**, 49 (2010).

27. L. J. Giannechini, "Design and Quantification of Highly Corrosion-Resistant Magnetorheological Finishing Powder," M.S. thesis, University of Rochester, 2015.

28. S. Salzman, L. J. Giannechini, H. J. Romanofsky, N. Golini, B. Taylor, S. D. Jacobs, and J. C. Lambropoulos, Proc. SPIE **9633**, 963307 (2015).

29. SurfaceNet GmbH, Landersumer Weg 40, D-48431 Rheine, Germany.

30. S. Salzman, H. J. Romanofsky, S. D. Jacobs, and J. C. Lambropoulos, Prec. Eng. **43**, 257 (2016).

31. J. A. Salem, National Aeronautics and Space Administration, Glenn Research Center, Cleveland, OH, Report NASA/TM—2006-214100 (2006).

32. T.-C. Wen and D. K. Shetty, Proc. SPIE **7302**, 73020Z (2009).

33. Colloidal Dynamics, Ponte Vedra Beach, FL 32082.

34. Zygo Mark IVxp™, Zygo Corporation, Middlefield, CT 06455-1291, http://www.zygo.com (25 May 2016).

35. J. S. Goela and R. L. Taylor, J. Mater. Sci. **23**, 4331 (1988).

36. K. L. Lewis *et al*., in *Proceedings of the Ninth International Conference on Chemical Vapor Deposition 1984*, edited by Mc. D. Robinson *et al*. (Electrochemical Society, Pennington, NJ, 1984), pp. 530–545.

37. NewView™ 100, White Light Optical Profiler (areal over 0.26 mm × 0.35 mm with a 20× Mirau objective, no filter) by Zygo Corporation, Middlefield, CT 06455-1270, http://www.zygo.com (25 May 2016).

38. G. West, "Measuring Surface Texture in MRF Spots on Polycrystalline Material," LLE Internal Memorandum, Laboratory for Laser Energetics, University of Rochester, Rochester, NY (3 August 2011).

Publications and Conference Presentations

Publications

S.-W. Bahk, C. Dorrer, R. G. Roides, and J. Bromage, "Chromatic-Aberration Diagnostic Based on a Spectrally Resolved Lateral-Shearing Interferometer," Appl. Opt. **55**, 2413 (2016).

E. L. Dewald, F. Hartemann, P. Michel, J. Milovich, M. Hohenberger, A. Pak, O. L. Landen, L. Divol, H. F. Robey, O. A. Hurricane, T. Döppner, F. Albert, B. Bachmann, N. B. Meezan, A. J. MacKinnon, D. Callahan, and M. J. Edwards, "Generation and Beaming of Early Hot Electrons onto the Capsule in Laser-Driven Ignition Hohlraums," Phys. Rev. Lett. **116**, 075003 (2016).

T. Döppner, D. A. Callahan, O. A. Hurricane, D. E. Hinkel, T. Ma, H.-S. Park, L. F. Berzak Hopkins, D. T. Casey, P. Celliers, E. L. Dewald, T. R. Dittrich, S. W. Haan, A. L. Kritcher, A. MacPhee, S. Le Pape, A. Pak, P. K. Patel, P. T. Springer, J. D. Salmonson, R. Tommasini, L. R. Benedetti, E. Bond, D. K. Bradley, J. Caggiano, J. Church, S. Dixit, D. Edgell, M. J. Edwards, D. N. Fittinghoff, J. Frenje, M. Gatu Johnson, G. Grim, R. Hatarik, M. Havre, H. Herrmann, N. Izumi, S. F. Khan, J. L. Kline, J. Knauer, G. A. Kyrala, O. L. Landen, F. E. Merrill, J. Moody, A. S. Moore, A. Nikroo, J. E. Ralph, B. A. Remington, H. F. Robey, D. Sayre, M. Schneider, H. Streckert, R. Town, D. Turnbull, P. L. Volegov, A. Wan, K. Widmann, C. H. Wilde, and C. Yeamans, "Demonstration of High Performance in Layered Deuterium-Tritium Capsule Implosions in Uranium Hohlraums at the National Ignition Facility," Phys. Rev. Lett. **115**, 055001 (2015).

C. Dorrer, L. J. Waxer, A. Kalb, E. M. Hill, and J. Bromage, "Single-Shot, High-Resolution, Fiber-Based Phase-Diversity Photodetection of Optical Pulses," Proc. SPIE **9732**, 97320P (2016).

A. J. Harvey-Thompson, A. B. Sefkow, T. N. Nagayama, M. S. Wei, E. M. Campbell, G. Fiksel, P.-Y. Chang, J. R. Davies, D. H. Barnak, V. Y. Glebov, P. Fitzsimmons, J. Fooks, and B. E. Blue, "Diagnosing Laser-Preheated Magnetized Plasmas Relevant to Magnetized Liner Inertial Fusion," Phys. Plasmas **22**, 122708 (2015).

V. V. Ivanov, A. A. Anderson, and I. A. Begishev, "Four-Color Laser Diagnostics for Z-Pinch and Laser-Produced Plasma," Appl. Opt. **55**, 498 (2016).

L. C. Jarrott, M. S. Wei, C. McGuffey, A. A. Solodov, W. Theobald, B. Qiao, C. Stoeckl, R. Betti, H. Chen, J. Delettrez, T. Döppner, E. M. Giraldez, V. Y. Glebov, H. Habara, T. Iwawaki, M. H. Key, R. W. Luo, F. J. Marshall, H. S. McLean, C. Mileham, P. K. Patel, J. J. Santos, H. Sawada, R. B. Stephens, T. Yabuuchi, and F. N. Beg, "Visualizing Fast Electron Energy Transport into Laser-Compressed High-Density Fast-Ignition Targets," Nat. Phys. **12**, 499 (2016).

H. M. Johns, R. C. Mancini, T. Nagayama, D. C. Mayes, R. Tommasini, V. A. Smalyuk, S. P. Regan, and J. A. Delettrez, "Shell Stability and Conditions Analyzed Using a New Method of Extracting Shell Areal Density Maps from Spectrally Resolved Images of Direct-Drive Inertial Confinement Fusion Implosions," Phys. Plasmas **23**, 012709 (2016).

J. D. Kilkenny, P. M. Bell, D. K. Bradley, D. L. Bleuel, J. A. Caggiano, E. L. Dewald, W. W. Hsing, D. H. Kalantar, R. L. Kauffman, D. J. Larson, J. D. Moody, D. H. Schneider, M. B. Schneider, D. A. Shaughnessy, R. T. Shelton, W. Stoeffl, K. Widmann, C. B. Yeamans, S. H. Batha, G. P. Grim, H. W. Herrmann, F. E. Merrill, R. J. Leeper, J. A. Oertel, T. C. Sangster, D. H. Edgell, M. Hohenberger, V. Yu. Glebov, S. P. Regan, J. A. Frenje, M. Gatu-Johnson, R. D. Petrasso, H. G. Rinderknecht, A. B. Zylstra, G. W. Cooper, and C. Ruiz, "The National Ignition Facility Diagnostic Set at the Completion of the National Ignition Campaign, September 2012," Fusion Sci. Technol. **69**, 420 (2016).

F. J. Marshall, P. B. Radha, M. J. Bonino, J. A. Delettrez, R. Epstein, V. Yu. Glebov, D. R. Harding, C. Stoeckl, J. A. Frenje, M. Gatu Johnson, F. H. Séguin, H. Sio, A. Zylstra, and E. Giraldez, "Polar-Direct-Drive Experiments with Contoured-Shell Targets on OMEGA," Phys. Plasmas **23**, 012711 (2016).

P. E. Masson-Laborde, M. C. Monteil, V. Tassin, F. Philippe, P. Gauthier, A. Casner, S. Depierreux, C. Neuville, B. Villette, S. Laffite, P. Seytor, P. Fremerye, W. Seka, D. Teychenné, A. Debayle, D. Marion, P. Loiseau, and M. Casanova, "Laser Plasma Interaction on Rugby Hohlraum on the Omega Laser Facility: Comparisons Between Cylinder, Rugby, and Elliptical Hohlraums," Phys. Plasmas **23**, 022703 (2016).

Y. Ping, A. Fernandez-Panella, H. Sio, A. Correa, R. Shepherd, O. Landen, R. A. London, P. A. Sterne, H. D. Whitley, D. Fratanduono, T. R. Boehly, and G. W. Collins, "Differential Heating: A Versatile Method for Thermal Conductivity Measurements in High-Energy-Density Matter," Phys. Plasmas **22**, 092701 (2015).

M. J. Rosenberg, A. B. Zylstra, F. H. Séguin, H. G. Rinderknecht, J. A. Frenje, M. Gatu Johnson, H. Sio, C. J. Waugh, N. Sinenian, C. K. Li, R. D. Petrasso, S. LePape, T. Ma, A. J. Mackinnon, J. R. Rygg, P. A. Amendt, C. Bellei, L. R. Benedetti, L. Berzak Hopkins, R. M. Bionta, D. T. Casey, L. Divol, M. J. Edwards, S. Glenn, S. H. Glenzer, D. G. Hicks, J. R. Kimbrough, O. L. Landen, J. D. Lindl, A. MacPhee, J. M. McNaney, N. B. Meezan, J. D. Moody, M. J. Moran, H.-S. Park, J. Pino, B. A. Remington, H. Robey, M. D. Rosen, S. C. Wilks, R. A. Zacharias, P. W. McKenty, M. Hohenberger, P. B. Radha, D. Edgell, F. J. Marshall, J. A. Delettrez, V. Yu. Glebov, R. Betti, V. N. Goncharov, J. P. Knauer, T. C. Sangster, H. W. Herrmann, N. M. Hoffman, G. A. Kyrala, R. J. Leeper, R. E. Olson, J. D. Kilkenny, and A. Nikroo, "A Direct-Drive Exploding-Pusher Implosion as the First Step in Development of a Monoenergetic Charged-Particle Backlighting Platform at the National Ignition Facility," High Energy Density Phys. **18**, 38 (2016).

M. Rutkauskas, C. Farrell, C. Dorrer, K. L. Marshall, T. R. Lundquist, P. Vedagarbha, and D. T. Reid, "High-Resolution Subsurface Microscopy of CMOS Integrated Circuits Using Radially Polarized Light," Opt. Lett. **40**, 5502 (2015).

S. Salzman, H. J. Romanofsky, L. J. Giannechini, S. D. Jacobs, and J. C. Lambropoulus, "Magnetorheological Finishing of Chemical-Vapor Deposited Zinc Sulfide via Chemically and Mechanically Modified Fluids," Appl. Opt. **55**, 1481 (2016).

S. Salzman, H. J. Romanofsky, S. D. Jacobs, and J. C. Lambropoulos, "Surface–Texture Evolution of Different Chemical-Vapor-Deposited Zinc Sulfide Flats Polished with Various Magnetorheological Fluids," Prec. Eng. **43**, 257 (2016).

J. Serafini, Y. Akbas, L. Crandall, R. Bellman, C. K. Williams, and R. Sobolewski, "Time-Resolved, Nonequilibrium Carrier Dynamics in Si-on-Glass Thin Films for Photovoltaic Cells," Semicond. Sci. Technol. **31**, 045006 (2016).

W. Shang, J. Yang, W. Zhang, Z. Li, B. Deng, Y. Dong, T. Zhu, C. Huang, X. Zhan, Y. Mei, L. Guo, R. Yu, S. Li, S. Jiang, S. Liu, F. Wang, Y. Ding, B. Zhang, and R. Betti, "Experimental Demonstration of Laser to X-Ray Conversion Enhancements with Low Density Gold Targets," Appl. Phys. Lett. **108**, 064102 (2016).

S. A. Slutz, W. A. Stygar, M. R. Gomez, K. J. Peterson, A. B. Sefkow, D. B. Sinars, R. A. Vesey, E. M. Campbell, and R. Betti, "Scaling Magnetized Liner Inertial Fusion on Z and Future Pulsed-Power Accelerators," Phys. Plasmas **23**, 022702 (2016).

J. Wang, F. Coppari, R. F. Smith, J. H. Eggert, A. E. Lazicki, D. E. Frantanduono, J. R. Rygg, T. R. Boehly, G. W. Collins, and T. S. Duffy, "X-Ray Diffraction of Molybdenum Under Shock Compression to 450 GPa," Phys. Rev. B **92**, 174114 (2015).

R. Yan, R. Betti, J. Sanz, H. Aluie, B. Liu, and A. Frank, "Three-Dimensional Single-Mode Nonlinear Ablative Rayleigh–Taylor Instability," Phys. Plasmas **23**, 022701 (2016).

Forthcoming Publications

B. P. Chock, T. B. Jones, and D. R. Harding, "Effect of a Surfactant on the Electric-Field Assembly of Oil/Water Emulsions for Making Foam Targets," to be published in Fusion Science and Technology.

T. J. B. Collins, J. A. Marozas, S. Skupsky, D. Cao, P. W. McKenty, J. A. Delettrez, and G. Moses, "Design Options for Polar-Direct-Drive Targets—From Alpha Heating to Ignition," to be published in the Journal of Physics: Conference Series.

A. K. Davis, D. Cao, D. T. Michel, M. Hohenberger, R. Epstein, V. N. Goncharov, S. X. Hu, I. V. Igumenshchev, J. A. Marozas, A. V. Maximov, J. F. Myatt, P. B. Radha, S. P. Regan, T. C. Sangster, and D. H. Froula, "Isolating and Quantifying Cross-Beam Energy Transfer in Direct-Drive Implosions," to be published in Physics of Plasmas (invited).

B. Delorme, M. Olzazbal-Loumé, A. Casner, Ph. Nicolaï, D. T. Michel, G. Riazuelo, N. Borisenko, J. Breil, S. Fujioka, M. Grech, A. Orekhov, W. Seka, A. Sunahara, D. H. Froula, V. Goncharov, and V. T. Tikhonchuk, "Experimental Demonstration of Laser Imprint Reduction Using Underdense Foams," to be published in Physics of Plasmas.

W. R. Donaldson, J. Katz, R. Huff, E. M. Hill, J. H. Kelly, J. Kwiatkowski, R. Brannon, and R. Boni, "Picosecond Beam-Timing System for the OMEGA Laser," submitted to Review of Scientific Instruments.

R. Epstein, S. P. Regan, B. A. Hammel, L. J. Suter, H. A. Scott, M. A. Barrios, D. K. Bradley, D. A. Callahan, C. Cerjan, G. W. Collins, S. N. Dixit, T. Döppner, M. J. Edwards, D. R. Farley, K. B. Fournier, S. Glenn, S. H. Glenzer, I. E. Golovkin, A. Hamza, D. G. Hicks, N. Izumi, O. S. Jones, M. H. Key, J. D. Kilkenny, J. L. Kline, G. A. Kyrala, O. L. Landen, T. Ma, J. J. MacFarlane, A. J. Mackinnon, R. C. Mancini, R. L. McCrory, D. D. Meyerhofer, N. B. Meezan, A. Nikroo, H.-S. Park, P. K. Patel, J. E. Ralph, B. A. Remington, T. C. Sangster, V. A. Smalyuk, P. T. Springer, R. P. J. Town, and J. L. Tucker, "Applications and Results of X-Ray Spectroscopy in Implosion Experiments at the National Ignition Facility," to be published in Proceedings of Atomic Processes in Plasmas (invited).

R. K. Follett, J. A. Delettrez, D. H. Edgell, V. N. Goncharov, R. J. Henchen, J. Katz, D. T. Michel, J. F. Myatt, J. G. Shaw, A. A. Solodov, C. Stoeckl, B. Yaakobi, and D. H. Froula, "Two-Plasmon–Decay Mitigation in Direct-Drive Inertial Confinement Fusion Experiments Using Multilayer Targets," to be published in Physical Review Letters.

D. R. Harding, D. C. Whitaker, and C. Fella, "Growth of a Solid DT Crystal from the Liquid Inside Inertial Confinement Fusion Targets," to be published in Fusion Science and Technology.

S. X. Hu, L. A. Collins, V. N. Goncharov, J. D. Kress, T. R. Boehly, R. Epstein, R. L. McCrory, and S. Skupsky, "First-Principles Studies on the Equation-of-State, Thermal-Conductivity, and Opacity of Deuterium–Tritium and Polystyrene (CH) for Inertial Confinement Fusion Applications," to be published in the Journal of Physics: Conference Series.

S. X. Hu, L. A. Collins, V. N. Goncharov, J. D. Kress, R. L. McCrory, and S. Skupsky, "First-Principles Investigations on Ionization and Thermal Conductivity of Polystyrene (CH) for Inertial Confinement Fusion Applications," to be published in Physics of Plasmas.

I. V. Igumenshchev, V. N. Goncharov, F. J. Marshall, J. P. Knauer, E. M. Campbell, D. H. Froula, R. L. McCrory, S. P. Regan, T. C. Sangster, and S. Skupsky, "Three-Dimensional Modeling of Direct-Drive Cryogenic Implosions on OMEGA," to be published in Physics of Plasmas.

J. D. Kilkenny, J. A. Caggiano, R. Hatarik, J. P. Knauer, D. B. Sayre, B. K. Spears, S. V. Weber, C. B. Yeamans, C. J. Cerjan, L. Divol, M. J. Eckart, V. Yu. Glebov, H. W. Herrmann, S. Le. Pape, D. H. Munro, G. P. Grim, O. S. Jones, L. Berzak-Hopkins, M. Gatu-Johnson, A. J. Mackinnon, N. B. Meezan, D. T. Casey, J. A. Frenje, J. M. Mcnaney, R. Petrasso, H. Rinderknecht, W. Stoeffl, and A. B. Zylstra, "Understanding the Stagnation and Burn of Implosions on NIF," to be published in the Journal of Physics: Conference Series.

J. A. Marozas, T. J. B. Collins, J. D. Zuegel, P. W. McKenty, D. Cao, S. Fochs, and P. B. Radha, "Continuous Distributed Phase Plate Design Advances for High-Energy Laser Systems," to be published in the Journal of Physics: Conference Series.

J. F. Myatt, J. G. Shaw, V. N. Goncharov, J. Zhang, A. V. Maximov, R. W. Short, R. K. Follett, W. Seka, D. H. Edgell, and D. H. Froula, "Laser–Plasma Interaction in Direct-Drive Inertial Confinement Fusion," to be published in the Journal of Physics: Conference Series.

B. W. Plansinis, W. R. Donaldson, and G. P. Agrawal, "Temporal Waveguides for Optical Pulses," to be published in the Journal of the Optical Society of America B.

P. B. Radha, V. N. Goncharov, M. Hohenberger, T. C. Sangster, R. Betti, R. S. Craxton, D. H. Edgell, R. Epstein, D. H. Froula, J. A. Marozas, F. J. Marshall, R. L. McCrory, P. W. McKenty, D. D. Meyerhofer, D. T. Michel, S. X. Hu, W. Seka, A. Shvydky, S. Skupsky, J. A. Frenje, M. Gatu Johnson, R. D. Petrasso, T. Ma, S. Le Pape, and A. J. Mackinnon, "Direct-Drive-Implosion Physics: Results from OMEGA and the National Ignition Facility," to be published in the Journal of Physics: Conference Series.

P. B. Radha, M. Hohenberger, D. H. Edgell, J. A. Marozas, F. J. Marshall, D. T. Michel, M. J. Rosenberg, W. Seka, A. Shvydky, J. W. Bates, T. R. Boehly, T. J. B. Collins, E. M. Campbell, R. S. Craxton, J. A. Delettrez, S. N. Dixit, J. A. Frenje, D. H. Froula, V. N. Goncharov, S. X. Hu, M. Karasik, J. P. Knauer, S. Le Pape, R. L. McCrory, P. W. McKenty, D. D. Meyerhofer, J. F. Myatt, S. P. Obenschain, R. D. Petrasso, S. P. Regan, T. C. Sangster, H. Sio, S. Skupsky, and A. B. Zylstra, "Direct Drive: Simulations and Results from the National Ignition Facility," to be published in Physics of Plasmas (invited).

P. B. Radha, M. Hohenberger, F. J. Marshall, D. T. Michel, J. W. Bates, T. R. Boehly, T. J. B. Collins, R. S. Craxton, J. A. Delettrez, S. N. Dixit, D. H. Edgell, J. A. Frenje, D. H. Froula, V. N. Goncharov, S. X. Hu, M. Karasik, J. P. Knauer, S. Le Pape, J. A. Marozas, R. L. McCrory, P. W. McKenty, D. D. Meyerhofer, J. F. Myatt, S. P. Obenschein, R. D. Petrasso, S. P. Regan, M. J. Rosenberg, T. C. Sangster, W. Seka, A. Shvydky, H. Sio, S. Skupsky, and A. B. Zylstra, "Polar-Direct-Drive Experiments at the National Ignition Facility," to be published in the Journal of Physics: Conference Series.

M. Sharpe, W. T. Shmayda, and W. U. Schröder, "Tritium Migration to the Surfaces of Stainless-Steel 316, Aluminum 6061, and Oxygen-Free, High-Conductivity Copper," to be published in Fusion Science and Technology.

W. T. Shmayda, M. D. Wittman, R. F. Earley, J. L. Reid, and N. P. Redden, "The Laboratory for Laser Energetics' Hydrogen Isotope Separation System," to be published in Fusion Engineering and Design (invited).

C. Stoeckl, R. Boni, F. Ehrne, C. J. Forrest, V. Yu. Glebov, J. Katz, D. J. Lonobile, J. Magoon, S. P. Regan, M. J. Shoup III, A. Sorce, T. C. Sangster, and D. Weiner, "A Neutron Temporal Diagnostic for High-Yield DT Cryogenic Implosions on OMEGA," to be published in Review of Scientific Instruments.

N. D. Viza, M. H. Romanofsky, M. J. Moynihan, and D. R. Harding, "The Effect of a Surfactant on the Operation of T-Junctions for Mass-Producing Foam Targets," to be published in Fusion Science and Technology.

Conference Presentations

M. J. Rosenberg, A. A. Solodov, W. Seka, R. Epstein, J. F. Myatt, S. P. Regan, M. Hohenberger, T. J. B. Collins, P. Michel, D. P. Turnbull, J. D. Moody, J. E. Ralph, M. A. Barrios, and J. W. Bates, "Planar Laser–Plasma Interaction Experiments at Direct-Drive Ignition-Relevant Scale Lengths at the National Ignition Facility," NIF User Group Meeting, Livermore, CA, 1–3 February 2016.

J. D. Zuegel, A. Agliata, S.-W. Bahk, I. A. Begishev, W. A. Bittle, T. Buczek, J. Bunkenburg, D. Canning, A. Consentino, D. Coppenbarger, R. Cuffney, C. Dorrer, J. Fini, D. H. Froula, G. Gates, M. J. Guardalben, D. Haberberger, S. Hadrich, C. Hall, H. Huang, R. K. Jungquist, C. Kellogg, T. J. Kessler, G. Kick, E. Kowaluk, B. E. Kruschwitz, T. Lewis, J. Magoon, J. Marciante, D. D. Meyerhofer, C. Mileham, M. Millecchia, S. F. B. Morse, P. M. Nilson, A. Okishev, J. B. Oliver, R. G. Peck, C. Rees, B. S. Rice, E. Riedle, A. L. Rigatti, C. Robillard, R. G. Roides, M. H. Romanofsky, J. Rothhardt, M. J. Shoup III, C. Smith, C. Stoeckl, R. Taylor, L. J. Waxer, and D. Weiner, "Technology Development and Prospects for 100-PW-Class Optical Parametric Chirped-Pulse Amplification Pumped by OMEGA EP," the 2nd International Symposium on High Power Laser Science and Engineering, Suzhou, China, 15–18 March 2016.

The following presentations were made at Industrial Associates, Rochester, NY, 21–22 March 2016:

L. E. McIntire, M. Divoky, W. H. Knox, S.-W. Bahk, and J. D. Zuegel, "High-Contrast, Closed-Loop Control of Continuous-Wave Laser Beam Profiles."

B. W. Plansinis, W. R. Donaldson, and G. P. Agrawal, "Controlling the Optical Pulse Spectrum with an Electro-Optic Phase Modulator."

B. W. Plansinis, W. R. Donaldson, and G. P. Agrawal, "Temporal Waveguiding Caused by Time Reflection and Refraction."

R. Betti, A. R. Christopherson, A. Bose, K. M. Woo, J. Howard, K. S. Anderson, E. M. Campbell, J. A. Delettrez, V. N. Goncharov, F. J. Marshall, R. L. McCrory, S. P. Regan, T. C. Sangster, C. Stoeckl, W. Theobald, M. J. Edwards, R. Nora, B. K. Spears, and J. Sanz, "The Most Unsolved Problem in Plasma Physics: Demonstrating a Burning Plasma in the Laboratory," Solved and Unsolved Problems in Plasma Physics, Princeton, NJ, 28–30 March 2016 (invited).

1850
MELIORA
UNIVERSITY of
ROCHESTER